

DESIGN OF AN OUTER-ROTOR BRUSHLESS DC MOTOR FOR CONTROL
MOMENT GYROSCOPE APPLICATIONS

A THESIS SUBMITTED TO
THE GRADUATE SCHOOL OF NATURAL AND APPLIED SCIENCES
OF
MIDDLE EAST TECHNICAL UNIVERSITY

BY

NECATI ÇAĞAN

IN PARTIAL FULFILLMENT OF THE REQUIREMENTS
FOR
THE DEGREE OF MASTER OF SCIENCE
IN
ELECTRICAL AND ELECTRONICS ENGINEERING

FEBRUARY 2015

Approval of the thesis:

**DESIGN OF AN OUTER-ROTOR BRUSHLESS DC MOTOR FOR CONTROL
MOMENT GYROSCOPE APPLICATIONS**

submitted by **NECATI ÇAĞAN** in partial fulfillment of the requirements for the degree of **Master of Science in Electrical and Electronics Engineering Department, Middle East Technical University** by,

Prof. Dr. M. Gülbin Dural Ünver
Dean, Graduate School of **Natural and Applied Sciences**

Prof. Dr. Gönül Turhan Sayan
Head of Department, **Electrical and Electronics Engineering**

Prof. Dr. H. Bülent Ertan
Supervisor, **Electrical and Electronics Eng. Dept., METU**

Examining Committee Members:

Prof. Dr. Muammer Ermiş
Electrical and Electronics Eng. Dept., METU

Prof. Dr. H. Bülent Ertan
Electrical and Electronics Eng. Dept., METU

Prof. Dr. M. Kemal Leblebicioğlu
Electrical and Electronics Eng. Dept., METU

Assoc. Prof. Dr. U. Murat Leloğlu
Geodetic and Geographic Information Tech. Dept., METU

Dr. Burcu Dönmez
Guidance and Control Design Dept., ROKETSAN A.Ş.

Date:

I hereby declare that all information in this document has been obtained and presented in accordance with academic rules and ethical conduct. I also declare that, as required by these rules and conduct, I have fully cited and referenced all material and results that are not original to this work.

Name, Last Name: NECATI AĐAN

Signature :

ABSTRACT

DESIGN OF AN OUTER-ROTOR BRUSHLESS DC MOTOR FOR CONTROL MOMENT GYROSCOPE APPLICATIONS

Çağın, Necati

M.S., Department of Electrical and Electronics Engineering

Supervisor : Prof. Dr. H. Bülent Ertan

February 2015, 109 pages

Attitude control plays an important role in low-earth orbit (LEO) satellites. Agility of such systems are quite crucial and degree of agility can be determined by the help of the maneuver capability of actuators. Typical actuating systems in a low-earth orbit satellite are Control Moment Gyroscopes (CMG), and the electric motor type used in such systems is the brushless DC motor. In this study, an outer-rotor design of permanent magnet brushless DC motor to be used in a satellite application is investigated and, the main characteristics and performance parameters such as torque per unit weight, torque per unit volume, inertia contribution and power efficiency are discussed. This design is compared with various designs in a finite-element analysis environment. In conclusion, the overall performance of the motor is handled and distinct design advantages are stated.

Keywords: Control Moment Gyroscope, outer-rotor permanent magnet brushless DC motor design, performance comparison

ÖZ

KONTROL MOMENT JİROSKOP UYGULAMALARI İÇİN ROTORU DIŞARIDA FIRÇASIZ DA MOTORU TASARIMI

Çağan, Necati

Yüksek Lisans, Elektrik ve Elektronik Mühendisliği Bölümü

Tez Yöneticisi : Prof. Dr. H. Bülent Ertan

Şubat 2015 , 109 sayfa

Konum kontrolü, Alçak Dünya Yörüngesi uydularında önemli rol oynamaktadır. Bu tip sistemlerin atıklığı kritiktir ve atıklık derecesi eyleyicilerin manevra yeteneği ile belirlenir. Alçak Dünya Yörüngesi uydularındaki tipik eyleyici sistemler Kontrol Moment Jiroskoplarıdır ve bu tip sistemlerde kullanılan elektrik motoru tipi Fırçasız Doğru Akım (DA) Motorudur. Bu çalışmada uydu uygulamasında kullanılmak üzere rotoru dışarıda yer alan bir doğal mıknatıslı fırçasız DA motoru tasarımı incelenmekte ve ana karakteristikler ile birim ağırlık başına tork, birim hacim başına tork, eylemsizlik momenti katkısı ve güç verimi gibi performans parametreleri tartışılmaktadır. Bu tasarım çeşitli tasarımlarla sonlu elemanlar analizi ortamında kıyaslanmaktadır. Sonuç olarak, motorun toplu performansı ele alınmakta ve farklı tasarım avantajları ifade edilmektedir.

Anahtar Kelimeler: Kontrol Moment Jiroskop, rotoru dışarıda doğal mıknatıslı fırçasız DA motoru tasarımı, performans karşılaştırması

To my family, my friends and all anxious souls...

ACKNOWLEDGMENTS

I would like to express my sincere thanks to my thesis advisor Prof. H. Bülent ERTAN for his guidance, almost-infinite patience and endless support throughout the study.

I would also like to thank the examining committee members Prof. Muammer ERMİŞ, Prof. M. Kemal LEBLEBİCİOĞLU and Assoc. Prof. U. Murat LELOĞLU for evaluating this study.

I would like to express my deepest thanks to Burcu DÖNMEZ, as well as my colleagues and other chiefs in ROKETSAN.

I would like to give credits to Bağış Altınöz and Reza Zeinali, for their help and wizardry on MATLAB and MAXWELL, respectively.

Additionally, thanks to everyone those somehow take part and provide necessary encouragement during the whole study.

My final and the most important thanks go to my parents, M. Tuğrul ÇAĞAN and Öznur ÇAĞAN, undoubtedly, for their worthy and unrequited love, support and trust.

TABLE OF CONTENTS

ABSTRACT	v
ÖZ	vi
ACKNOWLEDGMENTS	viii
TABLE OF CONTENTS	ix
LIST OF TABLES	xiv
LIST OF FIGURES	xvi
LIST OF ABBREVIATIONS	xx
CHAPTERS	
1 INTRODUCTION	1
1.1 Scope of Thesis	1
1.2 Outline of Thesis	1
2 ACTUATING SYSTEMS IN LEO SATELLITES AND TYPICAL ELECTRICAL MOTORS	3
2.1 General Overview	3
2.2 Motor Selection for CMG Applications	5
2.3 General Overview of Brushless DC Motors	8
2.3.1 Control of Brushless DC Motors	10

3	PROBLEM DEFINITION AND MOTOR ARCHITECTURE SELECTION	13
3.1	Problem Definition and The Requirements	13
3.1.1	Problem Definition	13
3.1.2	Requirements	15
3.1.2.1	Functional Requirements	15
3.1.2.2	Motor Torque Characteristics	15
3.1.2.3	Cooling and Temperature Characteristics	17
3.2	Material Selection	20
3.2.1	Ferromagnetic Materials	20
3.2.2	Permanent Magnets (PM)	22
3.2.2.1	Permanent Magnet Selection Criteria	24
3.3	Magnetic Circuit	26
3.4	Back emf and Torque Equations for PM Brushless DC Motors	29
3.4.1	Back EMF and Torque	30
3.4.2	Radial Flux Motor Equations	30
3.4.2.1	Back emf and Torque Equations under Sinusoidal Excitation	30
3.4.2.2	Back emf and Torque Equations under Squarewave Excitation	31
3.4.3	Axial Flux Motor Equations	32
3.4.3.1	Back emf and Torque Equations under Sinusoidal Excitation	32

	3.4.3.2	Back emf and Torque Equations under Squarewave Excitation	33
	3.5	Literature Survey	34
4		DESIGN PROCEDURE OF OUTER-ROTOR BRUSHLESS DC MOTOR TOPOLOGIES	37
	4.1	Introduction to the Design of an Outer-Rotor Permanent Magnet Brushless DC Motor Configuration	37
	4.1.1	Preliminary Design Considerations	38
	4.2	Design Procedure of RF Motors under Sinusoidal Excitation .	38
	4.2.1	Magnetic Circuit of RF Motors	39
	4.2.2	Determination of Motor Dimensions for Sinusoidal Excitation	42
	4.2.3	Winding Design	46
	4.2.4	Equivalent Circuit Parameters	47
	4.2.4.1	Phase Resistance	47
	4.2.4.2	Phase Inductance	48
	4.2.5	Losses	50
	4.2.6	Motor Mass, Volume, Inertia and Efficiency	51
	4.3	Design Procedure of RF Motors under Squarewave Excitation	53
	4.3.1	Determination of Motor Dimensions for Square-wave Excitation	53
	4.3.2	Winding Design	55
	4.3.3	Equivalent Circuit Parameters	55
	4.3.4	Losses	56

4.3.5	Motor Mass, Volume, Inertia and Efficiency	56
4.4	Design Outputs	57
4.4.1	Comparisons between Pole Numbers	57
4.4.2	Comparisons between Excitations	58
5	ANALYTICAL RESULTS	63
5.1	Analytical Results	63
5.1.1	Analytical Results of Sinusoidal Designs	65
5.1.1.1	Sinusoidal 2-pole Design	65
5.1.1.2	Sinusoidal 6-pole Design	66
5.1.2	Sizes and Performance Evaluation of Squarewave Designs	67
5.1.2.1	Squarewave 2-pole Design	67
5.1.2.2	Squarewave 6-pole Design	68
5.2	Overall Performance Comparison	68
6	SIMULATION RESULTS	71
6.1	Simulation Results	71
6.1.1	Simulation Results of Sinusoidal Designs	72
6.1.1.1	Sinusoidal 2-pole Design	73
6.1.1.2	Sinusoidal 6-pole Design	76
6.1.2	Simulation Results of Squarewave Designs	79
6.1.2.1	Squarewave 2-pole Design	80
6.1.2.2	Squarewave 6-pole Design	82

6.2	Comparison of The Results with an Axial-Flux Equivalent . .	84
6.2.1	Simulation Results in MAXWELL	84
6.2.2	Overall Finite Element Analysis Results	85
7	CONCLUSION	91
7.1	Overall Results	91
7.2	Future Work	94
	REFERENCES	97
APPENDICES		
A	PARAMETERS AND DESCRIPTIONS	99
B	DESIGN OUTPUTS WITH VARYING RATIO VALUES	101
C	CHOSEN DESIGNS FOR EACH TOPOLOGY	107
D	6-POLE SQUAREWAVE AXIAL-FLUX DESIGN PARAMETERS .	109

LIST OF TABLES

TABLES

Table 2.1	Applications of Different Motor Types (retrieved from [1])	7
Table 3.1	Main Functional Requirements	15
Table 3.2	COTS Motor Parameters	16
Table 3.3	Parameters for Thermal Calculation	19
Table 3.4	Core Loss Data of Cogent Power No.12	23
Table 3.5	Some Parameters of The Ferromagnetic Material	24
Table 3.6	Properties of Selected PM [2]	26
Table 4.1	Expressions for Basic Dimensions	54
Table 4.2	Summary of Equivalent Circuit Parameters	55
Table 4.3	Summary of Motor Mass, Volume, Inertia and Efficiency Equations	56
Table 5.1	Overall Performance Parameters at Steady-State	70
Table 6.1	Comparison of Analytical and Simulation Results of Sinusoidal 2-Pole BLDC Motor at Steady-State	77
Table 6.2	Comparison of Analytical and Simulation Results of Sinusoidal 6-Pole at Steady-State	81
Table 6.3	Comparison of Analytical and Simulation Results of Squarewave 2-Pole at Steady-State	85
Table 6.4	Comparison of Analytical and Simulation Results of Squarewave 6-Pole at Steady-State	89
Table 6.5	Overall MAXWELL Results	90

Table A.1 Parameters and Descriptions	100
Table B.1 Design Outputs Calculated Analytically for Sinusoidal 2-pole Topology	102
Table B.2 Design Outputs Calculated Analytically for Sinusoidal 6-pole Topology	103
Table B.3 Design Outputs Calculated Analytically for Squarewave 2-pole Topology	104
Table B.4 Design Outputs Calculated Analytically for Squarewave 6-pole Topology	105
Table C.1 Chosen Designs	107
Table D.1 AF 6-pole Design	109

LIST OF FIGURES

FIGURES

Figure 2.1	Typical Orbit of a Low-Earth Orbit Satellite	4
Figure 2.2	Basic Gyroscope Structure (retrieved from [3])	4
Figure 2.3	Basic Structure of a CMG (taken from [4])	5
Figure 2.4	Working Principle of a CMG (taken from [5])	6
Figure 2.5	General Motor Structure (taken from [6])	6
Figure 2.6	Typical BLDC Motor	8
Figure 2.7	Radial Flux BLDC Motor Configuration	9
Figure 2.8	Axial-Flux BLDC Motor Configuration	10
Figure 2.9	Current Waveforms in Sinusoidal Excitation	10
Figure 2.10	Current Waveforms in Squarewave Excitation	11
Figure 2.11	Control Loop for A Brushless DC Motor (taken from [7])	11
Figure 3.1	Current Integrated CMG on Satellite System (taken from [7])	14
Figure 3.2	Prepared Motor Model in SIMULINK	16
Figure 3.3	Mechanical Speed	17
Figure 3.4	Motor Torque-Speed Characteristics	17
Figure 3.5	Analogous Thermal Model [7]	18
Figure 3.6	Thermal Model of The Motor	19
Figure 3.7	Temperature Characteristics Obtained from Model	20
Figure 3.8	Typical B-H Curve of a Ferromagnetic Material (taken from [8])	21
Figure 3.9	B-H Curve of The Core Material (Cogent Power No.12)	22

Figure 3.10 Demagnetization Curve of a PM	24
Figure 3.11 Typical BLDC Motor (retrieved from [6])	26
Figure 3.12 Magnetic Circuit of the BLDC Motor (retrieved from [6])	27
Figure 3.13 Simplified Magnetic Circuit (retrieved from [6])	27
Figure 4.1 Division of The Topologies	37
Figure 4.2 Structure of an Outer-Rotor BLDC Motor	38
Figure 4.3 Magnetic Circuit of Outer-Rotor BLDC Motor	39
Figure 4.4 Equivalent Circuit of BLDC Motor (per phase)	48
Figure 4.5 Typical Tooth-Slot Geometry	49
Figure 4.6 End Turn Geometry for Calculation of End-Turn Inductance	50
Figure 4.7 Volume Comparison of Designs Under Different Pole Numbers	57
Figure 4.8 Mass Comparison of Designs Under Different Pole Numbers	58
Figure 4.9 Inertia Comparison of Designs Under Different Pole Numbers	58
Figure 4.10 Efficiency Comparison of Designs Under Different Pole Numbers	59
Figure 4.11 Volume Comparison of Designs Under Different Excitation	59
Figure 4.12 Mass Comparison of Designs Under Different Excitation	60
Figure 4.13 Inertia Comparison of Designs Under Different Excitation	60
Figure 4.14 Efficiency Comparison of Designs Under Different Excitation	61
Figure 5.1 Tooth - Slot Dimensions	64
Figure 5.2 Electrical Loading Variation with Increasing Ratio	64
Figure 5.3 Analytical Results for Sinusoidal 2-pole Design	65
Figure 5.4 Analytical Results for Sinusoidal 6-pole Design	66
Figure 5.5 Analytical Results for Squarewave 2-pole Design	67
Figure 5.6 Analytical Results for Squarewave 6-pole Design	69
Figure 6.1 Simulation Model	72

Figure 6.2	Motor Model Prepared in MAXWELL (sinusoidal 2-pole)	73
Figure 6.3	Magnetic Fields Obtained From MAXWELL for Sinusoidal 2-pole Topology	74
Figure 6.4	Flux Density Along Air Gap and Tooth (sinusoidal 2-pole)	74
Figure 6.5	Winding Current and Induced Voltage Obtained From MAXWELL for Sinusoidal 2-pole Topology	75
Figure 6.6	Torque and Speed Obtained From MAXWELL for Sinusoidal 2- pole Topology	76
Figure 6.7	Magnetic Fields Obtained From MAXWELL for Sinusoidal 6-pole Topology	78
Figure 6.8	Flux Density Along Air Gap and Tooth (sinusoidal 6-pole)	78
Figure 6.9	Winding Current and Induced Voltage Obtained From MAXWELL for Sinusoidal 6-pole Topology	79
Figure 6.10	Torque and Speed Obtained From MAXWELL for Sinusoidal 6- pole Topology	80
Figure 6.11	Magnetic Fields Obtained in MAXWELL for Squarewave 2-pole Topology	82
Figure 6.12	Flux Density Along Air Gap and Tooth (squarewave 2-pole)	82
Figure 6.13	Winding Current and Induced Voltage Obtained From MAXWELL for Squarewave 2-pole Topology	83
Figure 6.14	Torque and Speed Obtained From MAXWELL for Squarewave 2-pole Topology	84
Figure 6.15	Magnetic Fields Obtained in MAXWELL for Squarewave 6-pole Topology	86
Figure 6.16	Flux Density Along Air Gap and Tooth (squarewave 6-pole)	86
Figure 6.17	Winding Current and Induced Voltage Obtained From MAXWELL for Squarewave 6-pole Topology	87
Figure 6.18	Torque and Speed Obtained From MAXWELL for Squarewave 6-pole Topology	88
Figure 6.19	Magnetic Fields Obtained in MAXWELL for AF Squarewave 6- pole Topology	89

Figure 6.20 Parameters Obtained From MAXWELL for AF Squarewave 6-pole Topology	90
Figure 7.1 Overall Volume Comparison of Chosen Designs	92
Figure 7.2 Overall Mass Comparison of Chosen Designs	92
Figure 7.3 Overall Inertia Comparison of Chosen Designs	93
Figure 7.4 Overall Efficiency Comparison of Chosen Design	93

LIST OF ABBREVIATIONS

AF	Axial Flux
BLDC	Brushless DC
CMG	Control Moment Gyroscope
COTS	Commercial off-the-shelf
DC	Direct Current
emf	Electromotive Force
FEA	Finite-Element Analysis
LEO	Low Earth Orbit
PM	Permanent Magnet
RF	Radial Flux
rms	Root-Mean-Square

CHAPTER 1

INTRODUCTION

1.1 Scope of Thesis

Actuating systems are widely used in aerospace applications, as well as other consumer electronic systems or other household applications. In an actuating system within an aerospace application such as satellites, brushless DC motors are coupled with the momentum wheel and play an important role in controlling these systems in order to stabilize and give required maneuver to the whole system.

This thesis study mainly focuses on the conventional brushless direct-current (DC) motors used in such applications and proposes certain outer-rotor topologies and discusses the strengths and weaknesses between each other in terms of torque characteristics per unit volume and mass, efficiency, and inertia.

1.2 Outline of Thesis

This thesis is divided into six main chapters, except from this chapter, and each of which focuses on a certain topic as a milestone.

Chapter 2 presents the fundamentals of a typical control moment gyroscope actuating system configuration and electrical motors used in these systems. Furthermore, the electrical motor to be designed is presented such that types of the electrical motors are stated.

Chapter 3 defines the main problem in current control moment gyroscope (CMG) sys-

tems and major requirements related to the wheel motors are stated. Then, fundamental concepts related to permanent magnet brushless DC motors are defined. In this manner, magnetic circuit characteristics and specific torque equations relating basic sizes of the motors that will be used throughout the study are presented in corresponding sections.

Chapter 4 states the design of the proposed outer-rotor brushless DC motor topologies, derives the main expressions used throughout the design process. Changes in the design both for pole numbers and excitation such as squarewave or sinusoidal are presented.

Chapter 5 presents the results and makes discussions on these results. Main advantages and disadvantages of each design is discussed.

Chapter 6 presents the results obtained in a finite-element analysis tool in order to verify the analytical results.

Chapter 7 concludes the thesis by summarizing the overall study and stating a brief future work.

CHAPTER 2

ACTUATING SYSTEMS IN LEO SATELLITES AND TYPICAL ELECTRICAL MOTORS

2.1 General Overview

Low-Earth Orbit (LEO) satellites are used for taking images of the Earth ground. These systems have an orbit starting from one pole of the Earth towards the other pole and have a quite high orbit speed, as shown in Figure 2.1. In order to take proper images of the ground, these systems must have a sensitive attitude control system, and agility of such systems has quite importance. The degree of agility of satellites can be determined by their maneuver capability. Satellites make the necessary maneuvers by the aid of the actuators inside. Three main actuators take place in a typical satellite, namely reaction wheels, momentum wheels and control moment gyroscopes, all of which work based on the conservation of angular momentum principle. The first two examples drive a high-inertia wheel by the electric motor inside itself. These electric motors are coupled to the wheel. By properly controlling the speed of the motor, the necessary torque action for the satellite is obtained.

Control moment gyroscopes (see the basic gyroscope drawing in Figure 2.2) can be used in order to give direction to a spacecraft. The control moment gyroscope is assembled to a system along the axis in which the torque to be induced. The wheel axis and the gimbal axis are perpendicular to each other. As a working principle, a wheel is driven by its related motor at a specific rate. In addition, another motor assembled to the gimbal also rotates the gimbal and the wheel around the gimbal axis. After this point, any movement along the rotation plane of the wheel axis leads to an induced

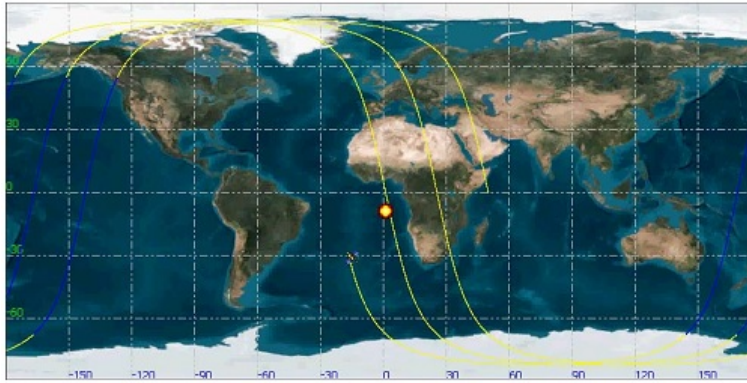


Figure 2.1: Typical Orbit of a Low-Earth Orbit Satellite

torque which is perpendicular to both gimbal axis and wheel axis. As a result, this torque is transferred to the spacecraft in order to make necessary maneuver.[3]

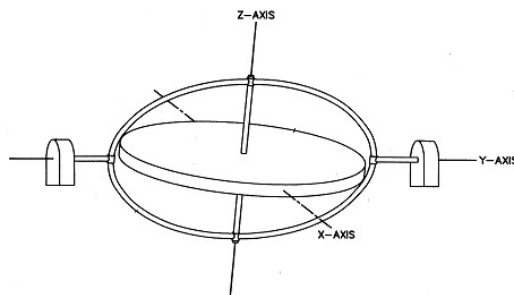


Figure 2.2: Basic Gyroscope Structure (retrieved from [3])

As explained above, CMG consists of a spinning disc with a large angular velocity ω , which rotates about x-axis as shown in Figure 2.3 [4]. Practically, when one intends to rotate the spinning disc around the z-axis with a small rate, then a large rotation must be applied around y-axis. This phenomena can be explained by the concept of momentum. First, a motor with a high speed, such as between 6000 and 10000 rpm, must be used in order to rotate spinning disc. Torque is created after changing momentum in the other axis (here, z-axis). This can be done by using another type of motor with a low speed, such as 20 rpm. Hence, the torque is produced on the perpendicular axis as shown in Figure 2.4.

Depending on the mechanical characteristics, CMGs can be characterized into three types, namely single-gimbal CMG, double-gimbal CMG and variable-speed CMG. In single-gimbal CMGs, momentum wheel is gimbaled in one axis and constrained to rotate on a circle in a plane normal to the gimbal axis while momentum is constrained inside two gimbals and angular momentum is oriented within a sphere in double-axis

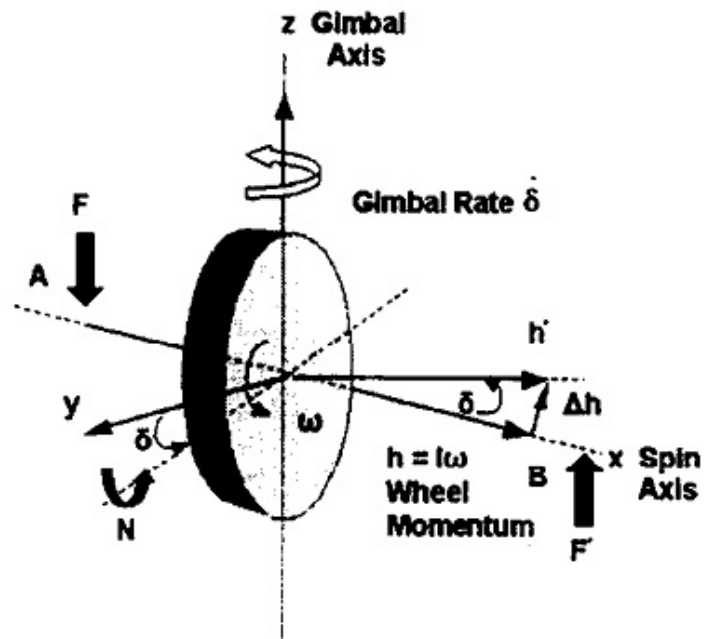


Figure 2.3: Basic Structure of a CMG (taken from [4])

CMG. Variable-speed CMGs have a variable speed momentum wheel and an extra degree of control is made available compared to the single-gimbal case. Single-gimbal CMGs provide higher torque amplification compared to the other two, but there are certain angles in which the CMG does not produce torque, which is called singularity. In order to overcome this problem, some special techniques are used, which is not in the scope of this thesis. [9]

In this thesis, main design process will be handled for the motor to be assembled to the wheel axis. Hence, the motor is required to operate at higher speeds compared to the one for gimbal motor, and the power consumption of this motor is going to be higher than that of the gimbal motor. Main functional and environmental specifications such as temperature is going to be studied in Chapter 4.

2.2 Motor Selection for CMG Applications

As stated in previous section, two main motors are included in a typical CMG system. In general, both AC and DC motors can be used in a typical aerospace application. Induction motors are preferred as an AC motor solution, and brushed or brushless DC motors are both preferred as the DC solution. Brushless solution is the best alternative

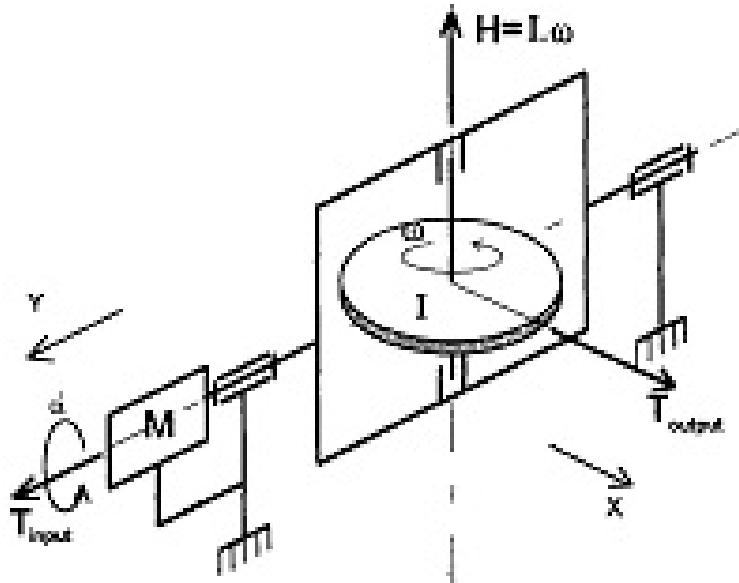


Figure 2.4: Working Principle of a CMG (taken from [5])

among all; because they have higher power/mass ratio, higher efficiency and longer life ratings. In a typical electrical motor (see Figure 2.5), there exist two distinct magnetic fields, one is for armature and the other is for field. Field flux is created either by permanent magnets or by an additional winding. In case a winding is used for field, one must consider the slip rings or brushes for commutation. In a high-speed application, the maintenance issue must be handled properly by the designer. In such a case, brushless solutions must be taken into consideration. The applications of motor types are summarized in Table 2.2.

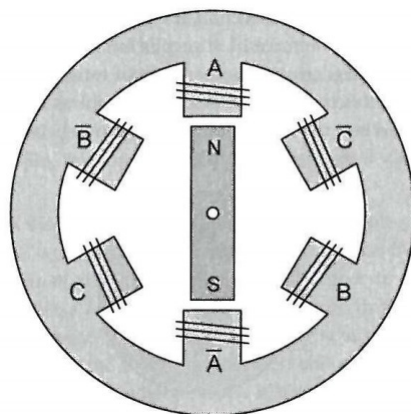


Figure 2.5: General Motor Structure (taken from [6])

As seen in Table 2.2, brushless motors can be considered as the core motor used in industry. Other main advantages of BLDC motors ([10]) are stated as follows:

Table 2.1: Applications of Different Motor Types (retrieved from [1])

AC Induction Motors	Brushed DC Motors	Brushless DC Motors	Stepper Motors
Thrust Vector Control Applications High-Torque and High-rpm Applications	Limited Life-Time Applications Low-rpm Applications High-Torque Applications	Thrust Vector Control Applications Fuel Valve Control Actuators Solar Array Deployment Control Moment Gyroscopes High-rpm Applications Light Weight Applications Low Thermal Emission Applications	Optical Drives Solar Array Deployment Gimbal Positioning Low-Torque Applications Open-Loop Micro Positioning Timer Switching

- High speed which may increase up to 100.000 rpm
- High torque at high speeds
- Higher torque ratings (about double) when compared to brushed DC motor equivalents with same size
- No winding on rotor, improvement on heat dissipation
- No brushes, no high maintenance cost
- Higher efficiency
- Vacuum compatible

On the other hand, the disadvantages of using a brushless DC motor in an aerospace application may be counted as relatively higher electronic cost and increase in complexity of the drive circuitry. [10] As a whole, brushless DC motors are preferred as an electrical motor solution at all applications in industry, as well as aerospace applications.

2.3 General Overview of Brushless DC Motors

A typical brushless DC motor (see Figure 2.6) is excited with balanced three-phase windings. These windings are excited in stator winding. The coils are wound in stator slots. Permanent magnets are placed on the rotor side. Rotor rotates inside the stator in synchronism with the stator with respect to the rotation of the phase windings on the stator side. By changing the excitation of the phase windings properly, a continuous rotational motion is achieved on the rotor side. At each commutation sequence, one of the windings is energized with positive power while the other winding is energized with negative. The remaining winding is kept neutral. Torque is produced due to the interaction of coils in stator and the magnetic field created in rotor (by permanent magnets). [11].

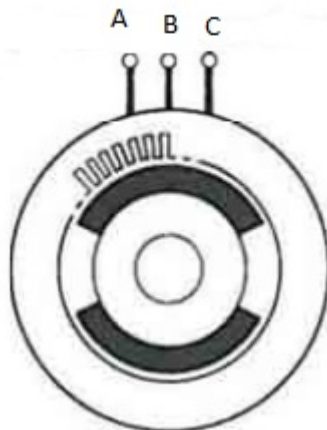


Figure 2.6: Typical BLDC Motor

Permanent magnet (PM) brushless DC (BLDC) motors can be classified in different categories. One classification criteria for brushless DC motors is the magnet structure. Main motors being discussed about the magnet structure are the surface-mounted motors, interior mounted motors and buried-magnet motors. Surface-mounted motors, as the name implies, are mounted on the rotor surface. This process is relatively easy and cost-efficient. Moreover, with the surface mounted magnets, one can obtain a larger air gap. The most important disadvantage of such configuration is the possibility of detachment of the magnet from the rotor surface in high speeds. As a second, magnets are put inside the rotor in an interior mounted motor. Such a motor can operate at higher speeds. On the other hand, direct axis and quadrature axis inductances are different, which leads to reluctance torques. The electrical characteristics of interior

motors and the buried-magnet motors are equivalent.

The other classification of PM BLDC motors is the flux direction. Two major types appear in this categorization, namely radial flux (RF) motors and axial flux (AF) motors. The most widely used motor topology is the radial flux motors. As the name implies, flux radially flows through the air gap in RF motors. The axial length of these motors are relatively long. Thus, the motor has a sausage-like shape, as shown in Figure 2.7. RF motors are kept to have a low inertia in order to have better response time and hence, are preferred in servo applications. Axial flux motors, on the other hand, have a flux pattern flowing in axial direction through the air gap. An axial flux configuration mostly includes two rotor and a stator, as shown in Figure 2.8. Stator is located between two rotor discs. Here, the main drawback of these motors appears such that the design procedure must be handled carefully due to the presence of two air gaps.

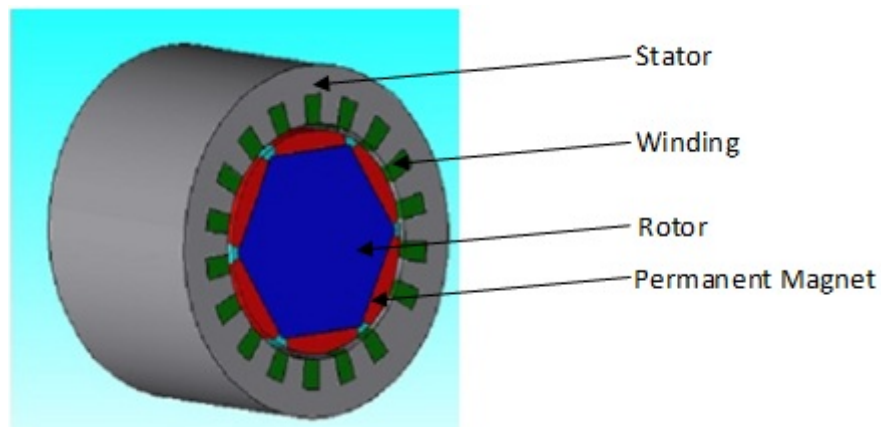


Figure 2.7: Radial Flux BLDC Motor Configuration

The last classification is on the excitation type of the brushless DC motors. Mainly, brushless DC motors are excited either trapezoidally or sinusoidally. Hence, the back electromotive forces (emf) are generated accordingly. Trapezoidal back emf generation is quite common in brushless DC motors. Such waveforms may lead to constant torque pulsations due to the fact that current waveforms can be more easily controlled. (see Figures 2.9 and 2.10 for typical current waveforms)

When the excitation is in trapezoidal form, one can obtain higher power density and use both concentrated and full-pitched windings. On the other hand, in the excitation in sine form, fractional-slot windings can be used for a smoother operation and a better

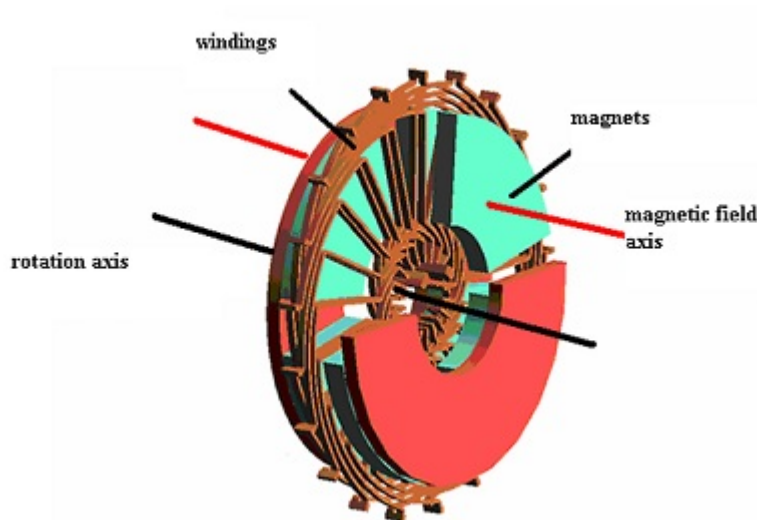


Figure 2.8: Axial-Flux BLDC Motor Configuration

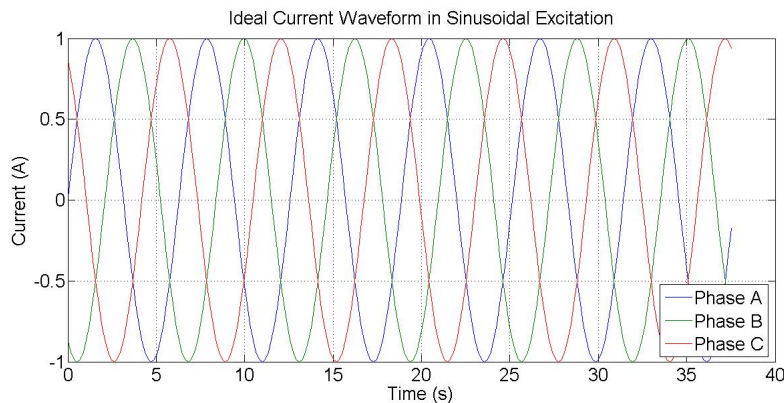


Figure 2.9: Current Waveforms in Sinusoidal Excitation

control can be obtained. ([12])

2.3.1 Control of Brushless DC Motors

Generally, brushless DC motors can be controlled with two control loops: one is for current, and hence electromagnetic torque, control and the other is for voltage, and therefore the speed. As a typical control loop, measured signal is compared with the reference signal and the required control actions are taken in order to fully control the system. First, current control is achieved by comparing the measured speed data with the one taken as reference. By applying proper control laws (e.g. PID), necessary current is obtained as a reference current to the minor control loop. By measuring the current, proper control laws are applied in order to control the voltage. Finally, applying a necessary voltage to the system leads to the speed control of the brushless

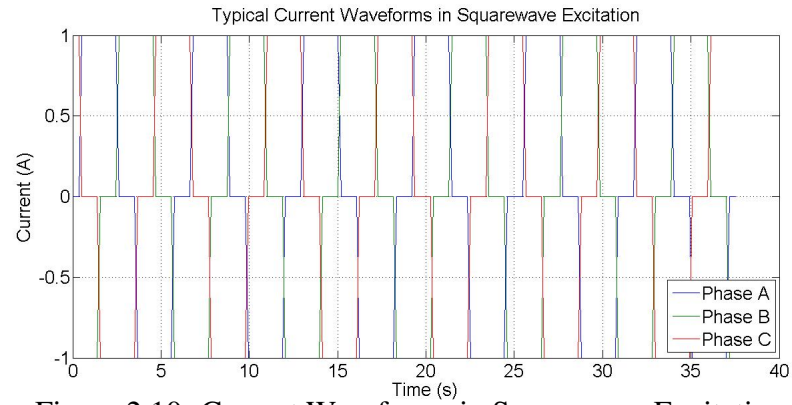


Figure 2.10: Current Waveforms in Squarewave Excitation

DC motors. Control system of the motors in block diagram is depicted in Figure 2.11.

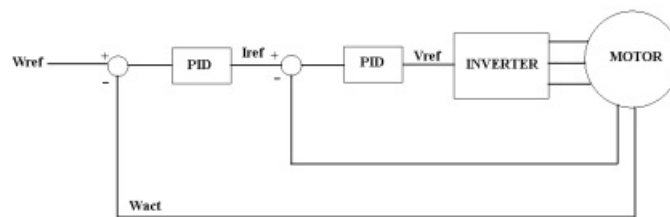


Figure 2.11: Control Loop for A Brushless DC Motor (taken from [7])

To sum up, brushless DC motors are widely used in different industrial applications, and such motors have a wide variety depending on the magnet structure, flux direction and excitation, each of which may be used for different purposes.

In the following chapter, problems related to current CMGs are going to be handled and main selection criteria in motor architecture selection is going to be investigated.

CHAPTER 3

PROBLEM DEFINITION AND MOTOR ARCHITECTURE SELECTION

This chapter first states the problem in existing CMG motors and define the main requirements and then, general expressions are derived for conventional BLDC motors. Here, the term "conventional" is used for the topology, where the stator is located outside the motor and the excitation is made, while the rotor is located inside the motor where the mechanical power is obtained.

3.1 Problem Definition and The Requirements

3.1.1 Problem Definition

In this thesis, the BLDC motor to be designed is for the wheel motor. Wheel motor operates at a relatively high constant speed, which is in the order of 10000 rpm. An acceleration time between 1 and 2 minutes will be taken into consideration and friction and windage torque components due to bearings will be investigated.

For CMG prototypes, commercial off-the-shelf (COTS) motor designs are being used. This leads to the necessity of a new design; because COTS products are manufactured as sausage-type BLDC motors. As a wheel motor, the inertia contribution of such a design is relatively low. On the contrary, more inertia contribution is made for the gimbal motor, which in turn leads to an increase in the power consumption of the gimbal motor. Due to the fact that it is a sausage-type, the load must be coupled to the motor with an external coupling. Furthermore, the distance between bearings are

relatively high; hence balancing problems may occur in such designs.

The second problem is the compatibility issues between the COTS design and the requirements. For a motor design to be used in such applications, the major disturbance component is the friction torque between shaft and bearings. Commercial motors are usually designed for dynamic load conditions, which may make these designs over-safe and over-designed, which in turn leads to an increase in mass or volume. Hence, a motor must be designed to fulfill the requirements with total correspondence.

As a whole, an alternative motor must be designed considering the mass and volume issues in an integrated system. Figure 3.1 shows a CMG prototype including an axial-flux motor as a wheel motor. Current motor system is integrated to the system by using 4 ball bearings. Reducing the number of the bearings and minimizing the frictional loads, total volume and mass of the motor, as well as increasing the efficiency is going to be main motivation of this study. For this purpose, the design conducted in [7] will be taken as a reference study and comparisons will be handled accordingly.

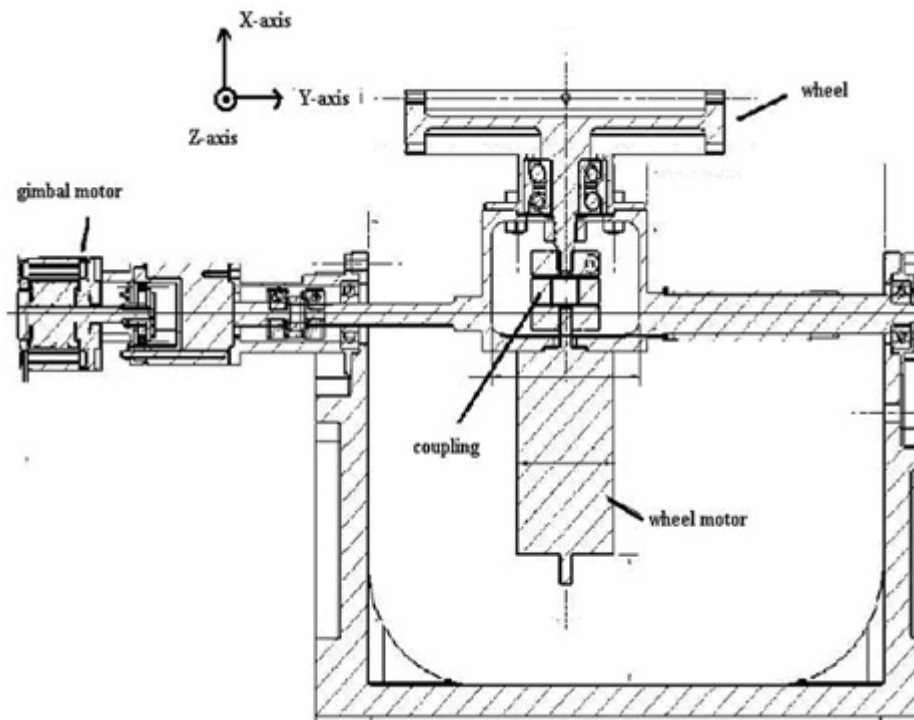


Figure 3.1: Current Integrated CMG on Satellite System (taken from [7])

3.1.2 Requirements

3.1.2.1 Functional Requirements

Functional requirements are derived from the requirements from the system-level requirements. An existing CMG has a total wheel inertia of $4.83 \times 10^{-4} \text{kg.m}^2$. The motor to be designed is desired to have an inertia as large as possible due to the fact that it is desired to have a large inertia contribution to the total wheel system. In addition, rotation of the wheel motor with a rate of 10.000 rpm is defined. Finally, accelerating the wheel system in between 35 and 120 seconds is set to be as the acceleration time. Main functional requirements of the motor to be designed is summarized in Table 3.1.

Table 3.1: Main Functional Requirements

Parameter	Value
<i>Inertia (kg.m²)</i>	4.83×10^{-4}
<i>Mechanical speed (rpm)</i>	10000
<i>Acceleration time (s)</i>	35 - 120
<i>Acceleration torque (mN-m)</i>	50
<i>Nominal torque (mN-m)</i>	32

3.1.2.2 Motor Torque Characteristics

In order to start a proper design of BLDC motor, one must consider the motor torque characteristics. The primary goal to be achieved is the determination of the acceleration time of the motor to a certain speed level. Here, the defined speed level is taken as 10000 rpm and it is desired to reach such levels in less than 120 seconds.

From previous experience [7], it is known that a BLDC motor manufactured by MAXON (model number 118892) was successfully used in an existing CMG prototype. Therefore, motor torque characteristics will be defined by taking this motor as a commercially off-the-shelf reference. The parameters of this motor is summarized in Table 3.2.

Table 3.2: COTS Motor Parameters

Parameter	Value
Inertia ($kg.m^2$)	4.83×10^{-4}
Angular speed (rpm)	10000
Acceleration time (s)	35 - 120
Mass (g)	263
Efficiency	78%
Operating Temperature ($^{\circ}C$)	(-20) - (+65)
Operating Voltage	18 - 33
Torque (mN.m)	32 nominal, 50 max
Application	Const. speed

Furthermore, the speed vs. time characteristics can be modeled with a simple model, as shown in Figure 3.2. Basically, electromechanical torque can be calculated as shown in Equation 3.1.

$$\tau_{em} = J_{wheel} \frac{dw_m}{dt} + \tau_{load} \quad (3.1)$$

where τ_{em} is the electromechanical torque, J_{wheel} is the inertia of the wheel, w_m is the angular mechanical speed, and τ_{load} is the load torque.

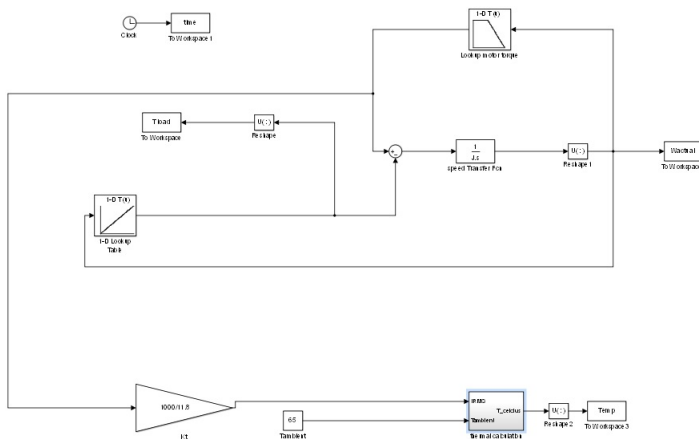


Figure 3.2: Prepared Motor Model in SIMULINK

The major aim in preparing a motor model is to see the speed characteristics of the motor with changing time. The motor model is constructed by taking Equation 3.1 as a reference and measure the actual speed of the motor with changing time. Thus, the mechanical speed of the motor is shown in Figure 3.3. According to Figure 3.3, the

motor reaches a steady-state speed after 40 seconds.

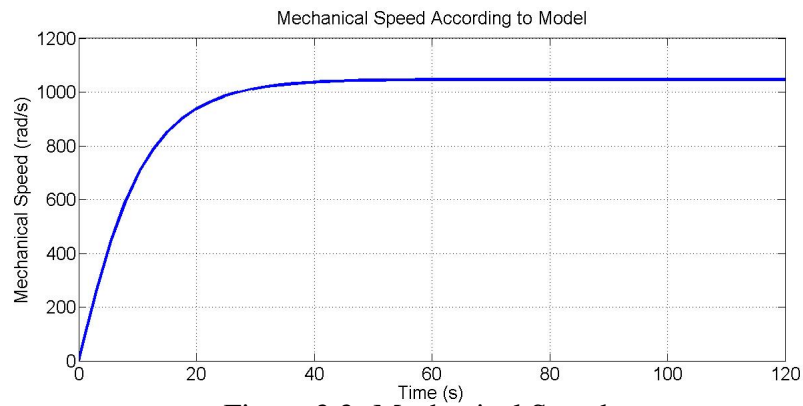


Figure 3.3: Mechanical Speed

Hence, in order to study on the torque characteristics depending on the speed, it is plausible to take the motor torque-speed characteristics as shown in Figure 3.4.([7])

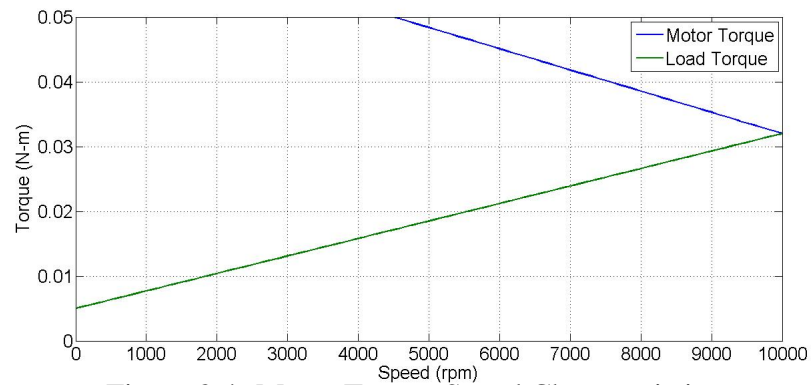


Figure 3.4: Motor Torque-Speed Characteristics

One additional note must be taken here that, in Figure 3.4, load torque is also shown. The load torque approaches to the value of 32 mN-m at rated speed, which is 10.000 rpm [7]. Hence, it is concluded that at rated speed, the electromechanical torque produced by the motor becomes equal to the load torque which is defined as 32 mN-m, and the motor operates in a steady-state behaviour and no acceleration occurs in overall system, which means a proper operation is obtained in the wheel system.

3.1.2.3 Cooling and Temperature Characteristics

Generally, temperature characteristics of a motor is investigated due to the cooling issues. The electrical motor to be designed is intended to operate in a space environment. Thus, one must consider the cooling techniques related to conduction and radiation

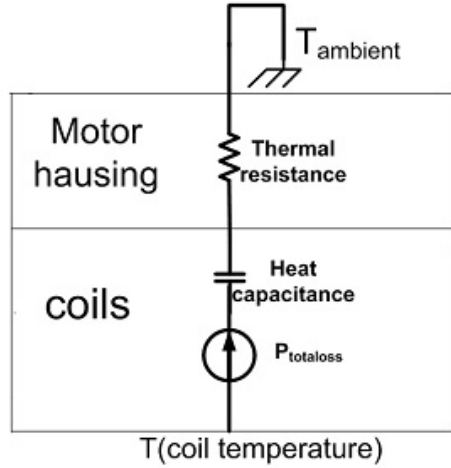


Figure 3.5: Analogous Thermal Model [7]

in case no gaseous solution is considered to take into account the convection. On the other hand, there is no radiation information, as well as there is no space environment in order to conduct proper tests. Thus, a modeling work is needed. For this purpose, a previous modeling study is taken as a reference which was conducted by using the commercial motor stated in previous section; and temperature characteristics are studied accordingly. The results of the COTS motor is given in [7] as per the manufacturer data. With the parameters given for the COTS design as shown in Figure 3.3, the temperature is measured to be about 72 °C, with a total loss value of 8.3 Watts. By considering the output power of 33 W, the efficiency is found to be 78%, as provided by the manufacturer.

As a result, temperature characteristics of an electrical motor can be calculated with the help of a simple model as explained in [13]. Basic thermal balance equation of a winding is shown in Equation 3.2, regarding the analogy given in Figure 3.5.

$$mc \frac{dT}{dt} = P_{loss} - Q \quad (3.2)$$

where m denotes the mass of the winding, c denotes the specific heat of the winding, T denotes the temperature of the winding, P_{loss} denotes the total loss in the motor, which consists of total core loss and the total copper loss, and Q denotes the heat supplied by conduction and convection to the ambient. This heat is expressed as in Equation 3.3.

$$Q = \frac{T - T_{ambient}}{R_{coil-housing} + R_{housing-ambient}} \quad (3.3)$$

Here, $T_{ambient}$ denotes the ambient temperature, $R_{coil-housing}$ is the thermal resistance between coils and housing and $R_{housing-ambient}$ is thermal resistance between housing and ambient. Copper losses and core losses are to be calculated in Chapter 4, and the necessary values are taken from there by calculating all performance parameters such as current as phase resistance. Hence, total losses are taken as 3.55 Watts. Total copper weight is calculated as 163 grams. Other parameters are shown in Table 3.3. These parameters are used in order to predict the thermal behaviour of the motor to be designed. The mathematical model, which is prepared in SIMULINK environment and used to calculate the thermal characteristics, is shown in Figure 3.6 and the output of this model, which is the coil temperature, is given in Figure 3.7. According to the model, it is seen that at the end of the defined operation time, the temperature of the coils increases up to 68 °C, without a settling trend. Hence, a temperature rise of 3 degrees at the end of the operation time is in an acceptable level if the permissible motor temperature is considered to be 125 °C [7].

Table 3.3: Parameters for Thermal Calculation

Parameter	Value
$R_{coil-housing} (^{\circ}C/W)$	2,5
$R_{housing-ambient} (^{\circ}C/W)$	5,4
$T_{ambient} (^{\circ}C)$	65
$c (J/g^{\circ}C)$	0,385

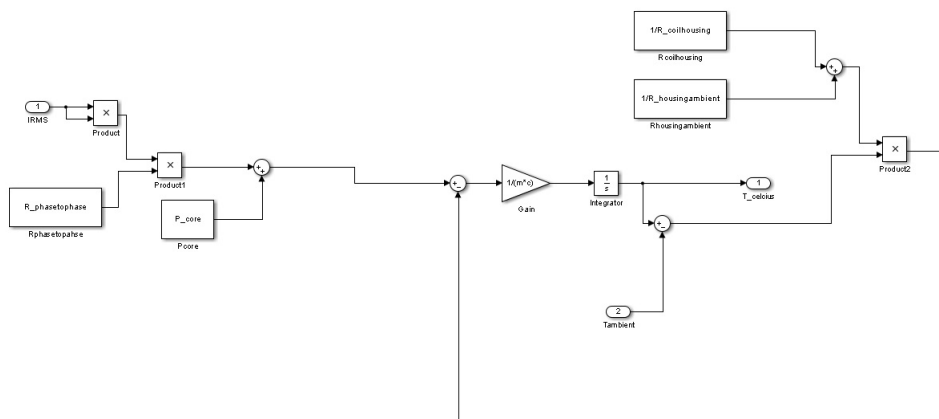


Figure 3.6: Thermal Model of The Motor

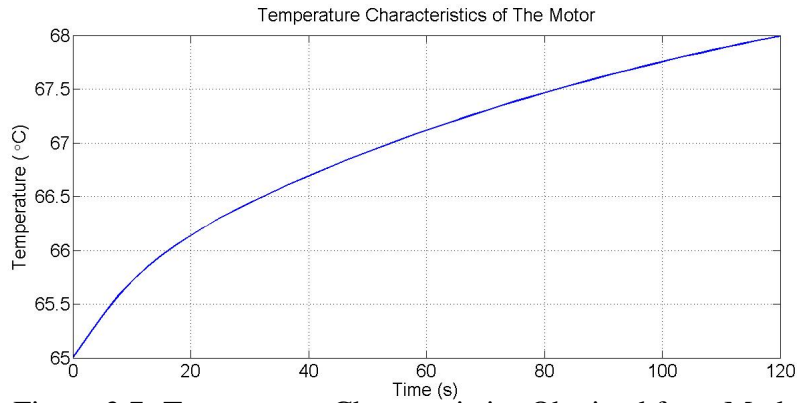


Figure 3.7: Temperature Characteristics Obtained from Model

3.2 Material Selection

In design of a PM BLDC motor, two main material selections are crucial, namely the core material selection and the PM selection. Core materials are used in construction of stator and rotor, and what makes this selection crucial is the magnetic circuit. While designing a motor, one should consider the magnetic circuit and construct an operating point according to the magnetic circuit. In addition, selection of PM is essential; because electromagnetic properties shown in a typical B-H curve determines the operating point of the motor. Therefore, selection of these materials is further discussed throughout this section.

3.2.1 Ferromagnetic Materials

Ferromagnetic materials are the most common magnetic material used in an electrical machine design as a core material for both stator and rotor. Typically, a ferromagnetic material is characterized by its B-H curve. The B-H curve of such materials are constructed by applying sinusoidal excitation with varying amplitude and the response of the material in terms of magnetic flux density and field intensity is measured. Figure 3.8 shows a typical B-H curve of a ferromagnetic material.

The B-H curve tells about the saturation effects of a core used in the motor. In the B-H curve, the point at which magnetic field density value does not increase any longer as the field intensity increases, is called the hard saturation. It is desired to design a motor at a point before hard saturation starts; because the magnetomotive force required to

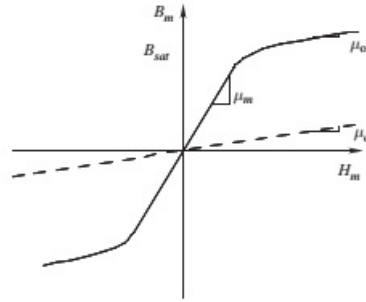


Figure 3.8: Typical B-H Curve of a Ferromagnetic Material (taken from [8])

magnetize the core becomes large and core losses become higher.

While choosing a core material, the losses in the ferromagnetic material should also be considered; because these losses directly affect the efficiency of the motor. The core losses are classified into two major losses, namely the hysteresis losses and the eddy current losses.

Hysteresis losses occur when an external magnetomotive force (MMF) is applied and the appliance of this excitation is removed. That is, when an external magnetic field intensity is applied, magnetic domains in the core material are aligned in a way that the corresponding magnetic field density is obtained. However, if this magnetic field is removed, it is observed that the magnetic domains will not go back to its original position and some residual flux stays in the core material. The point to be noted for hysteresis losses is that, it depends on the B-H curve and hence, the excitation applied on the core material.

Eddy currents, on the other hand, occurs when electric current is induced within the core material when the excitation is applied in a time-varying manner. Induced current circulates within the core material, resulting in a resistive loss due to the resistance inside the material. The main solution in order to decrease this loss is increasing the resistance of the material and hence, using laminations. The total of these losses is called the core loss and, formulations of the losses are further studied later in the chapter related to the design procedure. (see Chapter 4)

In order to select the ferromagnetic material properly for a good design, the effects of the loss to the efficiency must be considered especially. Although the operating temperature in CMG's are crucial, the temperature range of core materials is quite

wide. On the other hand, given formulae for core loss is empirical, and measurement of such losses is difficult. In such cases, the datasheet provided by the manufacturing companies are more important. The datasheets include core loss values in terms of Watts or kilowatts per unit weight. The motor to be designed for this CMG application will operate at a rotor speed of 10000 rpm. For a 2-pole motor, this speed corresponds to an electrical frequency value of $f = n_s p / 120 = 10000 \times 2 / 120 = 166 \text{ Hz}$. Furthermore, if a motor is to be used with higher number of poles such as 6, this value increases up to 500 Hz. Hence, a core material with less core loss, better manufacturing process and less cost must be selected. The ferromagnetic materials produced by Cogent can be preferred as the core material in the design; because Cogent has the capability of manufacturing thin sheet laminations.

In conclusion, the ferromagnet to be used in the design process is selected as Cogent Power no.12 [7]. Core loss data of the material is given Table 3.4, which is a tabulated data provided by the manufacturer. Moreover, the B-H curve of the material is given in Figure 3.9 by the manufacturer. Other necessary parameters during the design process are summarized in Table 3.5. In developing the new designs, it is assumed that the same material is to be used and loss calculations are done using the loss curve described in Table 3.4.

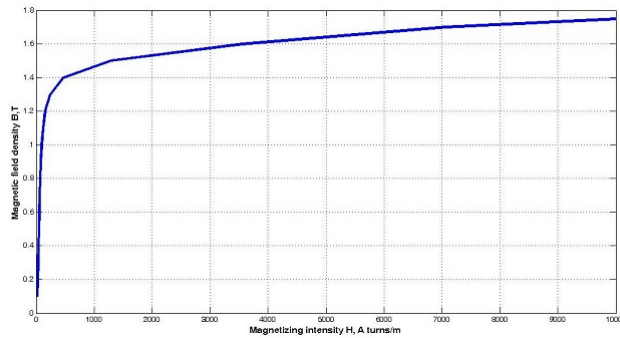


Figure 3.9: B-H Curve of The Core Material (Cogent Power No.12)

3.2.2 Permanent Magnets (PM)

Permanent magnets are critical magnetic materials for a brushless DC motor. Permanent magnets can be thought as magnetic flux generators. As a result, the necessity for a field winding is removed. Permanent magnets are also magnetic materials as described for ferromagnets, and hence it can be characterized by its B-H curve. However; second

Table 3.4: Core Loss Data of Cogent Power No.12

Magnetic Flux Density B (T)	Non-oriented steel core loss (Cogent Power No.12) (W/kg)		
	50 Hz.	400 Hz.	2.5 kHz
0,1	0,02	0,16	1,65
0,2	0,08	0,71	6,83
0,3	0,16	1,55	15,2
0,4	0,26	2,57	25,4
0,5	0,37	3,75	37,7
0,6	0,48	5,05	52
0,7	0,62	6,49	66,1
0,8	0,76	8,09	83,1
0,9	0,32	9,84	103
1	1,09	11,8	156
1,1	1,31	14,1	
1,2	1,56	16,7	
1,3	1,89	19,9	
1,4	2,29	24	
1,5	2,74	28,5	
1,6	3,14		
1,7	3,49		
1,8	3,78		

quadrant of a permanent magnet is investigated for categorization. Second quadrant of a B-H curve is called the demagnetization curve. Knowing basic specifications of a PM makes the construction of a magnetic circuit easier. Typical demagnetization curve of a PM is shown in Figure 3.10. Basic specifications are stated as follows:

- **Remanent Flux Density:** It is the flux density value that a PM can produce by itself. That is, when no external field intensity is applied on a PM, the flux density a PM can generate is the remanent flux density. (denoted as B_r in Figure 3.10)
- **Coercive Field Intensity:** It is the magnetic field intensity value at which the magnetic flux density generated by the PM becomes zero. For a permanent

Table 3.5: Some Parameters of The Ferromagnetic Material

Parameter	Value
Hysteresis coefficient (k_h)	0,0314
Eddy current coefficient (k_e)	2,18E-05
Density (d_{steel}) (kg/m^3)	7650
Relative permeability μ_r	4000

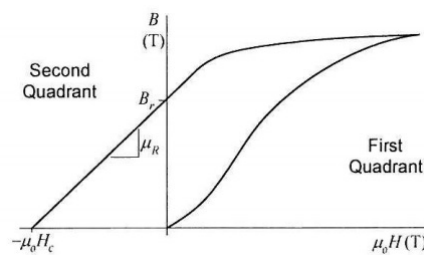


Figure 3.10: Demagnetization Curve of a PM

magnet having a high coercivity implies that a thinner PM can be used for a specific motor design to withstand demagnetization conditions. (denoted as H_c in Figure 3.10)

- **Recoil Relative Permeability:** It is the slope of demagnetization curve of the PM. (denoted as μ_R in Figure 3.10) Typical recoil relative permeability value of a PM lies between 1 and 1.2 .

3.2.2.1 Permanent Magnet Selection Criteria

For space applications, the permanent magnet must be chosen properly such that it must have a high operating temperature range, radiation sensitivity and high corrosion resistance.

As a design and operation constraint, the permanent magnet to be chosen must have a wide operating temperature range. The CMG prototype must operate between (-20) and (+65) $^{\circ}$ C. Temperature dependence is a critical issue for PM selection; because permanent magnets lose their magnetic property as the temperature increases.

Remanent flux value B_r of Samarium-Cobalt(Sa-Co) magnets is affected less than that of Neodymium-Boron(Ne-B) equivalents. In addition, Curie temperature of PM's is essential in selecting a PM. Curie temperature is defined as the maximum temperature value at which a PM loses its whole magnetic properties, that is no remanent flux or coercive field intensity value is measured from the PM. For Samarium-Cobalt permanent magnets, Curie temperature value is around 800 °C, while Neodymium-Boron PM's lie around 330°C. Considering the temperature conditions of the CMG, both values are acceptable. As the final temperature constraint, maximum service temperature is a parameter that must be taken into account. Service temperature is the temperature value at which the thermal property of the magnet degrades such that the magnetic properties cannot be reversed even the ambient or operating temperature decreases. Maximum service temperature of Ne-B permanent magnets are around 110°C, while Sa-Co equivalents are around 330°C. A temperature value of 110°C can be observed in a CMG, so selection of Ne-B permanent magnet may be risky.

As stated above, Sa-Co magnets have a better thermal characteristics. Another aspect that must be pointed out is that these permanent magnets are highly resistant to corrosion. Ne-B equivalents, on the other hand, appear to be more sensitive to the corrosion issues. In order to decrease these effects, Ne-B permanent magnets can be coated with an additional material. Yet, certain precautions must be taken for using a Ne-B permanent magnet. To sum up, Sa-Co based permanent magnets such as VACOMAX 225 HR have considerable thermal properties like thermal conductivity, which makes these materials easy to remove heat on itself.

Additionally, radiation resistance is another issue that must be taken into consideration. Radiation effects are highly dependent on the orbit, as well as the thickness of the material used as a shield; but these effects are hardly known; but what is known is that Sa-Co-based permanent magnets show an insensitive behaviour against radiation whereas Ne-B equivalents degrade in performance depending on the radiation level.

Under these circumstances, due to the fact that Sa-Co permanent magnets have considerably less temperature dependence, higher service and Curie temperature, better thermal conductivity and less radiation sensitivity over Ne-B equivalents. VACOMAX 225 HR (Sm_2Co_{17} B_r at 1.03-1.1 T, H_r at 720-830 A/m) is chosen as the PM material

for the design process. Properties of the selected permanent magnet is given in Table 3.6, as the manufacturer data. As stated in core material selection, the permanent magnet is assumed to be the same as the one used in previous CMG wheel motor design conducted in [7].

Table 3.6: Properties of Selected PM [2]

Property	Value
B_r (T)	1,03 - 1,1
H_c (kA/m)	720 - 820
μ_r	1,06 - 1,34
Temperature coefficient	-0,03
T_{curie} ($^{\circ}C$)	800
$T_{service}$ ($^{\circ}C$)	350
Thermal conductivity (W/(m. $^{\circ}C$))	12

3.3 Magnetic Circuit

As stated before, a PM BLDC includes surface-mounted permanent magnets on rotor, and windings on stator. A 4-pole PM BLDC is shown in 3.11 as an example. Such a motor includes 4 distinct permanent magnets for pole assignment and the magnetic circuit is completed with 2 adjoint opposite assigned (N and S) poles and core material manufactured for stator and rotor.

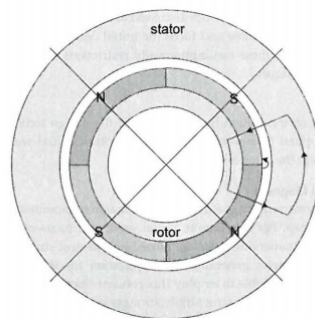


Figure 3.11: Typical BLDC Motor (retrieved from [6])

In designing an electrical motor, modeling of the motor with its magnetic circuit equivalent has importance. This step must be done in a neat way in order to determine the necessary air gap magnetic flux density and find the related operating point, which is the intersection point of the demagnetization curve of the PM and the load line.

Load line is defined by solving the magnetic circuit, relating the air gap magnetic flux density and the corresponding magnetic field intensity. The magnetic circuit equivalent is shown in 3.12. Each permanent magnet is represented as a current source due to the flux generation within itself and a resistance connected in parallel with this source in order to represent its leakage effects. Some of the flux reaches to the other pole through the air gap while the remaining part reaches the other pole through the stator.

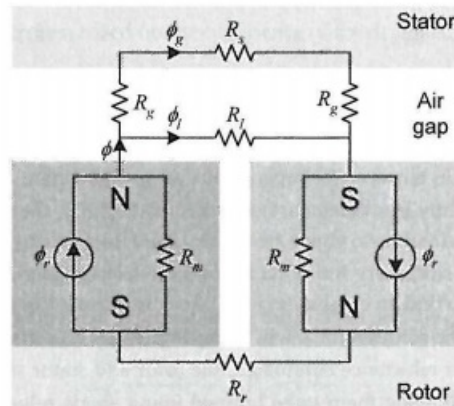


Figure 3.12: Magnetic Circuit of the BLDC Motor (retrieved from [6])

This magnetic circuit model may seem complicated to solve. For this reason, some simplifications can be made on this model. Since rotor reluctance and the magnet on the right are connected in series, they can be swapped. In addition, the leakage effect of the rotor can be neglected when a small flux component is assumed to be flowing as a leakage component. After considering the current sources as a combined current source, the model can be simplified as shown in 3.13.

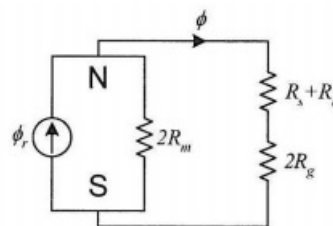


Figure 3.13: Simplified Magnetic Circuit (retrieved from [6])

After constructing the magnetic circuit, one can solve the magnetic circuit and related air gap magnetic flux density. Magnetic flux through the air gap is calculated as in Equation 3.4.

$$\phi = \phi_r \frac{2R_m}{2R_m + 2R_g + 2R_s + R_r} \quad (3.4)$$

In Equation 3.4, the terms R_s and R_r are nonlinear due to the nature of the ferromagnetic material, so the effects of these reluctance must be somehow eliminated or neglected. Thus, it is feasible to make an assumption that the relative permeability of the core is much higher than that of air (i.e. infinitely permeable), and the reluctance components related to them can be added as a perturbation to the air gap reluctance. This addition can be denoted as K_r and called as reluctance factor [6]. Furthermore, due to the leakage effect through the air gap, not all the flux component can flow through rotor and complete the magnetic circuit this way. In order to present this effect, a leakage factor is defined and denoted as K_l , which is a value smaller than 1. Selection of these values depends on the experience due to the fact that an actual calculation of these values in an analytical way is not easy [6]. Effects of these terms on the mathematical model are reflected as shown in Equation 3.5 and Equation 3.6.

$$2R_g + 2R_s + R_r = 2K_r R_g \quad (3.5)$$

$$\phi_g = K_l \phi \quad (3.6)$$

After magnet reluctance and air gap reluctance is defined as in Equation 3.7 and 3.8, the air gap flux expression takes the form shown in Equation 3.10

$$R_m = \frac{l_m}{\mu_0 \mu_{rel} A_m} \quad (3.7)$$

$$R_g = \frac{g}{\mu_0 A_g} \quad (3.8)$$

$$\phi_g = \phi_r \left(\frac{1}{1 + K_r \frac{R_g}{R_m}} \right) K_l \quad (3.9)$$

$$\phi_g = \phi_r \frac{K_l}{1 + K_r \frac{\mu_{rel} g A_m}{l_m A_g}} \quad (3.10)$$

After this point, one should define the terms concentration factor $C_\phi = A_m/A_g$ and the permeance coefficient $PC = l_m/gC_\phi$ and after substituting air gap magnetic flux density $B_g = \phi_g/A_g$ and magnet flux density $B_r = \phi_r/A_m$, the final expression takes the form as in Equation 3.11.

$$B_g = \frac{K_l C_\phi}{1 + K_r \frac{\mu_R}{PC}} B_r \quad (3.11)$$

If a motor is to be designed according to the air gap flux density as defined in Equation 3.11, it is worth noting that the leakage factor K_l can be taken between 0.9 and 1.0 and reluctance factor K_r lies between 1.0 and 1.2, and concentration factor is taken as the ideal value, which is 1.0 [6]. For a motor to be designed, the magnet remanent flux density can be thought as constant. In this case, only parameter to be changed is the permeance coefficient PC . That is, changing the magnet thickness and the air gap plays an important role in design process. To sum up, if it is desired to obtain a proper air gap magnetic flux density value, either air gap or magnet length can be arranged for a better design.

3.4 Back emf and Torque Equations for PM Brushless DC Motors

This section briefly states the torque expressions of the main motor topologies under investigation. As an initial step, design starts with the excitation and the pole number and related torque equation must be used while determining the sizes of the motor. A set of proposed designs as radial-flux outer-rotor topology is going to be presented in following chapters by using the equations given in the following sections. However, designed motors are going to be compared with the axial-flux 6-pole squarewave equivalent designed by [7]. Thus, in order to provide a complete set of equations, torque equations related to axial-flux are additionally stated.

3.4.1 Back EMF and Torque

In the very general case, the back emf of a motor is obtained by the Faraday's Law of Induction, which is denoted in Equation 3.12.

$$e_b = \frac{d\lambda}{dt} = \frac{d\lambda}{d\phi_e} \frac{d\phi_e}{dt} = \frac{2N\phi_g}{\pi} \omega_e = \frac{2N\phi_g}{\pi} \frac{N_p}{2} \omega_m \quad (3.12)$$

After substituting the ϕ_g as shown in Equation 3.16, the final expression for back emf can be obtained.[14].

$$\phi_g = B_g A_g \quad (3.13)$$

$$A_g = R_{in} \phi_p L \quad (3.14)$$

$$\phi_p = 2\pi / N_p \quad (3.15)$$

$$e_b = 2NB_g LR_{in} \omega_m \quad (3.16)$$

3.4.2 Radial Flux Motor Equations

3.4.2.1 Back emf and Torque Equations under Sinusoidal Excitation

In sinusoidal excitation, it assumed that all the phase currents are sinusoidal and these phases are all in conduction during the commutation. It is further assumed that only fundamental component in the back emf voltage creates the necessary torque. The starting point in calculating the torque is that all three phase components are conducting and the electromechanical torque is produced. Therefore, the electromechanical torque is calculated as shown in Equation 3.17.

$$\tau = \frac{3e_{rms} I_{rms}}{\omega_m} \quad (3.17)$$

In order to obtain the rms of back emf voltage, first one must obtain the peak value as calculated in Equation 3.20.

$$e_{peak} = -\omega_{elec} \frac{d\lambda}{d\theta} \quad (3.18)$$

$$\frac{d\lambda}{d\theta} = N_{ph} A_g B_{gav} \quad (3.19)$$

$$e_{peak} = \frac{\pi}{2} \omega_m N_{ph} B_{gav} D_i L \quad (3.20)$$

$$e_{rms} = \frac{e_{peak}}{\sqrt{2}} \quad (3.21)$$

Using Equation 3.17 and Equation 3.21, torque expression can be modified in terms of related sizes.

$$\tau = \frac{3\pi}{2\sqrt{2}} N_{ph} B_{gav} D_i L I_{rms} \quad (3.22)$$

Electrical loading is defined as in Equation 3.23.

$$q = \frac{2m N_{ph} I_{rms}}{\pi D_i} \quad (3.23)$$

where m is number of phases, N_{ph} denotes number of turns per phase, I_{rms} denotes the rms current, and D_i denotes the bore diameter. Throughout this thesis, 3-phase motor designs are proposed; hence the number of phases value m will be taken as 3 and electrical loading will be expressed as in Equation 3.24.

$$q = \frac{6 N_{ph} I_{rms}}{\pi D_i} \quad (3.24)$$

After substituting I_{rms} in Equation 3.24 into Equation 3.22, final expression for torque is obtained in 3.25 [7].

$$\tau = \frac{\pi^2}{4\sqrt{2}} B_{gav} q D_i^2 L \quad (3.25)$$

3.4.2.2 Back emf and Torque Equations under Squarewave Excitation

In squarewave excitation, two phases are in conduction during a commutation interval, and a trapezoidal current is used, whose peak value is the dc link current. The electromechanical power is expressed as shown in Equation 3.26.

$$P_{em} = 2E_{ph} I_{DC} = \tau_{em} \omega_{mech} \quad (3.26)$$

where E_{ph} is the flattop value of the phase back emf, I_{DC} is the DC link current, ω_{mech} is the mechanical speed of the motor and τ_{em} is the electromechanical torque generated. Typically, DC link current has a trapezoidal characteristic and has an angle of 120° electrically. If the rms value of this current waveform is to be calculated, the expression in Equation 3.27 is used.

$$I_{rms} = \sqrt{\frac{2}{3}} I_{DC} \quad (3.27)$$

In order to calculate the flattop phase back emf, following set of equations are used.

$$\lambda = N_{ph}\phi_g \quad (3.28)$$

$$e = -\frac{d\lambda}{dt} = -\frac{d\lambda}{d\theta_{elec}} \frac{d\theta_{elec}}{dt} = -\omega_{elec} \frac{d\lambda}{d\theta_{elec}} \quad (3.29)$$

$$\phi_g = B_g A_g = B_g \theta_{mech} R_i L = B_g \frac{2}{P} \theta_{elec} R_i L \quad (3.30)$$

$$E_{ph} = \frac{P}{2} \omega_{mech} \frac{2N_{ph}\phi_g}{\theta_{elec}} \quad (3.31)$$

$$E_{ph} = N_{ph} B_g L D_i \omega_{mech} \quad (3.32)$$

By substituting Equation 3.24 in I_{rms} , and Equation 3.32 in Equation 3.26 and solve for τ_{em} , one can get the final torque expression for squarewave excitation, as shown in Equation 3.33 [7].

$$\tau_{em} = \frac{\pi}{\sqrt{6}} B_g q D_i^2 L \quad (3.33)$$

3.4.3 Axial Flux Motor Equations

3.4.3.1 Back emf and Torque Equations under Sinusoidal Excitation

Equations to be derived for AF BLDC motors have the same concepts as that for RF motors. The difference in the geometry of AF motors must be taken into consideration and the derivations must be made accordingly. The assumptions made for RF motors are valid in AF motors. That is, only the fundamental component of the air gap magnetic flux density creates the desired torque.

Peak back emf value can be obtained as shown between Equation 3.34 and Equation 3.37.

$$e_{peak} = \frac{P}{2} \omega_{mech} N_{ph} B_{gav} \pi \frac{(R_o^2 - R_i^2)}{P} \quad (3.34)$$

$$= \frac{\pi}{2} \omega_{mech} N_{ph} B_{gav} (R_o^2 - R_i^2) \quad (3.35)$$

$$K_r = \frac{R_i}{R_o} \quad (3.36)$$

$$e_{peak} = \frac{\pi}{2} \omega_{mech} N_{ph} B_{gav} R_o^2 (1 - K_r^2) \quad (3.37)$$

$$e_{rms} = \frac{e_{peak}}{\sqrt{2}} \quad (3.38)$$

Torque can be defined as the same as shown in Equation 3.17. The expression found in Equation 3.37 is inserted in the torque expression and resulting expression after I_{rms}

is replaced with Equation 3.24 is given in Equation 3.40.

$$\tau_{em} = \frac{3\pi}{2\sqrt{2}} N_{ph} B_{gav} R_o^2 (1 - K_r^2) I_{rms} \quad (3.39)$$

$$= \frac{\pi^2}{\sqrt{2}} B_{gav} q R_o^3 K_r (1 - K_r^2) \quad (3.40)$$

3.4.3.2 Back emf and Torque Equations under Squarewave Excitation

While calculating the torque expression related to the squarewave excitation of the AF motors, the initial point will also be the same as the derived expressions for RF motors. Electromechanical power produced by such motors is expressed as stated in Equation 3.26.

The flux at air gap in AF motors is stated as in Equation 3.41.

$$\phi_g = B_g A_g = B_g \frac{\pi(R_o^2 - R_i^2)\theta_{mech}}{P\pi} \quad (3.41)$$

E_{ph} , in addition, can be expressed as shown in Equation 3.45.

$$\lambda = N_{ph}\phi_g \quad (3.42)$$

$$E_{ph} = -\frac{d\lambda}{dt} = -\frac{d\lambda}{d\theta_{elec}} \frac{d\theta_{elec}}{dt} \quad (3.43)$$

$$= \frac{P}{2} \frac{2N_{ph} \theta_{mech} (R_o^2 - R_i^2)}{\theta_{mech} P} \omega_{mech} B_g \quad (3.44)$$

$$= N_{ph} B_g R_o^2 (1 - K_r^2) \omega_{mech} \quad (3.45)$$

$$K_r = \frac{R_i}{R_o} \quad (3.46)$$

After substituting E_{ph} found in Equation 3.45, one can obtain the torque expression as shown in Equation 3.47.

$$\tau_{em} = 2N_{ph} B_g R_o^2 (1 - K_r^2) I_{DC} \quad (3.47)$$

Substitution of I_{DC} with its rms equivalent in Equation 3.47 and modifying the expression for electrical loading q yields the form given in Equation 3.48 .

$$\tau_{em} = \frac{2\sqrt{2}\pi}{\sqrt{3}} B_g q_i R_o^3 K_r (1 - K_r^2) \quad (3.48)$$

3.5 Literature Survey

In literature, there are several findings and results on the area of CMG designs and the motor topologies related to CMG applications.

Radial flux motors can be used when relatively long shafts are to be included. As the pole number increases, the torque capability of the motor increases but after a certain increase, the increase in pole number leads to a decrease in torque capability; because core losses inside the motor tend to increase. Furthermore, for an AF motor, making a design with a small axial length, these motors are capable of delivering more torque [15].

In [16], it is stated that an axial-flux topology has advantages on CMG applications compared to the radial-flux topologies. Furthermore, increase in the pole number and repeating the motor design process reduces the motor volume dramatically, which is also discussed by [17], stating that single-sided axial-flux machines have a volumetric advantage when compared to the radial-flux equivalents. [18] discusses the advantages between RF topology and AF topology. According to [18], RF topologies show a slightly better torque performance than AF topology, under the circumstances that D_i/L ratio does not exceed the value of 5. [12] gives a comprehensive information about design guidelines, control strategies, cooling methods, PM selection and presents the engineering tools used in a typical electrical motor design process as a FEA solution. In [19], basic derivations are done for motors under different application types. These include the maximum torque and acceleration limits, and acceleration capability is presented for different applications. Reducing cogging torque effects in a permanent magnet motor is well stated in [20], by explaining the effects of skewing, applying a pole arc and defining notches in the stator teeth.

In general, there are not many papers on CMG design. Some patents such as [3] explains the general working principles of the Control Moment Gyroscopes and states that the main electrical motor used in such systems are brushless DC electrical motors. In addition, [9] presents a comprehensive study on attitude control systems based on Control Moment Gyroscopes. Here, [9] explains the working principles of these systems clearly. Similar observations are made by [21] by explaining the Control

Moment Gyroscope types and the configurations in a typical satellite system.

In the next chapter, the design procedure of an outer-rotor brushless DC motor is going to be stated, and necessary equations for sizing and performance are going to be provided.

CHAPTER 4

DESIGN PROCEDURE OF OUTER-ROTOR BRUSHLESS DC MOTOR TOPOLOGIES

This chapter describes the design procedure for proposed brushless DC motor topology. First, equations are derived for RF motor topology under sinusoidal excitation case, both for 2-pole topology and 6-pole topology. Then, the same procedure is summarized for squarewave excitation, again for both 2-pole and 6-pole topologies.(see Figure 4.1)

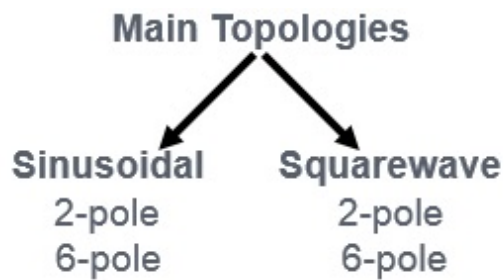


Figure 4.1: Division of The Topologies

4.1 Introduction to the Design of an Outer-Rotor Permanent Magnet Brushless DC Motor Configuration

The structure of an outer-rotor BLDC PM motor is given in Figure 4.2. In an outer-rotor configuration, the locations of stator and rotor are made inside out. That is, the stator of the motor is placed inside the rotor, and the rotor is placed outer side of the motor. Main advantage of such system is that no slip ring is required while achieving the electromechanical energy conversion, which is the same as a typical PM brushless

DC motor. It is assumed that the excitation of the windings are achieved through the hollow shaft inside the stator part. Another main advantage of such configuration is that inertia of the motor is made larger with respect to the inner-rotor equivalent and hence, inertia contribution of the motor is increased. A final advantage of designing such a motor is that a more flat and pancake-like topology can be integrated to the system, which in turn makes a minimized volume design.

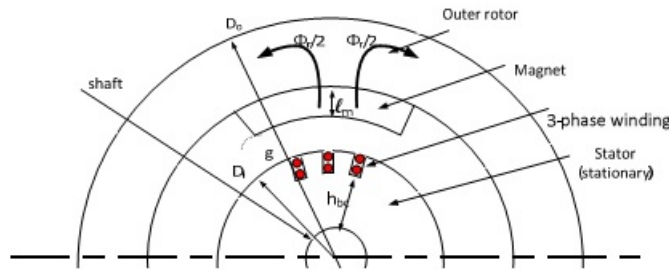


Figure 4.2: Structure of an Outer-Rotor BLDC Motor

4.1.1 Preliminary Design Considerations

In this study, the motor to be designed must operate at a constant speed of 10000 rpm. Such a rotor speed corresponds to a supply frequency of approximately 166 Hz. For the application here, the material selected has 0.35 mm lamination thickness and the core loss is as stated in Table 3.4, in Chapter 3. The core loss, P_{core} at other frequencies and flux densities will be approximated in 4.2.5.

4.2 Design Procedure of RF Motors under Sinusoidal Excitation

After considering the main aspects of an outer-rotor motor topology, it is needed to develop a mathematical model for the design process. In other words, the torque expressions must be related with the characteristic sizes of the motor, as well as the electrical and magnetic loading of the motor. In this manner, the first task is to establish a magnetic circuit of the topology under investigation. Next, the derivations are going to be handled for sizing of the motor with the use of winding aspects considering the pole number and excitation type. Then, equivalent circuit parameters such as phase resistance and phase inductance are going to be calculated. Finally, the parameters classifying the motor performance such as losses are going to be handled and the

motor volume and mass is approximated. In this manner, the calculations are handled according to the pole number and the excitation types, respectively. In this context, the sinusoidal excitation case is investigated in this section, for both 2-pole and 6-pole topologies. Afterwards, the squarewave excitation case is going to be discussed, again for both 2-pole and 6-pole topologies.

4.2.1 Magnetic Circuit of RF Motors

Generally, a PM is assumed to be a constant flux generator, which is denoted as ϕ_r and this flux is expressed as seen in Equation 4.1. The magnetic circuit of the outer-rotor configuration is shown in Figure 4.3. In this figure, magnet flux ϕ_r is represented by a current source [14]. Other elements of the circuit represented by the symbol R denote the reluctance of each magnetic circuit element and symbols shown by P denote permeance of the related part of the magnetic circuit. These will be briefly explained before progressing with how this circuit is used for design purpose.

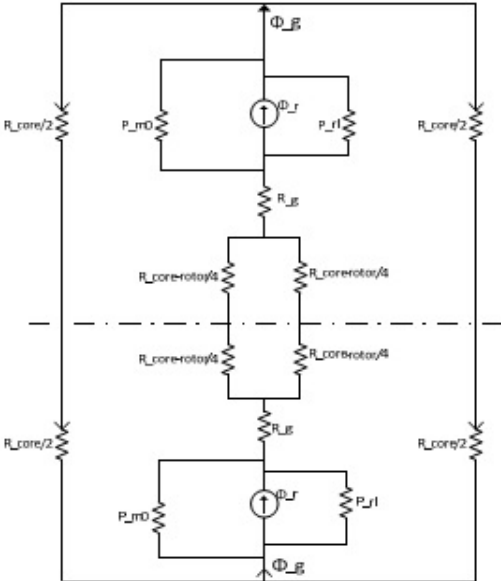


Figure 4.3: Magnetic Circuit of Outer-Rotor BLDC Motor

$$\phi_r = B_r A_m \tag{4.1}$$

Some of the flux generated by the PM circulates around itself due to the internal permeance of PM. This is represented as in Equation 4.2

$$P_{m0} = \frac{\mu_0 \mu_{rec} A_m}{l_m} \quad (4.2)$$

where μ_0 is the permeability of vacuum, μ_{rec} is the relative permeability of the PM, A_m is the magnet area and l_m is the magnet length. Magnet area is considered as 120° of magnet span and calculated according to the length at the middle, which indeed gives a mean length when a 2-pole motor is considered. Furthermore, magnet area is calculated as in Equation 4.3.

$$A_m = \alpha(R_i + g + l_m/2)L \quad (4.3)$$

In Equation 4.3, R_i denotes the stator radius, g denotes the air gap, L denotes the axial length, and α denotes arc angle of the PM in radians. That is, if the magnet arc angle is to be taken as 120°, then the term α becomes $\frac{2}{3}\pi$. By adding the rotor leakage effects, denoting as P_{rl} and corresponding to a value of 10% of the internal permeance of the internal permeance [14], the total permeance of the magnet is calculated in Equation 4.4. Additionally, the reluctance of the air gap is calculated as shown in Equation 4.5.

$$P_m = P_{m0} + P_{rl} = P_{m0} + 0.1P_{m0} = 1.1P_{m0} \quad (4.4)$$

$$R_g = \frac{g'}{\mu_0 A_g} \quad (4.5)$$

where g' is the equivalent air gap calculated with the expression $g' = K_c g$ in which K_c denotes the Carter's Coefficient, and A_g is the area of the air gap. Carter's Coefficient must be taken into consideration in cases where slotting affects the mean air gap. In this study, Carter's Coefficient can be assumed to be as 1.05 [14]. Except from the air gap, the reluctance of the air gap is dependent on the area of the air gap area and this area is calculated as shown in Equation 4.6, following the same idea as the calculation of magnet area.

$$A_g = (\alpha(R_i + g/2) + 2g)(L + 2g) \quad (4.6)$$

The reluctance of the flux path in the stator core is calculated from Equation 4.7. In

Equation 4.7, μ_{core} is the permeability of the flux path and l_{core} is the length of the flux path (uniform flux distribution path is assumed) and calculated as in Equation 4.8. Furthermore, area of the core is calculated as shown in Equation 4.9.

$$R_{core} = \frac{l_{core}}{\mu_{core}A_{core}} \quad (4.7)$$

$$l_{core} = \frac{\pi(D_i + D_o)}{2p} \quad (4.8)$$

$$A_{core} = \frac{L}{2}(D_o - D_i) \quad (4.9)$$

where D_o is the outer diameter of the core. In Equation 4.6, the core length is extended by a “2g” term in order to take into account the fringing flux at the ends of the core and give a proper margin. The air gap flux is assumed to cross the air gap only through the magnets and is calculated from 4.10.

$$\phi_g = \frac{\phi_r}{1 + P_m(R_g + \frac{R_{core}}{4})} \quad (4.10)$$

It must be noted that, this flux can also be written in terms of average air gap flux density as in Equation 4.11.

$$B_g A_g = \frac{B_r A_m}{1 + P_m(R_g + \frac{R_{core}}{4})} \quad (4.11)$$

The operating point of the magnet can be determined from the equivalent circuit, and is found to be given by 4.12

$$B_m = \frac{1 + P_r l (R_g + \frac{R_{core}}{4})}{1 + P_m (R_g + \frac{R_{core}}{4})} B_r \quad (4.12)$$

Now, the magnet flux density at the operating point B_m is determined for a given geometry, using the slope of the B-H curve, magnetizing force H_m can be calculated using Equation 4.13.

$$-H_m = \frac{B_r - B_m}{\mu_0 \mu_{rec}} \quad (4.13)$$

After substituting B_r in 4.12 into 4.13, load line characteristics for the magnet can be found as in Equation 4.14.

$$B_m = \mu_0 \mu_{rec} H_m \left(\frac{1 + P_{rl} \left(R_g + \frac{R_{core}}{4} \right)}{P_{m0} R_g} \right) \quad (4.14)$$

The equations above describe how to establish the magnetic equivalent circuit of an outer-rotor RF PM motor; given its dimensions and the properties of the core material and the magnet. Once B_m , the operating point of the magnet is known, the flux densities of various parts of the motor magnetic circuit can be found.

4.2.2 Determination of Motor Dimensions for Sinusoidal Excitation

In the design process, the torque requirement and the torque expression related to the certain excitation is the main starting point. Previously, it was stated that the torque produced by the motor (τ_p) can be found from Equation 4.15 in case the BLDC motor is excited from a sinusoidal voltage source.[22].

$$\tau_p = \frac{\pi^2}{4\sqrt{2}} B_{gav} q D_i^2 L \quad (4.15)$$

In Equation 4.15, B_{gav} is the average flux density in the air gap, q is the electrical loading, D_i is the inner diameter and L is the axial length of the motor. B_{gav} and q terms are given in Equations 4.16 and 4.17, respectively.

$$B_{gav} = \frac{\phi_{pole}}{A_{pole}} \quad (4.16)$$

$$q = \frac{6N_{ph} I_{rms}}{\pi D_i} \quad (4.17)$$

where ϕ_{pole} denotes the flux at each pole and A_{pole} denotes the pole area in Equation 4.16. In Equation 4.17, N_{ph} denotes the number of turns per phase and I_{rms} denotes

the rms current. Electrical loading basically clarifies total magnetomotive force per unit length. Hence, number of turns per phase value must be first multiplied by 3 for total number of turns, and total number of turns value must be multiplied by 2 for total number of conductors within the motor. That is why the term 6 appears in Equation 4.17.

B_{gav} is a measure of saturation of the magnetic circuit and depends on the material used as the core. This parameter is also related to core loss. q , on the other hand, is related to copper loss and therefore is limited by the type of cooling. Previous study conducted in [7] indicates that the current loading up to 6000 A/m can be handled by the motor while the motor is accelerating with current density of $J=7 \text{ A/mm}^2$ in the conductors. Once the motor reaches its steady-state speed, it is found that current density falls down to 3 A/mm^2 and the motor temperature remains within acceptable limits.

One of the purposes of the investigation here is to compare the performance of the two-rotor axial-flux PM motor designed in [7] with the outer-rotor radial-flux PM motor. Because of this reason, both motors are designed with the same core material. As in the axial flux motor design in [7], the value of the average air gap flux density is limited to 0.43 T. The maximum flux density in any part of the motor is kept below 1.4 T, so that the material magnetic characteristics remain in its linear region and the core loss is low.

At this point, the main aim here is to minimize the volume and the mass of the motor with higher inertia and efficiency and to determine the main dimensions of the motor, so that the motor is capable of producing the desired torque both in transient and steady-state, satisfying the following requirements:

- Average air gap magnetic flux density B_{gav} must be 0.43 T, which is taken as the same that in [7].
- $J_{Cu} = 7 \text{ A/mm}^2$ and less than 3 A/mm^2 at steady-state.
- Electrical loading q must be less than 6000 A-turn/m during starting and less than 3000 A-turn/m at steady-state.
- Acceleration torque must be 50 mN-m maximum.

- Steady-state torque (at 10000 rpm) must be 32 mN-m. This value is set so that the net torque becomes zero and motor continues to operate without any acceleration.
- The flux density in other parts of the core must be 1.4 T maximum. The average air gap magnetic flux density is taken as 0.43 T. This create a constraint that the average magnetic flux density at the core material must become 2 times the average air gap magnetic flux density, which is 0.86 T. The peak value of such averaged flux density value is found simply by multiplying with $\pi/2$, which makes 1.35 T. Hence, a core flux density of 1.4 T is an acceptable value due to the fact the core material starts to saturate after 1.4 T.

The problem can be handled in a simple way by setting the average air gap magnetic flux density B_{gav} as 0.43 T and the current density of the copper to its maximum value, which is 7 A/mm^2 .

The problem is now determination of basic dimensions such as slot area A_{slot} , slot depth h_s , back core length h_{sbc} , inner diameter D_i , core length L and the outer-diameter of the motor D_o .

The slot width and the tooth width are assumed to be equal in order to reduce the number of unknowns. Therefore, three parameters are left unknown, namely h_s , D_i and L , where h_s and h_{sbc} are dependent variables. Therefore, we need three equations to solve the required variables. However, there are two known constraints, which are the current density J_{Cu} and the average air gap flux density B_{gav} . Therefore, $R_{DL} = D_i/L$ ratio is chosen as a parameter so that the number of unknowns is reduced to two.

In the calculations below the shaft diameter D_{shaft} is chosen as 5 mm and is kept constant throughout the whole design process. The flux density behind the slots B_{sbc} can be written as shown in Equation 4.19.

$$\phi_{pole} = B_{gav} A_{pole} \quad (4.18)$$

$$\phi_{sbc} = B_{sbc} A_{sbc} \quad (4.19)$$

$$\phi_{sbc} = \frac{\phi_{pole}}{2} \quad (4.20)$$

$$A_{pole} = \frac{\pi D_i L}{p} \quad (4.21)$$

$$A_{sbc} = h_{sbc} L \quad (4.22)$$

$$B_{gav} \frac{\pi D_i L}{2p} = B_{sbc} h_{sbc} L \quad (4.23)$$

In addition, the back core depth h_{sbc} is expressed as in Equation 4.24.

$$h_{sbc} = \frac{D_i - 2h_s - D_{shaft}}{2} \quad (4.24)$$

By substituting Equation 4.24 in Equation 4.18, one can solve the quadratic equation and slot depth h_s can be found as in Equation 4.25.

$$h_s = \frac{1}{2} \left[D_i \left(1 - \frac{B_{gav} \pi}{B_{sbc} p} \right) - D_{shaft} \right] \quad (4.25)$$

It must be noted that the flux density at back core B_{sbc} is a dependent variable, which is a function of D_i . In addition, electrical loading of a motor can also be expressed as shown in Equation 4.26.

$$q = \frac{J_{Cu} K_{Cu} A_{slot}}{\pi D_i} \quad (4.26)$$

where J_{Cu} is the current density of the copper wire, K_{Cu} is the slot fill factor (taken 0.4 here) and A_{slot} is the total slot area. A_{slot} can be expressed as shown in Equation 4.27. It must be noted that, the total number of slots are taken as 18 throughout the design process. Since 3-phase designs are going to be handled with 2-pole and 6-pole topologies, the chosen slot number is acceptable.

$$A_{slot} = \frac{\pi}{2} \left[\left(\frac{D_i}{2} \right)^2 - \left(\frac{D_i}{2} - h_s \right)^2 \right] \quad (4.27)$$

After substituting the slot depth h_s found in Equation 4.25 in Equation 4.27, and the resulting expression in 4.26, the electrical loading expression also becomes a function of D_i , as shown in 4.28.

$$q = \frac{J_{Cu}K_{Cu}}{2D_i} \left[\left(\frac{D_i}{2} \right)^2 - \left(\frac{D_i}{2} - h_s \right)^2 \right] \quad (4.28)$$

The torque equation of the electrical motor under sinusoidal excitation was previously stated as in the form in Equation 4.15. When it is written by substituting R_{DL} and is solved for electrical loading, the equation takes the following form, as in Equation 4.29.

$$q = \frac{\tau_p R_{DL}}{\frac{\pi^2}{4\sqrt{2}} B_{gav} D_i^3} \quad (4.29)$$

The electrical loading values expressed as in Equation 4.29 and Equation 4.28 are both functions of D_i . All other parameters in the expressions such as peak torque τ_p , average air gap flux density B_{gav} , current density J_{Cu} , slot fill factor K_{Cu} are known, and ratio R_{DL} can be changed easily. Therefore, for a given value of R_{DL} ; D_i can be solved from Equation 4.29. In addition, h_s can be calculated from Equation 4.25. It must be noted that D_o can be calculated from Equation 4.30.

$$D_o = D_i + 2g + 2l_m + 2h_{sbc} \quad (4.30)$$

4.2.3 Winding Design

After sizing is handled, the winding design must be made, so that the current density requirement is met and the resulting winding fits into the slots properly. While doing this, one must make sure that the electrical loading limits are not exceeded. Once these dimensions are found, it becomes possible to adjust the inertia to the desired value (by increasing the rotating rotor frame thickness, namely the outer diameter D_o) and compare the resulting volume and mass of the new design with other designs.

After the main sizes are obtained, the next task is considering the windings. The motor in this work is supplied from a DC bus whose minimum voltage level is 18V. Therefore, the winding design is made so that, even at this DC bus level, the motor meets the requirements. The peak value of the line-voltage level, at minimum DC bus voltage is estimated to be 16 V, taking into account the semiconductor voltage

drop of the inverter. In that case, the phase voltage is calculated by multiplying with $1/\sqrt{3}$, and the rms value is found by multiplying with $1/\sqrt{2}$. Hence, e_{rms} is taken as $16/\sqrt{6} = 6.532Volt$ as a design constraint. Therefore the number of turns per phase N_{ph} can be calculated from Equation 4.31.

$$N_{ph} = \frac{2\sqrt{2}e_{rms}}{\pi B_{gav} D_i L \omega_m} \quad (4.31)$$

where ω_m denotes the mechanical speed of the rotor. Furthermore, the rms phase current can be calculated from Equation 4.32.

$$I_{rms} = \frac{q\pi D_i}{6N_{ph}} \quad (4.32)$$

Current is calculated in order to obtain the loss data of the motor, both for acceleration and steady-state period of the motor. Copper losses are calculated with the knowledge of the current value and the electrical loading characteristics are obtained in order to check whether the specified constraints (an electrical loading of 6000 A-t/m) are satisfied or not.

Following this procedure, the dimensions of the motor that meets the requirements and constraints can be obtained as well as its winding details. Calculated dimensions and sizes for different R_{DL} values are presented in Chapter 5.

4.2.4 Equivalent Circuit Parameters

Equivalent circuit parameters are calculated in order to extract the performance characteristics of the design under investigation. The main aim here is that all the losses are calculated with the help of equivalent circuit parameters and efficiency value is extracted accordingly using the equivalent circuit of the motor shown in Figure 4.4.

4.2.4.1 Phase Resistance

At the very basic level, the phase resistance is calculated as shown in Equation 4.33.

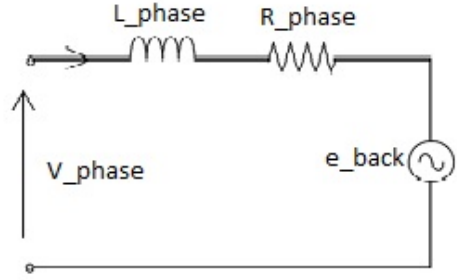


Figure 4.4: Equivalent Circuit of BLDC Motor (per phase)

$$R_{ph} = \frac{\sigma_{Cu} l_{Cu}}{A_{Cu}} = \frac{\sigma_{Cu} (MLC) N_{ph}}{A_{co}} \quad (4.33)$$

Here, l_{Cu} denotes the conductor length, σ_{Cu} denotes the resistivity of the conductor (which is $1,72 \cdot 10^{-8} \Omega - m$ for copper), A_{Cu} denotes the conductor area. The term MLC expresses the mean length of the conductors, which is a geometry-dependent term for different motor types. In this case, the mean length can be calculated as in Equation 4.34.

$$MLC = \left(\frac{\pi(D_i - h_s/2)}{p} + 2L \right) + 2(0.007) \quad (4.34)$$

Here, it is considered that a single wire passes in the middle of the slot, which is $h_s/2$ away from the edge of the stator. The first term is added to the axial length terms due to the end turn. In addition, two "7-mm" terms are added due to proper bending of the wires. Area of the conductor is calculated as in Equation 4.35 .

$$A_{Cu} = \frac{I_{rms}}{J} = \frac{q\pi D_i}{6N_{ph}J} \quad (4.35)$$

4.2.4.2 Phase Inductance

Phase inductance is consisted of three main components, namely air gap inductance, end-turn inductance and the slot leakage inductance. In order to calculate the air gap inductance, the equivalent circuit per pole must be taken into consideration. [7]

The linkage flux is expressed as in Equation 4.36.

$$\lambda_s = N\phi_{sbc} \quad (4.36)$$

$$\lambda_s = \frac{L}{I} \quad (4.37)$$

$$\phi_{sbc} = \frac{NI}{2R_g + 2R_m} \quad (4.38)$$

$$L = \frac{N^2}{2R_g + 2R_m} \quad (4.39)$$

$$L_g = \frac{P}{2}L \quad (4.40)$$

Furthermore, the slot leakage inductance can be found depending on the geometry of the slot. It is assumed that the slot width is taken to be equal to the tooth width previously. For a slot geometry given as in 4.5, the corresponding slot leakage can be found as expressed in Equation 4.41.

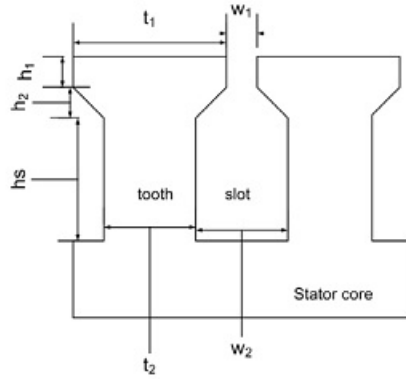


Figure 4.5: Typical Tooth-Slot Geometry

$$L_{sl} = n_c(2N_c^2) \left[\frac{\mu_0 h_s L}{3w_2} + \frac{\mu_0 h_2 L}{\frac{w_1 + w_2}{2}} + \frac{\mu_0 h_1 L}{w_1} \right] \quad (4.41)$$

where N_c denotes the total number conductors in slot, n_c denotes the total number of slots per phase. After considering the slot leakage inductance, the final component for inductance remains to be the end turn inductance. For the calculation of the end-turn inductance, the geometry is taken as shown in 4.6, and the corresponding inductance value is calculated using Equation 4.42.

$$L_e = \frac{n_c \mu_0 T_{cp} N_c^2}{8} \ln \left(\frac{T_{cp} \sqrt{\pi}}{\sqrt{2A_{slot}}} \right) \quad (4.42)$$

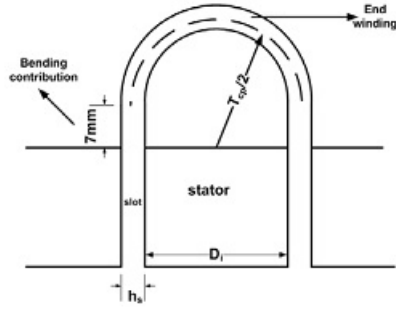


Figure 4.6: End Turn Geometry for Calculation of End-Turn Inductance

$$A_{slot} = w_2 h_s + \frac{w_1 + w_2}{2} h_2 + h_1 w_1 \quad (4.43)$$

4.2.5 Losses

Basically, the losses in an electromechanical environment are due to wiring and the core material, as stated in Chapter 3. These losses are called as resistive losses and core losses, respectively. Resistive losses represent the heat dissipation of the wires due to their resistance, and the core losses represent the heat dissipation due to the changing magnetic field in a core material. Core losses consist of hysteresis losses and eddy current losses. These losses are expressed as in Equation 4.46 .

$$P_h = k_h f B^n \quad (4.44)$$

$$P_e = k_e f^2 B^2 \quad (4.45)$$

$$P_{core} = P_h + P_e \quad (4.46)$$

where k_h is the hysteresis coefficient and k_e is the eddy current coefficient, both of which are material-dependent constant coefficients. Furthermore, f is the electrical frequency, B is the peak magnetic flux density reached in the core. By using the equations above, one can obtain the core loss P_{core} in terms of Watts per unit mass (Watts/kg) . Hence, this quantity must be multiplied with the total mass of the core material in order to obtain the total core loss value. The term n is called Steinmetz exponent and varies between 1.5 and 2.5, depending on the core material. For a typical iron core, it can be taken as 1.6 . In this study, the Steinmetz exponent will be taken as

2 [23]. Core loss parameters are taken from Table 3.4, as stated in Chapter 3.

Resistive losses are calculated as shown from Equation 4.47 to Equation 4.50.

$$P_{copper} = 3I_{in-rms}^2 R_{ph} \quad (4.47)$$

$$I_{in-rms} = I_{rms} + \frac{P_{core}}{3V_{ph-rms}} \quad (4.48)$$

$$V_{ph-rms} = \sqrt{(ZI_{rms})^2 + e_{rms}^2} \quad (4.49)$$

$$Z = \sqrt{(\omega L_{ph})^2 + R_{ph}^2} \quad (4.50)$$

where P_{copper} denotes the resistive loss, I_{in-rms} denotes the input current in rms form, R_{ph} and L_{ph} are the phase resistance and phase inductance, respectively, I_{rms} is the rms current, P_{core} denotes the core losses, V_{ph-rms} denotes the phase voltage in rms form and Z denotes the total phase impedance.

4.2.6 Motor Mass, Volume, Inertia and Efficiency

While calculating the mass and the volume of the motor, the parts in which the electromechanical energy conversion takes place are taken into consideration. That is, all housing, bearing, winding and other terms are ignored for the ease of calculations. In such a case, the mass of motor includes the mass of the stator, the mass of the rotor and the mass of PM. Mass of the rotor is simply the mass of a cylinder with hollow and the mass of the PM can be handled by multiplying the area with the axial length, so calculation of these masses is quite easy. On the other hand, calculation of the mass of the stator is relatively difficult due to the existence of slot geometry and teeth. Mass of the rotor is expressed as in Equation 4.51.

$$M_{rotor} = \pi[(D_o/2)^2 - ((D_o - 2h_{sbc})/2)^2]Ld_{core} \quad (4.51)$$

where D_o is the outer diameter, h_{sbc} is the stator back core depth, which also determines the thickness of the rotor shell, L is the axial length and d_{core} is the density of core material. In addition, mass of the PM can be calculated as shown in Equation 4.52 .

$$M_{magnet} = \frac{\alpha}{2} (D_i + 2g + \frac{l_m}{2}) \frac{l_m}{2} p L d_{magnet} \quad (4.52)$$

where α is the arc angle of the magnet and d_{magnet} is the density of the magnet material. All other parameters are previously calculated and known quantities. In order to calculate the mass of the stator, it is plausible to divide this mass into sections. That is, the stator is composed of two sections, one is a hollow cylinder and the other is the group of teeth, number of which is equal to the number of slots. In this case, calculation of the the mass of the stator is shown between Equations 4.53 and 4.56.

$$M_{hollow} = \pi (D_{shaft} + h_{sbc}) h_{sbc} L d_{core} \quad (4.53)$$

$$M_{teeth} = S A_{tooth} L d_{core} \quad (4.54)$$

$$= S h_s w_s L d_{core} \quad (4.55)$$

$$M_{stator} = M_{hollow} + M_{teeth} \quad (4.56)$$

Calculation of the volume of the motor is quite easy. In this case, only outer diameter value D_o and axial length L values are needed. Final expression is shown in Equation 4.57.

$$V_{motor} = \pi (R_o)^2 L \quad (4.57)$$

Additionally, inertia of the motor can be calculated as the inertia of the rotating part, which is the rotor. Since the magnets are thinner as compared to the rotor, the effect of magnet inertia is neglected. Calculation of the rotor inertia is simply calculation of a cylindrical shell part, which can be calculated as shown in Equation

$$J_{motor} = \frac{1}{2} M_{rotor} (R_o^2 + (R_o - h_{sbc})^2) \quad (4.58)$$

Finally, the efficiency of the motor, denoted as η can be calculated as in Equation

$$\eta = \frac{P_{out}}{P_{in}} = \frac{P_{out}}{P_{out} + P_{total-loss}} = \frac{P_{out}}{P_{out} + P_{core} + P_{copper}} \quad (4.59)$$

4.3 Design Procedure of RF Motors under Squarewave Excitation

As mentioned earlier, the design process of RF motors are divided into two major sub-processes according to the excitation type and the sinusoidal case was covered. Related expressions and other calculations are presented by considering the variations in pole number, which can be thought as the minor processes for the design process. In this section, the relations for squarewave excitation is presented. It must be noted that the magnetic circuit derived for RF motor does not change for the excitation type, the related section will not be covered again.

4.3.1 Determination of Motor Dimensions for Squarewave Excitation

The starting point of the design process in context of squarewave excitation is almost similar to that of sinusoidal case. The torque expression as an initial point differs from the one used in sinusoidal excitation. The torque τ_p produced by an RF motor, if excited with a squarewave, is expressed in Equation 4.60.

$$\tau_p = \frac{\pi}{\sqrt{6}} B_g q D_i^2 L \quad (4.60)$$

In Equation 4.60, B_g is the flat top value of the flux density in the air gap, q is the electrical loading, D_i is the inner diameter and L is the axial length, all of which are the same parameters for that of the sinusoidal excitation.

As stated previously, B_g is a measure of saturation of the magnetic circuit (and therefore stated as magnetic loading in various sources) and depends on the material used for the core. This parameter is also related to core loss. q , on the other hand, is related to the copper loss and therefore is limited by the type of cooling. Experience from [7] indicates that the current loading up to 6000 A-t/m can be handled by the motor while the motor is accelerating with current density of $J=7 \text{ A/mm}^2$ in the conductors. Once the motor reaches its steady-state speed, it is found that current density falls down to 3 A/mm^2 and the motor temperature remains within acceptable limits.

At this point, the problem is determining the main dimensions of the motor, so that the

motor is capable of producing a torque of 50 mNm while the motor is accelerating, satisfying the following requirements:

- Flat-top value of air gap magnetic flux density for squarewave case must be $B_g = 0.62T$, so that the average value must satisfy $B_{gav} = 0.43T$.
- J_{Cu} is $7 A/mm^2$ during acceleration and less than $3 A/mm^2$ at steady-state.
- Electrical loading q must be less than 6000 A-turn/m during starting and less than 3000 A-t/m at steady-state.
- Accelerating torque must be 50 mN-m.
- Steady-state torque (at 10000 rpm) must be 32 mN-m.
- The flux density in order parts of the core must be 1.4 T maximum.

The approach to the problem is the same as the one applied for sinusoidal case. First, the flat-top air gap magnetic flux density B_g will be set as 0.62 T and then, the current density of the copper will be fixed at its maximum value, which is $7 A/mm^2$. finally, main dimensions such as slot depth h_s , back core depth h_{sbc} , inner diameter D_i , axial length L and the outer diameter of the motor D_o will be determined. As performed previously, the shaft diameter D_{shaft} is taken as 5 mm. The equations used during the determination of the sizes for squarewave excitation is summarized in Table 4.3.1.

Table 4.1: Expressions for Basic Dimensions

Flux per pole	$\phi_{pole} = B_g A_{pole}$
Flux at back core	$\phi_{sbc} = \frac{\phi_{pole}}{2}$
Back-core depth	$h_{sbc} = \frac{D_i - 2h_s - D_{shaft}}{2} L$
Slot depth	$h_s = \frac{1}{2} [D_i (1 - \frac{B_g \pi}{B_{sbc p}}) - D_{shaft}]$
Total Slot Area	$A_{slot} = \frac{\pi}{2} [(\frac{D_i}{2})^2 - (\frac{D_i}{2} - h_s)^2]$
Electrical loading	$q = \frac{\tau_p R_{DL}}{\frac{\pi}{\sqrt{6}} B_g D_i^3}$
Outer diameter	$D_o = D_i + 2g + 2l_m + 2h_{sbc}$

The torque equation of the electrical motor under sinusoidal excitation was previously stated as in the form shown in Equation 4.15. When it is written by substituting

R_{DL} and is solved for electrical loading, the equation takes the following form, as in Equation 4.29.

The electrical loading expressed as in Equation 4.29 and Equation 4.28 are both functions of D_i , where τ_p is a known design requirement. Therefore, for a given value of R_{DL} ; D_i can be solved from Equation 4.29. In addition, h_s can be calculated from Equation 4.25. It must be noted that D_o can be calculated from Equation 4.30.

4.3.2 Winding Design

When the motor is excited with squarewave, it must be noted that only two phases are active for each commutation period. When the voltage drop across the semiconductors are taken into account, the summation of the back emf's must be 18 V maximum. Hence, the maximum back emf for one phase is assumed to be 8 V.

The number of turns per phase can be expressed as shown in Equation 4.61 .

$$N_{ph} = \frac{E_{ph}}{B_g L D_i \omega_m} \quad (4.61)$$

4.3.3 Equivalent Circuit Parameters

The expressions derived in sinusoidal excitation case is also valid for squarewave excitation case. These expressions are summarized in Table 4.3.3.

Table 4.2: Summary of Equivalent Circuit Parameters

Air-gap Inductance	$L_g = \frac{P}{2} \frac{N^2}{2R_g + 2R_m}$
Slot Leakage Inductance	$L_{sl} = n_c (2N_c^2) \left[\frac{\mu_0 h_s L}{3w_2} + \frac{\mu_0 h_2 L}{w_1 + w_2} + \frac{\mu_0 h_1 L}{w_1} \right]$
End-Turn Inductance	$L_e = \frac{n_c \mu_0 T_{cp} N_c^2}{8} \ln \left(\frac{T_{cp} \sqrt{\pi}}{\sqrt{2} A_{slot}} \right)$
Phase Inductance	$L_{ph} = L_g + L_{sl} + L_e$
Phase Resistance	$R_{ph} = \frac{\sigma_{Cu} l_{Cu}}{A_{Cu}} = \frac{(MLC) N_{ph}}{A_{Cu}}$

4.3.4 Losses

In calculation of losses, the same procedure is applied as done for the sinusoidal excitation. Here, the flat-top value for the magnetic air-gap flux density must be used. While calculating the average flux density at tooth, fundamental component of the air gap magnetic flux density is taken into account. The resulting peak flux density at stator is compared with the maximum peak flux density value of the core and the whether it is suitable or not is investigated. While calculating copper losses, DC link current must be used due to the fact that two phases are excited in squarewave excitation. The required equations are stated in Equations from 4.62 to 4.65.

$$I_{in-rms} = I_{rms} + \frac{P_{core}}{3V_{DC}} \sqrt{\frac{2}{3}} \quad (4.62)$$

$$V_{DC} = 2I_{rms}R_{ph} + E_{ph} \quad (4.63)$$

$$I_{DC} = \sqrt{\frac{3}{2}} I_{in-rms} \quad (4.64)$$

$$P_{co} = 2I_{DC}^2 R_{ph} \quad (4.65)$$

4.3.5 Motor Mass, Volume, Inertia and Efficiency

Motor volume, mass and inertia values are calculated in the way same as used in sinusoidal case. The equations are summarized in Table 4.3.5.

Table 4.3: Summary of Motor Mass, Volume, Inertia and Efficiency Equations

Rotor Mass	$M_{rotor} = \pi[(D_o/2)^2 - ((D_o - 2h_{sbc})/2)^2]Ld_{core}$
Magnet Mass	$M_{magnet} = \frac{\alpha}{2}(D_i + 2g + \frac{l_m}{2})\frac{l_m}{2}pLd_{magnet}$
Hollow Mass	$M_{hollow} = \pi(D_{shaft} + h_{sbc})h_{sbc}Ld_{core}$
Teeth Mass	$M_{teeth} = Sh_s w_s Ld_{core}$
Stator Mass	$M_{stator} = M_{hollow} + M_{teeth}$
Volume	$V_{motor} = \pi R_o^2 L$
Inertia	$J_{motor} = 0.5M_{rotor}(R_o^2 + (R_o - h_{sbc})^2)$
Efficiency	$\eta = \frac{P_{out}}{P_{in}}$

4.4 Design Outputs

Design outputs are obtained by changing the ratio R_{DL} from 1 to 20 to get understand the behaviours of certain parameters like volume, mass, inertia and efficiency. All characteristics are compared depending on the excitation and the pole number, separately. The design outputs are tabulated in Appendix B (see Table B.1, Table B.2, Table B.3 and Table B.4). These comparisons are done in the following subsections.

4.4.1 Comparisons between Pole Numbers

In this section, designs are compared regarding the differences in pole numbers. Four main variations are taken into consideration, namely volume, mass, inertia and efficiency.

Volume comparison of the designs for different pole numbers with the same excitation is shown in Figure 4.7.

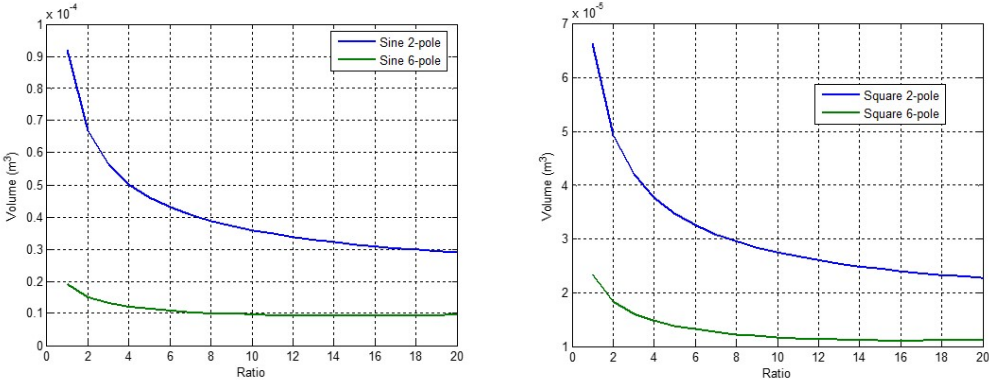


Figure 4.7: Volume Comparison of Designs Under Different Pole Numbers

As seen in Figure 4.7, both 6-pole designs have a volumetric advantage on the 2-pole designs, that is, if a smaller volume is desired, then a 6-pole design can be chosen. Mass comparison of the topologies under different pole numbers is shown in Figure 4.8.

As it can be seen in Figure 4.8, again the 6-pole designs are smaller in mass than the 2-pole equivalents. Thus, 6-pole designs can be preferred for a design with smaller mass specifications. Inertia of the designs with different pole numbers are shown in Figure 4.9.

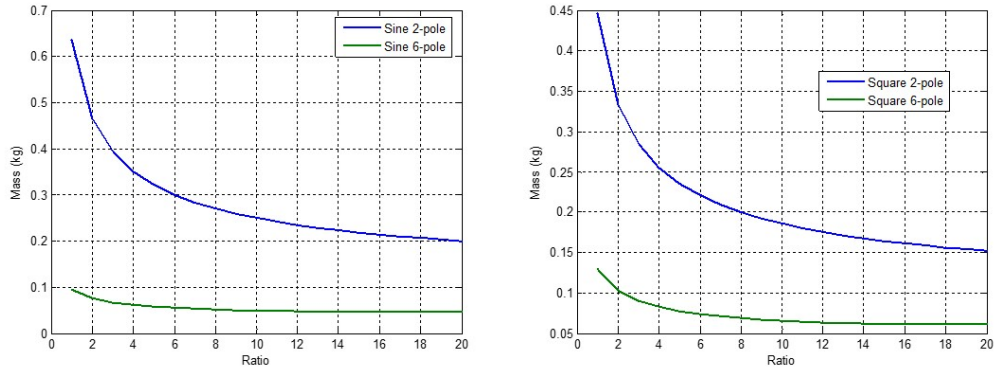


Figure 4.8: Mass Comparison of Designs Under Different Pole Numbers

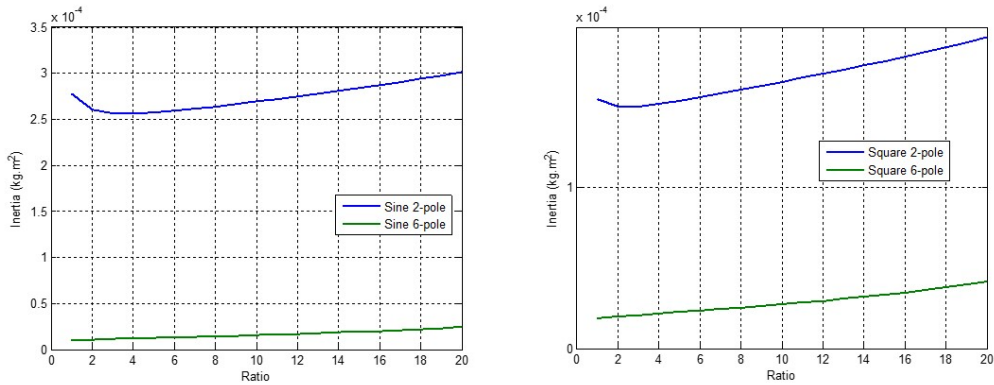


Figure 4.9: Inertia Comparison of Designs Under Different Pole Numbers

According to Figure 4.9, 2-pole designs have larger inertia as compared to the 6-pole equivalents. So, if it is desired to have a larger inertia contribution to the overall wheel system, 2-pole designs must be included and integrated to a CMG system. As a final comparison criteria for pole numbers, the difference of efficiency in different pole numbers are shown in Figure 4.10.

According to Figure 4.10, efficiency of 6-pole designs increases up to 94% while the efficiency of 2-pole designs increases to 90%. Hence, 6-pole designs have an efficiency advantage over the 2-pole designs.

4.4.2 Comparisons between Excitations

In this section, designs are compared regarding the differences in excitations. Again, four main variations are taken into consideration, namely volume, mass, inertia and efficiency.

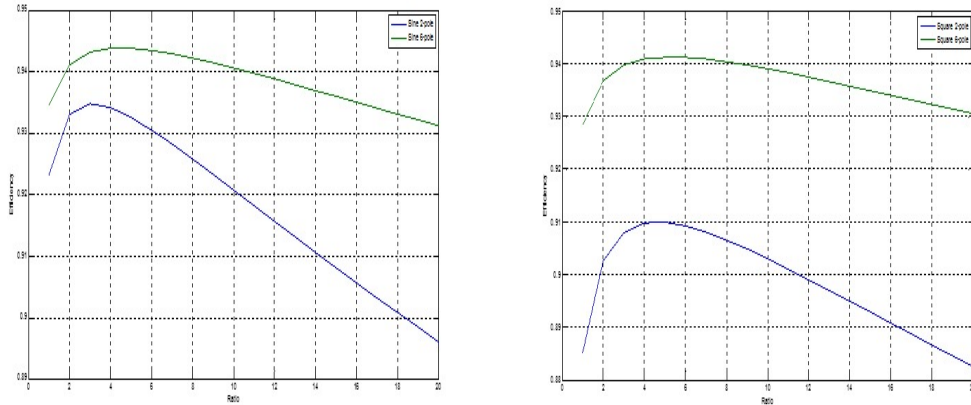


Figure 4.10: Efficiency Comparison of Designs Under Different Pole Numbers

Comparison of volume under different excitations with the same pole number is shown in Figure 4.11.

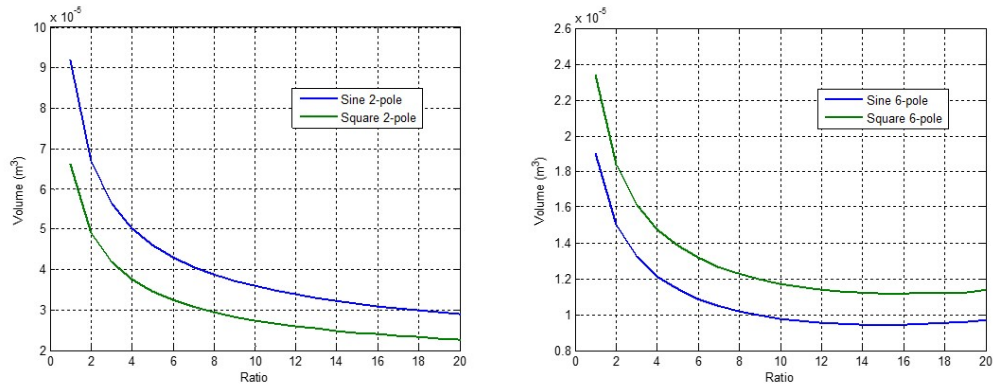


Figure 4.11: Volume Comparison of Designs Under Different Excitation

According to Figure 4.11, squarewave 2-pole design is more likely to be small in volume when compared to the sinusoidal 2-pole counterpart where the sinusoidal 6-pole design is smaller in volume than the squarewave 6-pole counterpart. Additionally, the mass comparison of the designs under different excitation is shown in Figure 4.12.

Figure 4.12 shows again that squarewave 2-pole design is smaller in mass than the sinusoidal 2-pole counterpart. On the other hand, sinusoidal 6-pole design set is smaller in mass than the squarewave 6-pole design set. Inertia values are compared as shown in Figure 4.13.

Figure 4.13 shows that sinusoidal design set has more inertia than the squarewave design set if it is designed in 2-pole. However, squarewave design set has more inertia than the sinusoidal counterpart if it is intended to make a design under 6-pole. The last

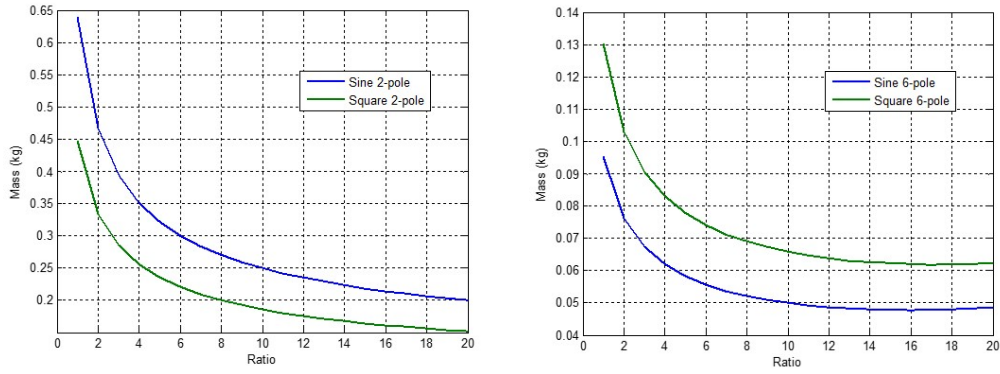


Figure 4.12: Mass Comparison of Designs Under Different Excitation

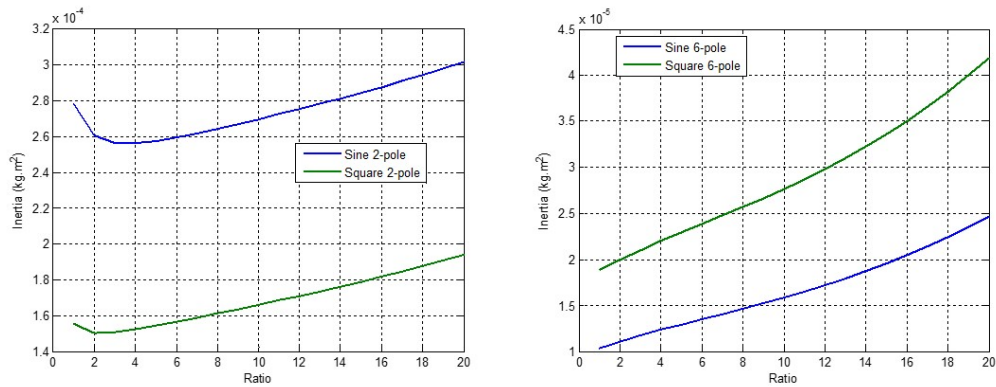


Figure 4.13: Inertia Comparison of Designs Under Different Excitation

comparison parameter, which is efficiency, is shown in Figure 4.14.

Figure 4.14 puts forward the fact that designs in sinusoidal excitation are more efficient than the squarewave designs in 2-pole, and the designs in squarewave excitation are more efficient than the sinusoidal ones in 6-pole. As a whole, a proper design must be selected regarding the physical and functional requirements. Design outputs for each topology are tabulated in Appendix B.

In the following chapter, performance results for chosen designs are going to be investigated. Simulation results of the topologies of interest under a Finite Element Analysis environment are going to be shown in Chapter 6.

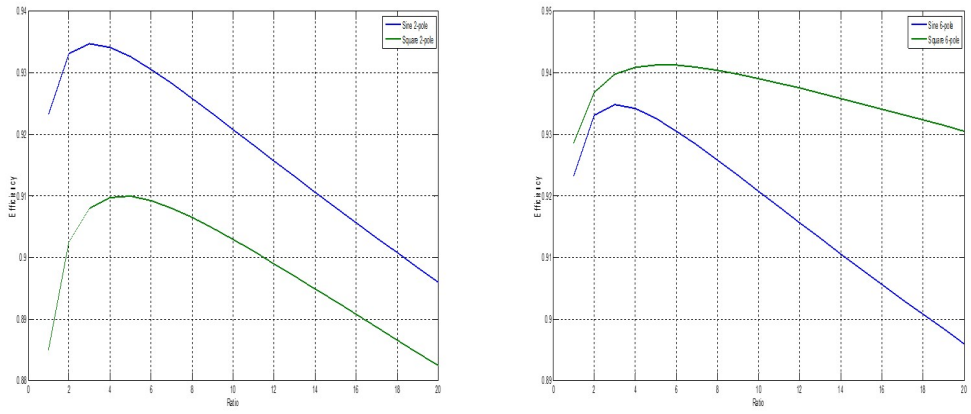


Figure 4.14: Efficiency Comparison of Designs Under Different Excitation

CHAPTER 5

ANALYTICAL RESULTS

This chapter includes the analytical results of the design procedure stated in Chapter 4. In order to determine the design outputs, MATLAB environment is used. In this manner, script codes including sizing and performance equations are prepared for each excitation and topology in separate m-files, and basic sizes, equivalent circuit parameters and winding details, as well as some performance criteria such as losses, efficiency, required current and back emf are calculated, as defined in Chapter 4. At the end of the process, separate tables are prepared for each design by changing D_i/L ratio from 0.7 to 20 with irregular step sizes, and for a chosen ratio, related graphs are presented. The point to be noted here is that the slot number in each proposed design is taken to be 18, and full-pitched concentrated windings are assumed to be used. Moreover, a coil extension is taken into account which has a value of 7 mm. Parameter descriptions are given in Appendix A, and the dimensions related to slots and teeth are defined based on Figure 5.1. Analytical results are presented in its related section or subsection, with the motor torque profile shown in Figure 3.4.

5.1 Analytical Results

Analytical results are obtained by setting the electrical loading value as 6000 A.t/m, motor torque as 50 mN-m while accelerating and 32 mN-m at rated speed, and phase voltage as 16 Volts, as defined in Chapter 4. Furthermore, it is desired to have an average air gap magnetic flux density value of 0.43 T. While conducting the design procedure, it is guaranteed that the average air gap magnetic flux density value is

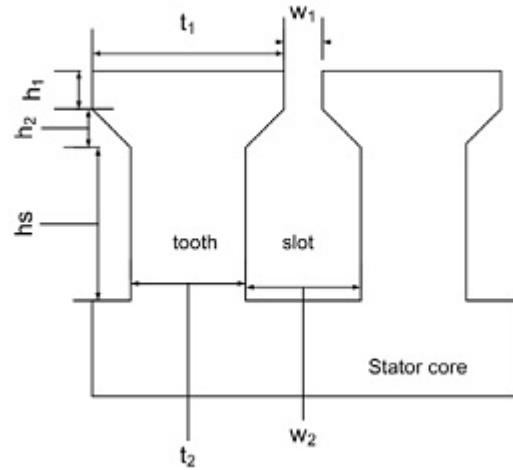


Figure 5.1: Tooth - Slot Dimensions

set to be 0.43 T. Hence, all design sets will have the desired magnetic loading value. Hence, design outputs are obtained with varying ratio R_{DL} and the design at which the ratio value satisfies the required electrical loading specification is concluded to be the final design. The variation of electrical loading with increasing R_{DL} ratio is shown in Figure 5.2.

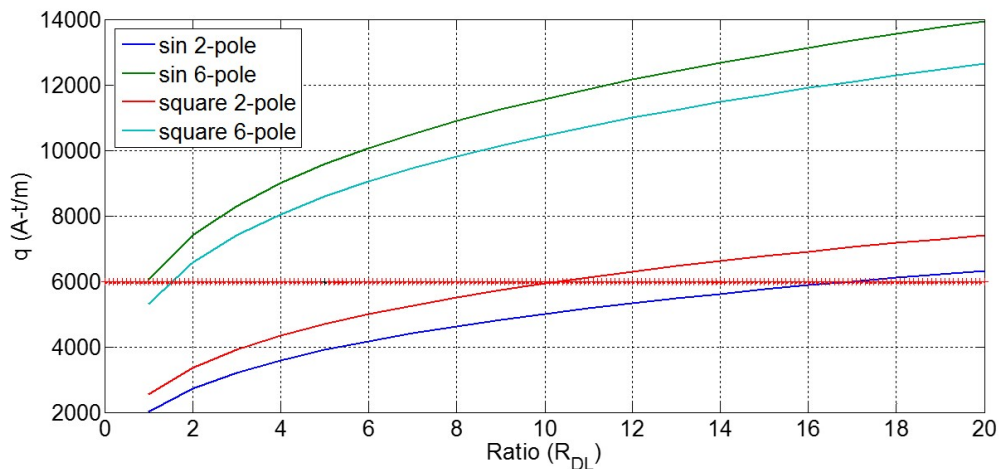


Figure 5.2: Electrical Loading Variation with Increasing Ratio

As it can be seen in Figure 5.2, the topologies satisfy the electrical loading value at different ratio R_{DL} values. The designs which have the required electrical loading value are tabulated in Appendix C (see Table C.1).

Following sections explain each topology with its corresponding performance characteristics such as electrical loading, RMS current, efficiency, power loss and voltage with varying rotor speed.

5.1.1 Analytical Results of Sinusoidal Designs

5.1.1.1 Sinusoidal 2-pole Design

The design results obtained for sinusoidal 2-pole design are summarized in Appendix C, in Table C.1, which presents the results as basic dimensions, inertia, mass and volume.

As seen in Figure 5.2, when ratio R_{DL} is 17, the electrical loading value is obtained about 6000 A-t/m. So, analytical results are obtained according to $R_{DL} = 17$ value, and graphical results are obtained accordingly. The analytical results related to electrical loading, rms current, efficiency, losses and voltage are shown in Figure 5.3.

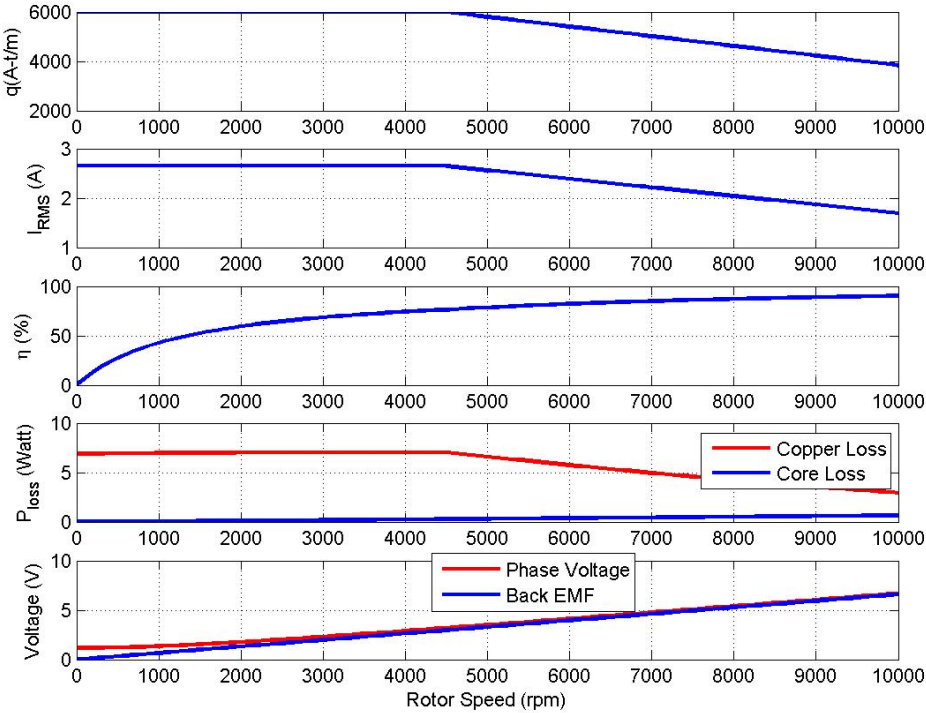


Figure 5.3: Analytical Results for Sinusoidal 2-pole Design

According to Figure 5.3, motor accelerates with an electrical loading value of 6000 A-t/m, and in steady-state this value becomes approximately 4000 A-t/m. Moreover, in acceleration period, the rms current is found to be about 2.7 A, but in steady-state, this value decreases to a value of 1.8 A. The efficiency at 10000 rpm is calculated to be 90%. In addition, it is seen that at all speeds, copper losses inside the motor dominates

the core losses inside the core material. In acceleration, copper losses reach to a value of 7 Watts, but in steady-state it decreases below 3 Watts. Core losses do not exceed a value of 1 Watt. Back emf value is calculated as 6.5 Volts in rms form.

5.1.1.2 Sinusoidal 6-pole Design

The analytical results obtained for sinusoidal 6-pole topology is shown in Appendix C (see Table C.1).

As seen in Figure 5.2, when ratio R_{DL} is 0.95, the electrical loading value is obtained about 6000 A-t/m, so this ratio is set to be the final design choice for squarewave excitation under 2-pole. Analytical results are obtained according to this ratio value, and graphical results are obtained accordingly. The analytical results related to electrical loading, rms current, efficiency, losses and voltage are shown in Figure 5.4.

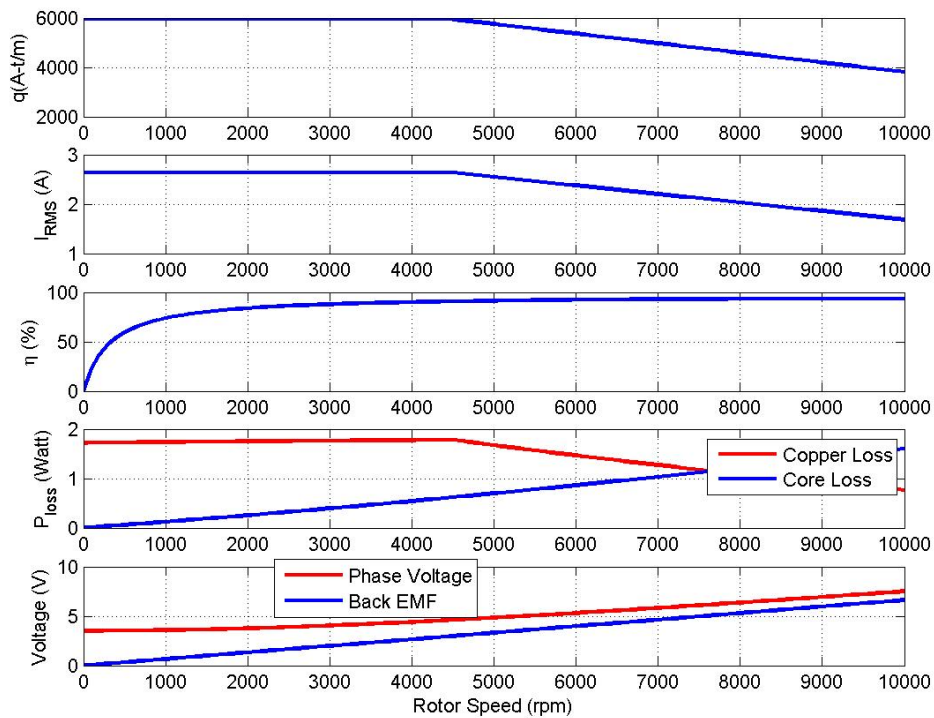


Figure 5.4: Analytical Results for Sinusoidal 6-pole Design

According to Figure 5.4, motor accelerates with an electrical loading value of 6000 A-t/m, and in steady-state this value becomes approximately 4000 A-t/m. Moreover, in acceleration period, the rms current is found to be about 2.7 A, but in steady-state,

this value decreases to a value of 1.65 A. The efficiency at 10000 rpm is calculated to be about 93%. In addition, core losses in 6-pole become more effective than that in 2-pole. In acceleration, copper losses reach to a value of 1.8 Watts, but in steady-state it decreases below 0.8 Watts. Core losses, on the other hand, reach to a value of 1.6 Watts. Back emf value is calculated as 6.5 Volts in rms form.

5.1.2 Sizes and Performance Evaluation of Squarewave Designs

5.1.2.1 Squarewave 2-pole Design

Table C.1 in Appendix C presents the results obtained for squarewave 2-pole topology such as basic dimensions, mass, volume and inertia.

As seen in Figure 5.2, when ratio R_{DL} is made 10, the electrical loading value is just below 6000 A-t/m. So, analytical results are presented according to $R_{DL} = 10$ value, and graphical results are obtained accordingly. The analytical results related to electrical loading, rms current, efficiency, losses and voltage are shown in Figure 5.5.

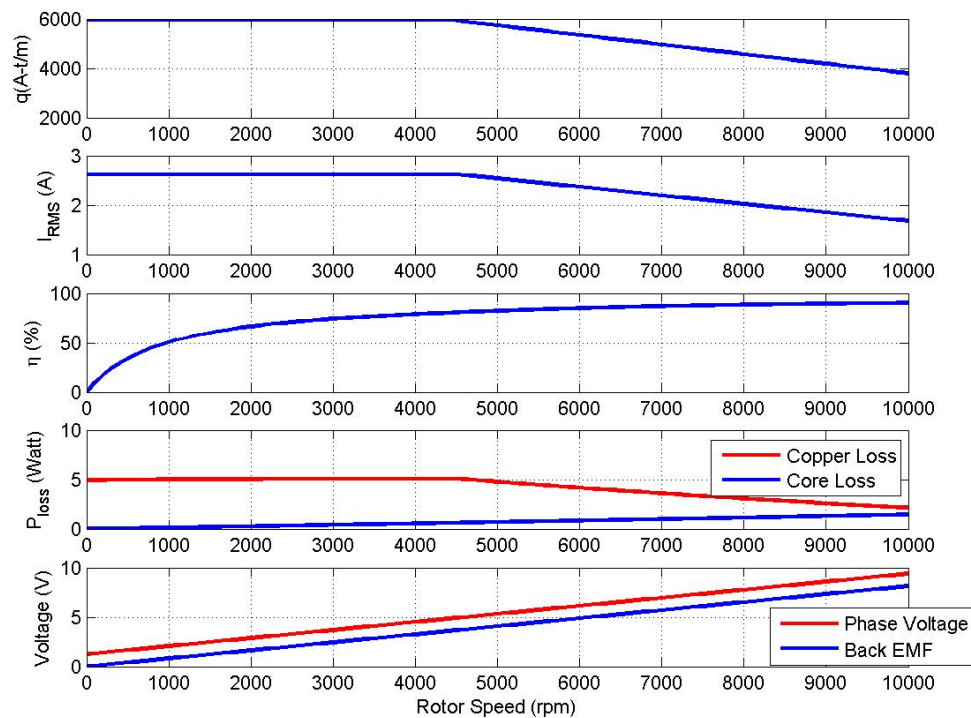


Figure 5.5: Analytical Results for Squarewave 2-pole Design

According to Figure 5.5, motor accelerates with an electrical loading value of 6000 A-t/m, and in steady-state this value becomes approximately 4000 A-t/m. Moreover, in acceleration period, the rms current is found to be about 2.65 A, but in steady-state, this value decreases to a value of 1.7 A. The efficiency at 10000 rpm is calculated to be approximately 90%. In addition, it is seen that at all speeds, copper losses inside the motor dominates the core losses inside the core material. In acceleration, copper losses reach to a value of 5 Watts, but in steady-state it decreases above 2 Watts. Core losses reach to a value of 1.5 Watts. Back emf voltage is calculated to be around 8 Volts per phase, which is as expected.

5.1.2.2 Squarewave 6-pole Design

The analytical results obtained for squarewave 6-pole topology is shown in Appendix C (see Table C.1).

As seen in Figure 5.2, when ratio R_{DL} is made 1.5, the electrical loading value is obtained about 6000 A-t/m. The analytical results related to electrical loading, rms current, efficiency, losses and voltage are shown in Figure 5.6.

According to Figure 5.6, motor accelerates with an electrical loading value of 6000 A-t/m, and in steady-state this value becomes approximately 4000 A-t/m. Moreover, in acceleration period, the rms current is found to be about 2.65 A, but in steady-state, this value decreases to a value of 1.7 A. The efficiency at 10000 rpm is calculated to be about 93%. In addition, core losses in 6-pole become more effective than that in 2-pole. In acceleration, copper losses reach to a value of 1.7 Watts, but in steady-state it decreases below 0.8 Watts. Core losses, on the other hand, reach to a value of 1.65 Watts. Back emf voltage is calculated to be around 8 Volts per phase, which is as expected.

5.2 Overall Performance Comparison

Overall performance parameters of the designs are summarized in Table 5.1. Specifications of the reference motor (MAXON 118892, as mentioned in Chapter 3) is also

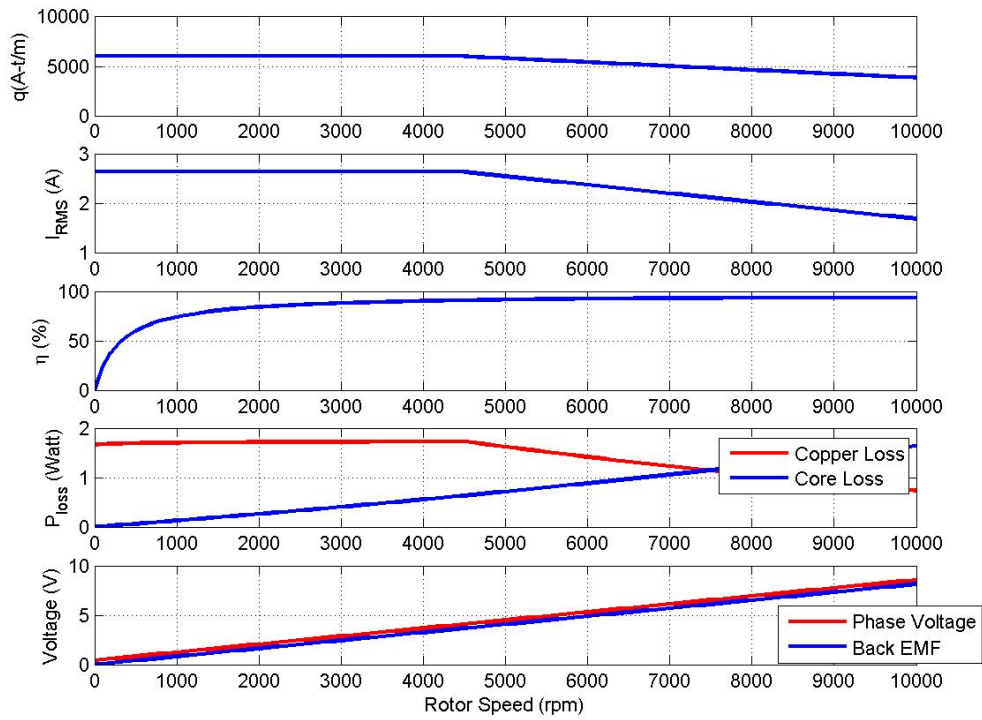


Figure 5.6: Analytical Results for Squarewave 6-pole Design

included in order to fully compare the designs.

According to Table 5.1, the phase resistance of 2-pole designs are higher than that of 6-pole designs, and the phase inductance of the designs are calculated to be smaller than the 6-pole counterparts. Losses in 2-pole designs are greater than the 6-pole designs, and efficiency of 6-pole topologies are larger than the 2-pole equivalents.

In the following chapter, simulation results obtained from Finite-Element Analysis are going to be presented and the obtained results are going to be compared with the ones presented here.

Table 5.1: Overall Performance Parameters at Steady-State

Parameter	Sine 2-pole	Sine 6-pole	Square 2- pole	Square 6- pole	MAXON 118892
$R_{ph} (m\Omega)$	327,45	82,73	238,38	80,30	481
$L_{ph} (\mu H)$	288,58	424,88	268,92	386,79	75
$I_{rms} (A)$	1,8	1,69	1,68	1,68	4,15
$e_{back-peak} (V)$	9,24	9,20	8	8	9
$q (A.t/m)$	4070	3795	3805	3847	-
$B_{gav} (T)$	0,43	0,43	0,43	0,43	-
$B_{sbc-peak} (T)$	1,45	1,46	1,43	1,44	-
$P_{Loss} (W)$	3,54	2,37	3,60	2,37	-
$\eta (\%)$	90,31	93,31	90,16	93,30	81
$\tau_{steady-state} (mN - m)$	32	32	32	32	45,2
$n_s (rpm)$	10000	10000	10000	10000	12700

CHAPTER 6

SIMULATION RESULTS

This chapter aims at verifying the analytical results obtained in Chapter 5. For this purpose, Finite Element Analysis is made on the designs made in Chapter 4 and the performance of the designs which are analytically made are compared with the results found from the Finite-Element solution. Here, proper designs are chosen such that the electrical loading value during the acceleration satisfies the design requirement, which is 6000 A-t/m.

6.1 Simulation Results

As stated previously, ANSYS MAXWELL was used as the simulation tool for the motors, as a Finite-Element Method solution tool. While solving the motors, the meshes are assigned automatically by the program, so no additional assignment on the meshes is made by the user in manual manner. In addition, core material and permanent magnet properties are assigned as presented in Chapter 3. That is, a library is constructed for both ferromagnetic material COGENT Power No. 12 by taking the core loss data shown in Table 3.5 and Figure 3.9 and permanent magnet VACOMAX 225 HR as shown in 3.6. Core loss parameters and related B-H curves are entered to the library, and stator and rotor materials are assigned accordingly, as well as the assignment of permanent magnet material. The copper resistivity is taken as $1,72.10^{-8}\Omega - m$. Finally, transient solutions are applied in all motors. Boundaries are assigned by the program automatically such that boundary conditions are defined just outside the motor contour. In these regions, vector potential is taken to be zero, so no

flux is leaking outside the motor. In solutions, motor speed is started at 10000 rpm and electrical oscillations are observed accordingly. Thus, the solutions are going to be presented for the state at which a steady-state characteristics is obtained. The data of the motors analyzed in Finite-Element Method can be found in Appendix C (see Table C.1).

6.1.1 Simulation Results of Sinusoidal Designs

While simulating the sinusoidally excited motors, first, motor is prepared in RMXprt Module of MAXWELL environment considering the sizes calculated analytically and transferred to the 2D design environment. In 2D design environment, motor is divided into symmetrical sections due to the symmetry in the magnetic circuit. In this manner, computational effort required for the solutions is reduced. The equivalent circuit of the solution is depicted in Figure 6.1. Before running the simulation, three main parameters must be entered to the depicted model, namely phase resistance, leakage inductance and the input phase voltage. MAXWELL does not have the capability of calculating the phase resistance and inductance terms related to leakage phenomena and end-turn geometry. The program only assigns physical regions for windings or coils and assigns certain materials for windings, stator, rotor etc. Hence, the equivalent circuit parameters must be entered in an external manner. Finally, input phase voltage, which is $16/\sqrt{3} = 9.24V_{peak}$ is entered as a sinusoidal expression with its corresponding frequency (166 Hz for 2-pole and 500 Hz for 6-pole) and phase(each waveform 120° apart from each other), and the model is run after setting these parameters.

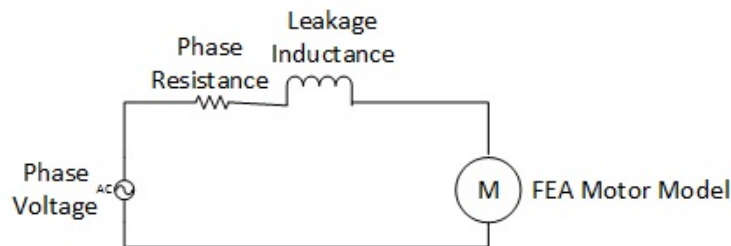


Figure 6.1: Simulation Model

In the following subsections, the results obtained after applying the procedure stated above are going to be presented.

6.1.1.1 Sinusoidal 2-pole Design

For validation of the sinusoidal 2-pole brushless DC motor, the model shown in Figure 6.2 is prepared. The main dimensions are tabulated in Appendix C (see Figure C.1), with the corresponding column and the description of the dimensions is given in Figure 5.1 with the descriptions stated as in Appendix A (see Table A.1).

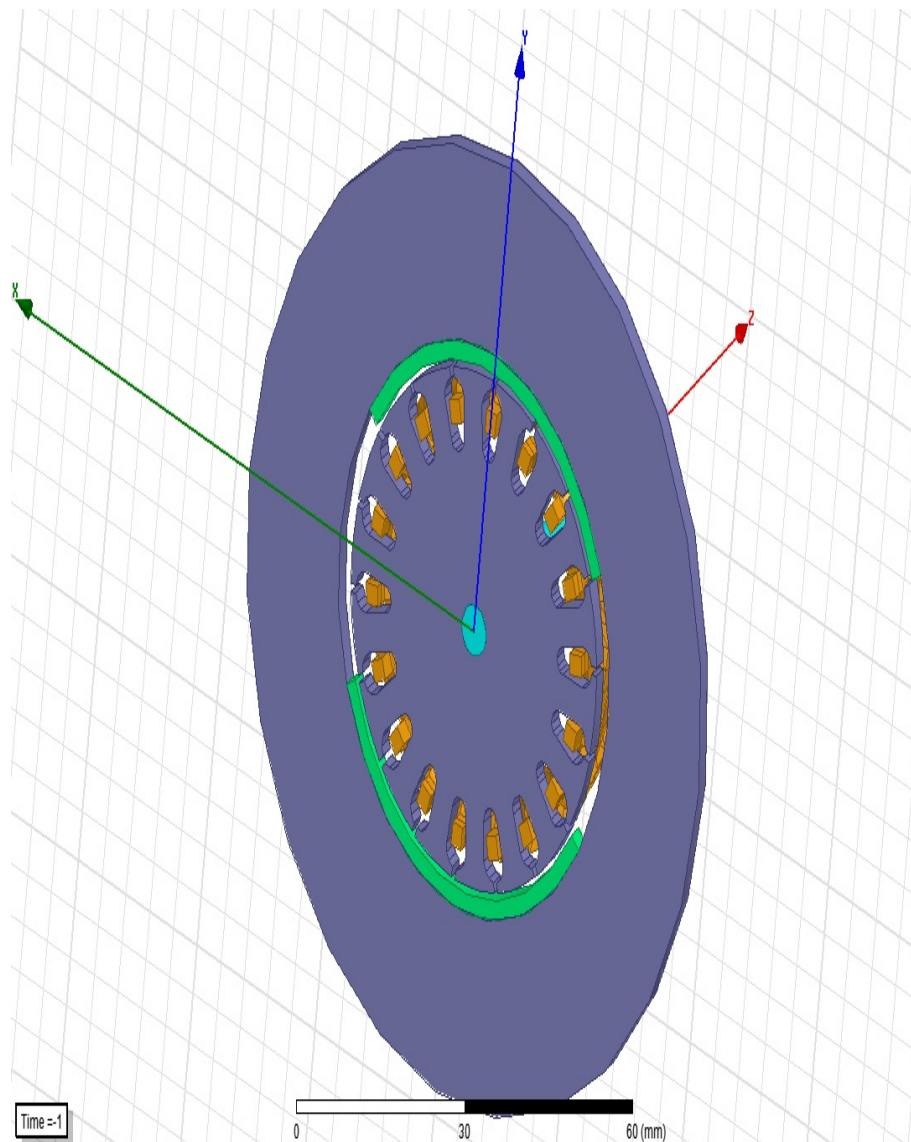


Figure 6.2: Motor Model Prepared in MAXWELL (sinusoidal 2-pole)

The results obtained in ANSYS MAXWELL environment for sinusoidal 2-pole design are shown in Figure 6.3, Figure 6.5 and Figure 6.6. Figure 6.5 shows the winding current and induced voltage while Figure 6.6 shows the motor torque, load torque and rotor speed, respectively.

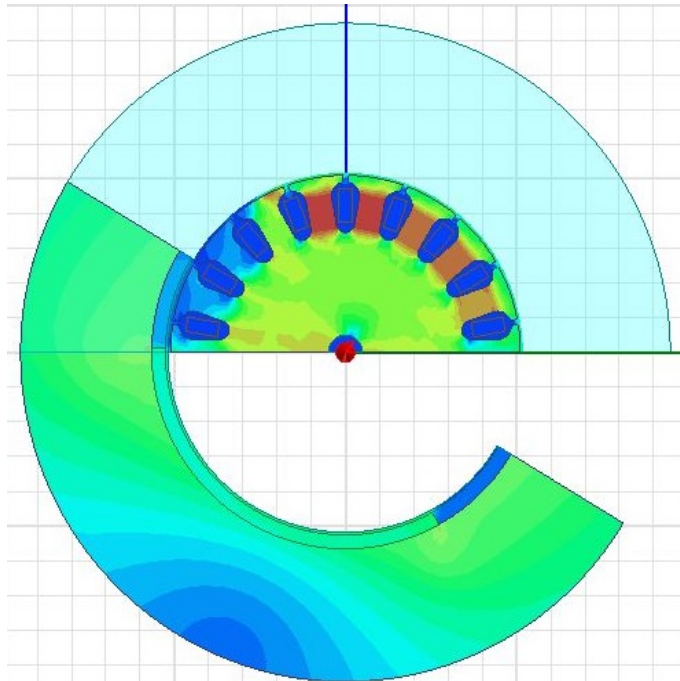


Figure 6.3: Magnetic Fields Obtained From MAXWELL for Sinusoidal 2-pole Topology

Air gap magnetic flux density and flux density along one tooth in the sinusoidal 2-pole design is shown in Figure 6.4.

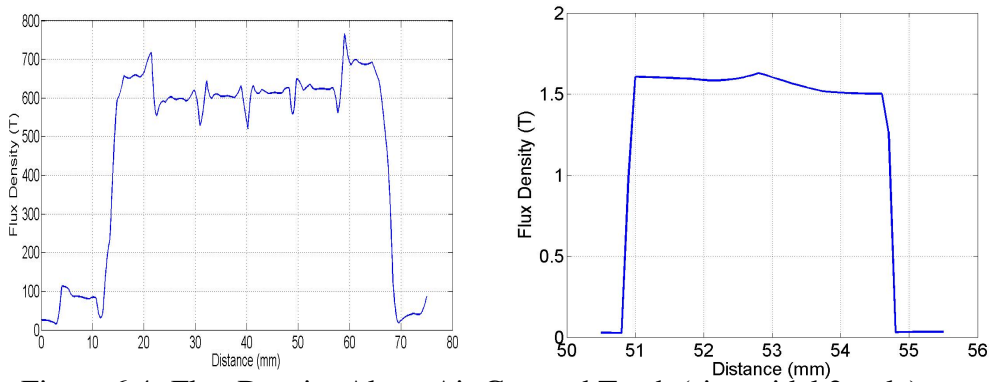


Figure 6.4: Flux Density Along Air Gap and Tooth (sinusoidal 2-pole)

As seen in Figure 6.3 and Figure 6.4, the tooth flux density rises up to a value of 1.55 T. In Figure 6.3, regions shown in red correspond to a magnetic flux density value of 1.5 T and Figure 6.4 verifies this finding. The flux density plots are obtained by defining contours along air gap and stator tooth, all of which are drawn in the middle of air gap and stator tooth, respectively. When this value is compared with the one calculated analytically as shown in Table 5.1, it is seen that the calculated and simulated results are close to each other.

Induced phase voltage and winding current behaviour of the motor is shown in Figure 6.5.

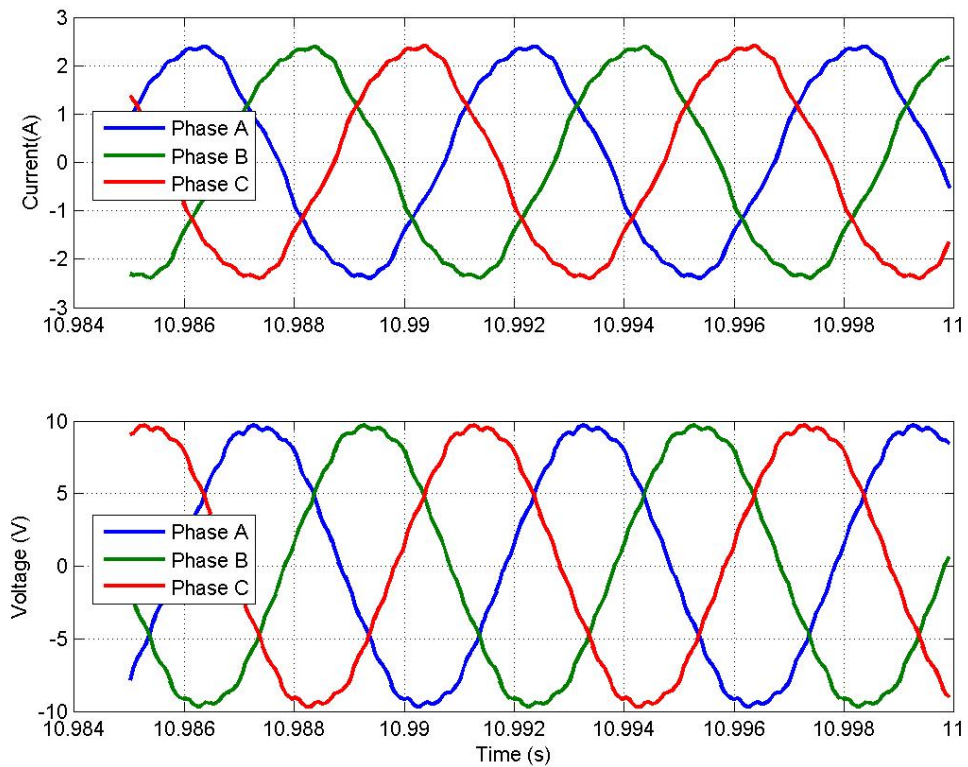


Figure 6.5: Winding Current and Induced Voltage Obtained From MAXWELL for Sinusoidal 2-pole Topology

According to Figure 6.5, the peak value of the winding current is calculated to be 2.4 A, the rms of which is 1.76 A, which is consistent with the analytical result tabulated in Table 5.1, which is 1,8 A. In addition, the peak phase voltage is measured below 10 Volts, which is found as expected. Although the value in Table 5.1 is shown as 6.5 Volts, it is in rms quantity. Hence, the peak value is calculated as 9,24 Volts, which is consistent with the simulation result.

Furthermore, torque and speed findings of the simulation is shown Figure 6.6.

It is observed in Figure 6.6 that the motor reaches a steady-state behaviour before 10 seconds. That is, the torque produced by the motor settles such that no significant decrease in ripple is observed. Hence, the graphs are drawn accordingly. As seen in Figure 6.6, the torque fluctuates around a steady-state value of 32.70 mN-m, but it

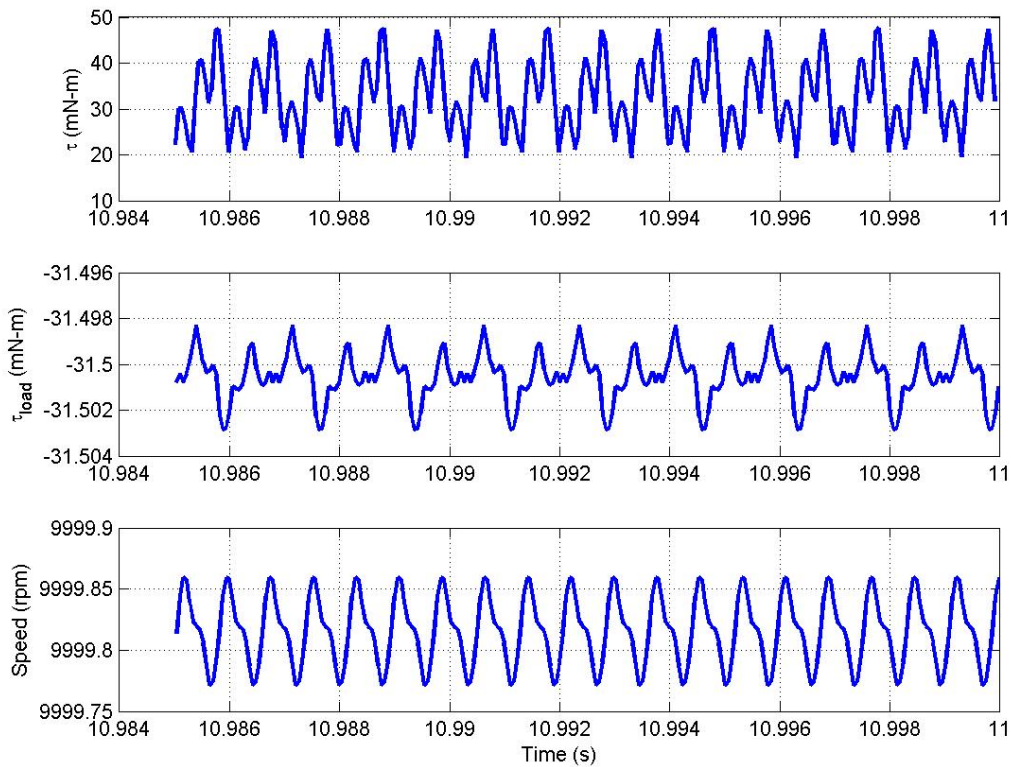


Figure 6.6: Torque and Speed Obtained From MAXWELL for Sinusoidal 2-pole Topology

has a torque ripple of about 25 mN-m. This is due to the fact the flux density seen at tooth exceeds the design parameter 1.4 T, which in turn saturates the core material. Simulation also shows that the load torque value approaches to a steady-state value of 31.5 mN-m, and, the speed of the motor has a steady state value of 10000 rpm.

Overall comparison between analytical results and simulation results of this topology is tabulated in Table 6.1.

6.1.1.2 Sinusoidal 6-pole Design

The outputs obtained in ANSYS MAXWELL environment for sinusoidal 6-pole design are shown in Figure 6.7, Figure 6.9 and Figure 6.10.

Figure 6.8 shows the variation of the air gap flux density and tooth flux density. The

Table 6.1: Comparison of Analytical and Simulation Results of Sinusoidal 2-Pole BLDC Motor at Steady-State

	Sinusoidal 2-pole	
	Analytical	Simulation
I_{rms} (A)	1,8	1,76
e_{back} (V)	9,24	9,20
R_{ph} (m Ω)	327,45	327,45
L_{leak} (μ H)	110,30	110,30
L_{ph} (μ H)	288,58	254,30
B_{gav} (T)	0,43	0,41
q (A.t/m)	4070,00	3980,00
$B_{stator-peak}$ (T)	1,45	1,55
$B_{rotor-peak}$ (T)	1,46	1,56
P_{loss} (W)	3,54	3,70
P_{out} (W)	33,00	34,24
τ_{motor} (mN.m)	32,00	32,70
η (%)	90,31	90,25

plots are obtained by defining a contour in the middle of the air gap and stator tooth.

As seen Figure 6.7, the tooth flux density, which is denoted by brown regions, rises up to a magnetic flux density value of 1.54 T, which is close to the calculated flux density value as tabulated in Table 5.1, as well as the tooth flux density plot shown in Figure 6.8.

Winding current and induced phase voltage findings are shown in Figure 6.9.

According to Figure 6.9, the peak phase voltage is measured around 9 Volts, and rms value is found as 7 Volts which is close to the analytical induced phase voltage value given in Table 5.1. Moreover, the peak value of the winding current is found to be approximately 2.4 A, and rms value of this current is calculated as 1.70 A, which is also close to the analytical results stated in Table 5.1.

Additionally, torque and speed findings of the simulation is shown Figure 6.10.

It is observed that the motor reaches a steady-state behaviour before 8 seconds. Hence,

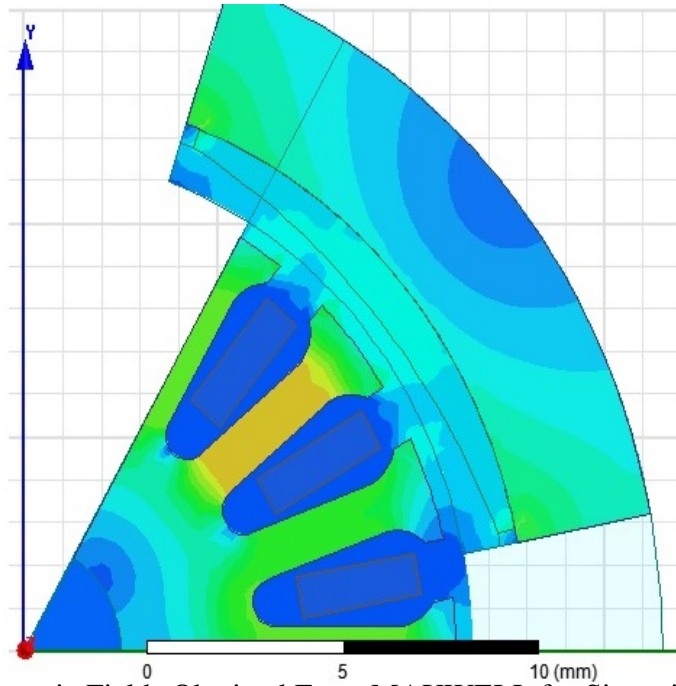


Figure 6.7: Magnetic Fields Obtained From MAXWELL for Sinusoidal 6-pole Topology

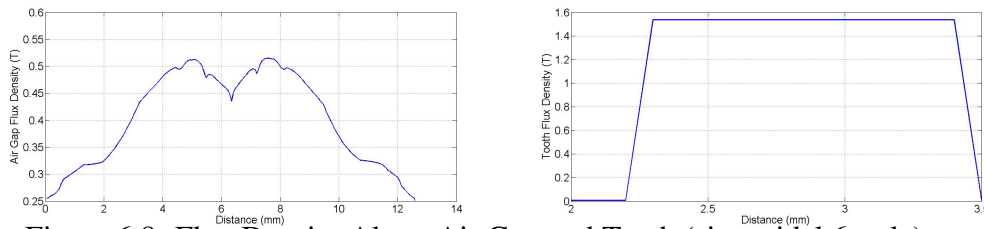


Figure 6.8: Flux Density Along Air Gap and Tooth (sinusoidal 6-pole)

the graphs are drawn accordingly. As seen Figure 6.10, the torque fluctuates around the steady-state design parameter 32.9 mN-m, but it has a torque ripple of about 15 mN-m. Again, this is due to the fact the flux density seen at tooth exceeds the design parameter 1.4 T, which in turn saturates the core material. Simulation shows that the load torque value approaches to a steady-state value of 31.53 mN-m, and, the speed of the motor oscillates around the rated speed value of 10000 rpm.

Overall comparison between analytical results and simulation results of this topology is tabulated in Table 6.2.

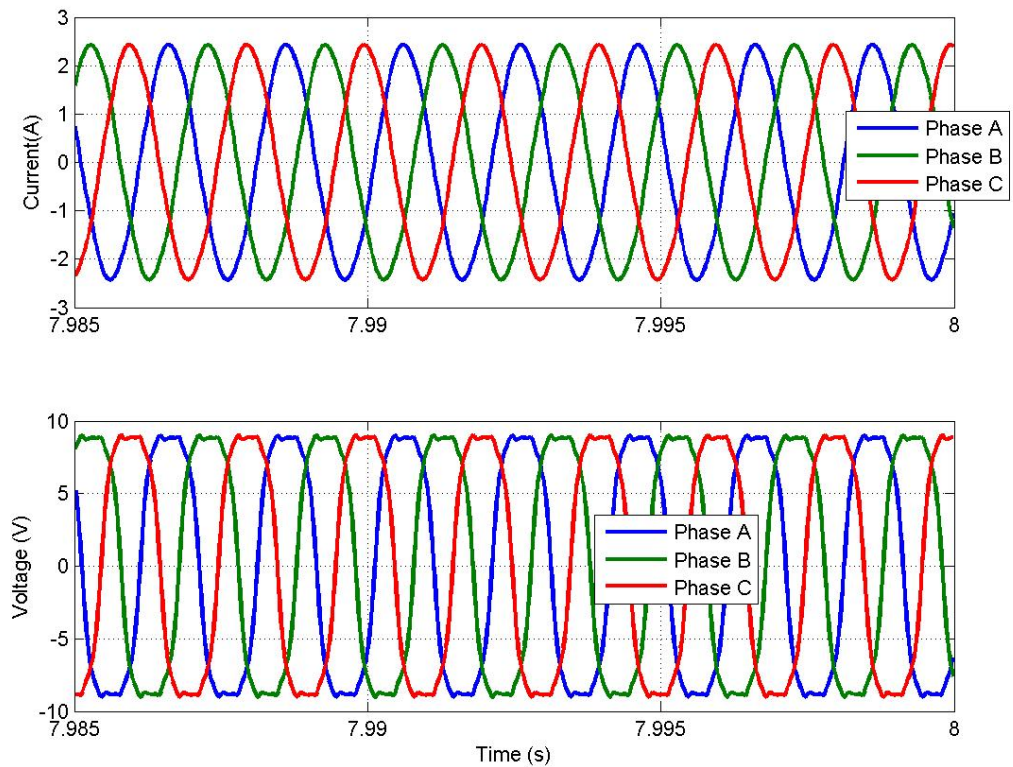


Figure 6.9: Winding Current and Induced Voltage Obtained From MAXWELL for Sinusoidal 6-pole Topology

6.1.2 Simulation Results of Squarewave Designs

While simulating the squarewave excited motors, the same procedure is applied as the one applied for sinusoidally excited. First, motor is prepared in RMxpert Module of MAXWELL environment, considering the sizes calculated analytically and transferred to the 2D Environment. In 2D environment, motor is divided into symmetric sections due to the symmetry in the magnetic circuit in order to reduce the computation time of the solution. Before running the simulation, phase resistance, leakage inductance and the input phase voltage (here, flat-top value of the phase voltage of 8 V is taken) are entered to the model and the model is run after setting these parameters as performed in sinusoidal design.

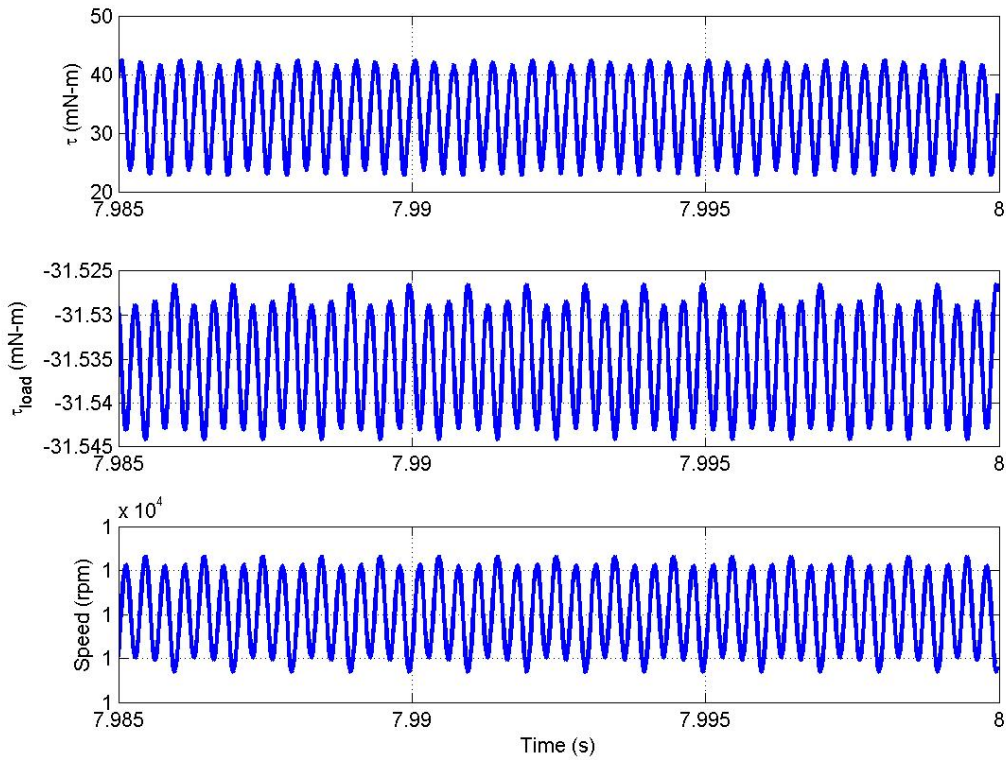


Figure 6.10: Torque and Speed Obtained From MAXWELL for Sinusoidal 6-pole Topology

6.1.2.1 Squarewave 2-pole Design

The outputs obtained in ANSYS MAXWELL environment for squarewave 2-pole design are shown in Figure 6.11, Figure 6.13 and Figure 6.14.

Figure 6.12 shows the variation of the air gap flux density and tooth flux density. The plots are obtained by defining a contour in the middle of the air gap and stator tooth.

As seen Figure 6.11, the tooth flux density, which is denoted by brown regions, rises up to a magnetic flux density value of 1.56 T, which is close to the calculated flux density value as tabulated in Table 5.1, as well as the tooth flux density plot shown in Figure 6.12.

Winding current and induced phase voltage findings are shown in Figure 6.13.

According to Figure 6.13, the peak phase back emf is measured to be 7 Volts, which is

Table 6.2: Comparison of Analytical and Simulation Results of Sinusoidal 6-Pole at Steady-State

	Sinusoidal 6-pole	
	Analytical	Simulation
I_{rms} (A)	1,69	1,70
e_{back} (V)	9,20	9,00
R_{ph} (m Ω)	82,70	82,70
L_{leak} (μ H)	242,58	242,58
L_{ph} (μ H)	424,88	312,11
B_{gav} (T)	0,43	0,41
q (A.t/m)	3805,00	3840,00
$B_{stator-peak}$ (T)	1,43	1,54
$B_{rotor-peak}$ (T)	1,43	1,55
P_{loss} (W)	2,37	2,32
P_{out} (W)	33,00	34,46
τ_{motor} (mN.m)	32,00	32,91
η (%)	93,31	93,69

close to the analytical induced phase voltage value given in Table 5.1. Moreover, the peak value of the winding current is found to be approximately 3 A, and rms value of this current is calculated as 2 A, which is also close to the analytical results stated in Table 5.1.

Additionally, torque and speed findings of the simulation is shown Figure 6.14.

It is observed that the motor reaches a steady-state behaviour before 25 seconds. Hence, the graphs are drawn accordingly. As seen Figure 6.14, the torque rises up to 32.4 mN-m, and no torque ripple as in sinusoidal 2-pole case is observed. The load torque value approaches to a steady-state value of less than 30,8 mN-m. The speed of the motor approaches to the steady state value of 9060 rpm.

Overall comparison between analytical results and simulation results are summarized in Table 6.3.

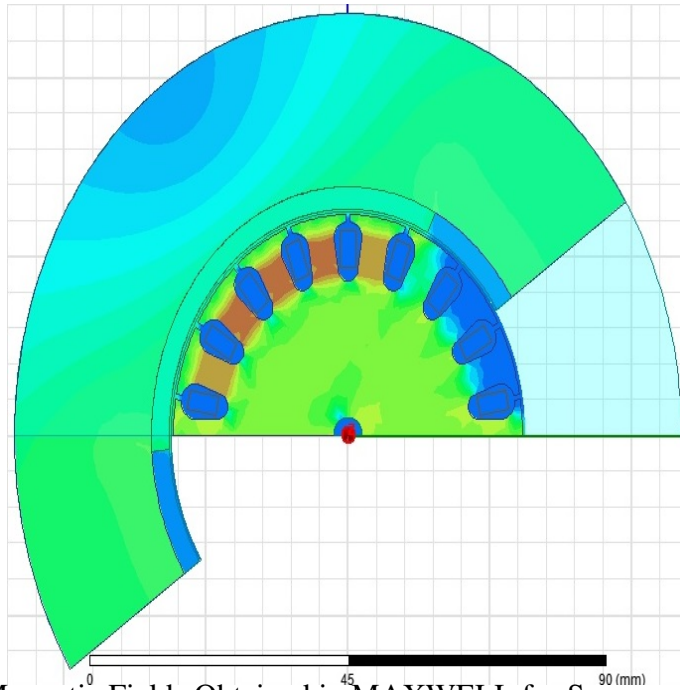


Figure 6.11: Magnetic Fields Obtained in MAXWELL for Squarewave 2-pole Topology

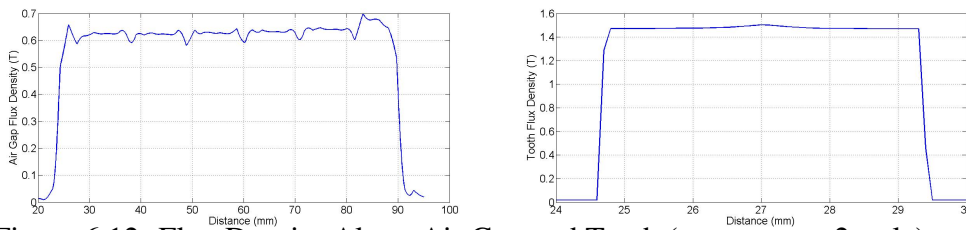


Figure 6.12: Flux Density Along Air Gap and Tooth (squarewave 2-pole)

6.1.2.2 Squarewave 6-pole Design

The outputs obtained in ANSYS MAXWELL environment for squarewave 6-pole design are shown in Figure 6.15, Figure 6.17 and Figure 6.18.

Figure 6.16 shows the variation of the air gap flux density and tooth flux density. Again, the plots are obtained by defining a contour in the middle of the air gap and stator tooth.

As seen Figure 6.15, the tooth flux density, which is denoted by orange regions, rises up to a magnetic flux density value of 1.5 T, which is close to the calculated flux density value as tabulated in Table 5.1, as well as the tooth flux density plot shown in Figure 6.16.

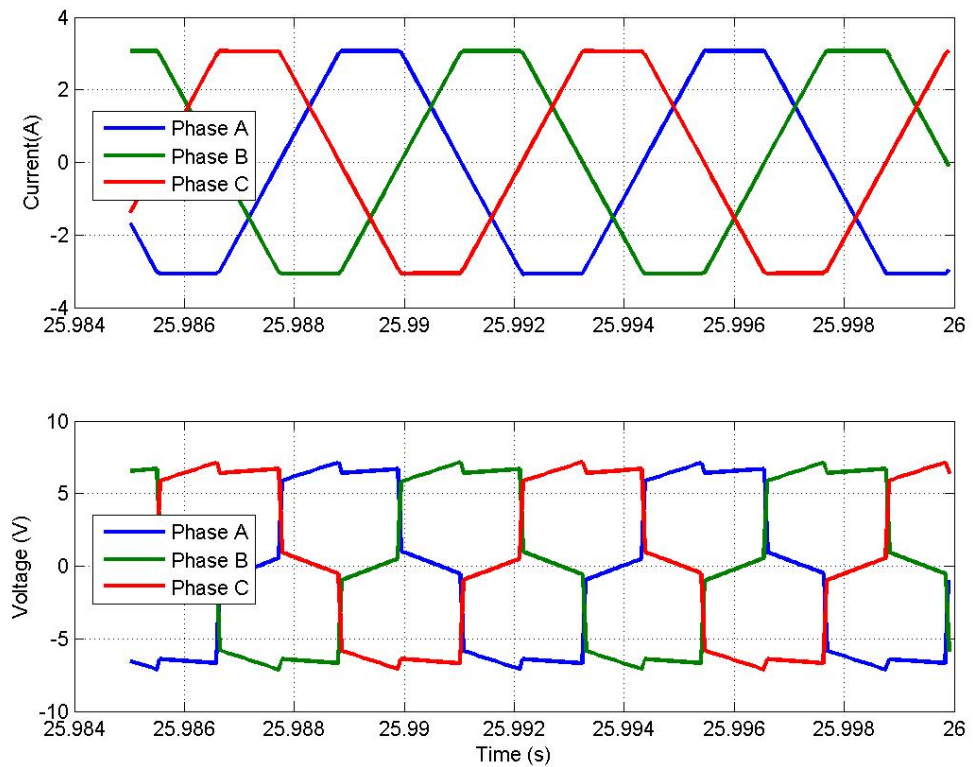


Figure 6.13: Winding Current and Induced Voltage Obtained From MAXWELL for Squarewave 2-pole Topology

Winding current and induced phase voltage findings are shown in Figure 6.17.

According to Figure 6.17, the peak phase back emf is measured to be 8 Volts, which is close to the analytical induced phase voltage value given in Table 5.1. Moreover, the peak value of the winding current is found to be approximately 3 A, and rms value of this current is calculated as 2 A, which is also close to the analytical results stated in Table 5.1.

Additionally, torque and speed findings of the simulation is shown Figure 6.18.

As seen in Figure 6.18, the average torque is calculated as 32.7 mN-m. The load torque value approaches to a steady-state value of less than 31.5 mN-m. The speed of the motor approaches to the steady state value of 10000 rpm.

Overall comparison between analytical results and simulation results are summarized in Table 6.4.

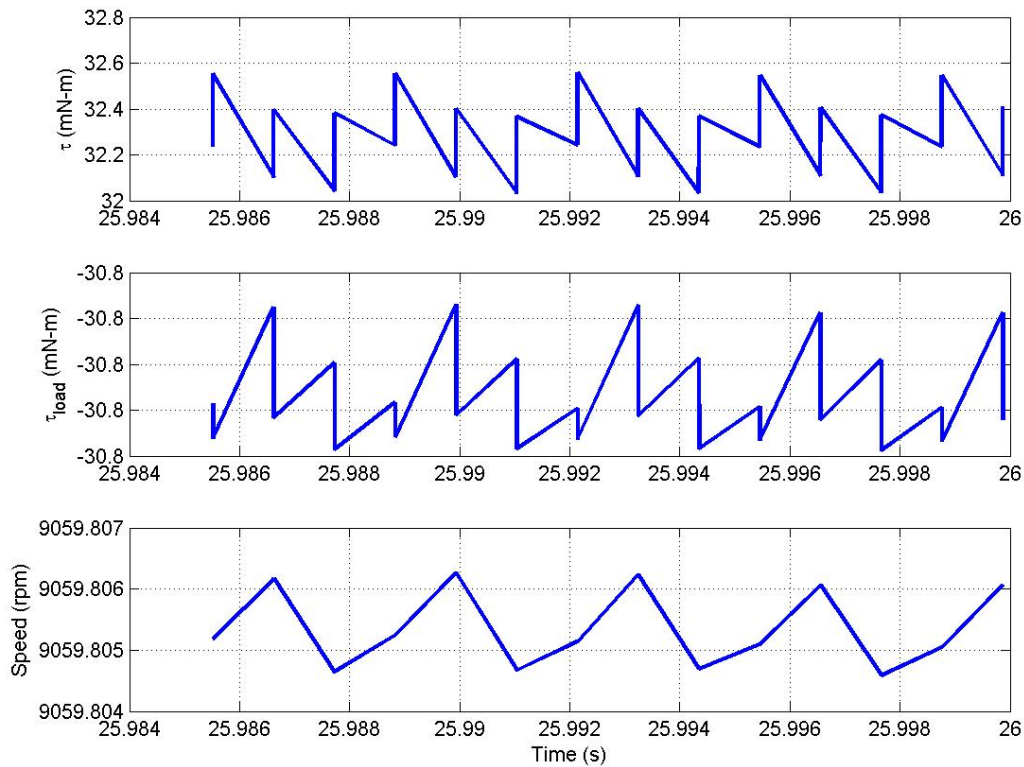


Figure 6.14: Torque and Speed Obtained From MAXWELL for Squarewave 2-pole Topology

6.2 Comparison of The Results with an Axial-Flux Equivalent

In this section, the design conducted in [7] is presented. In [7], both inside-rotor RF motors and AF motors are designed, and a 6-pole squarewave excited AF solution is concluded to be the best alternative among all in torque per unit mass, torque per unit volume and efficiency point of view. Main dimensions and properties of the proposed design is summarized in Appendix D (see Table D.1).

6.2.1 Simulation Results in MAXWELL

The AF design is prepared in MAXWELL environment in order to obtain the results. The simulation results of the 6-pole AF motor such as magnetic field, winding current, induced voltage, torque and speed are shown in Figure 6.19 and Figure 6.20, respec-

Table 6.3: Comparison of Analytical and Simulation Results of Squarewave 2-Pole at Steady-State

	Squarewave 2-pole	
	Analytical	Simulation
I_{rms} (A)	1,68	2,00
e_{back} (V)	8,00	7,00
R_{ph} (m Ω)	238,38	238,38
L_{leak} (μ H)	114,38	114,38
L_{ph} (μ H)	268,92	248,30
B_{gav} (T)	0,43	0,55
q (A.t/m)	3795,00	3837,00
$B_{stator-peak}$ (T)	1,46	1,56
$B_{rotor-peak}$ (T)	1,47	1,56
P_{loss} (W)	3,60	3,36
P_{out} (W)	33,00	34,45
τ_{motor} (mN.m)	32,00	32,91
η (%)	90,16	91,11

tively.

The magnetic flux density is maximum at the stator side, at the instant shown in Figure 6.19 and this value is read as 1.5 T, which is in an acceptable level.

As it can be seen in Figure 6.20, the steady-state torque value oscillates around the required design value of 32 mN-m, having a ripple value of 13 mN-m. What is more, the peak value of the line induced voltage is measured to be about 15 Volts. It shows a distorted characteristics; but this is mainly due to the armature reaction phenomena. In addition, the phase currents are 120 °apart from each other and in balanced form. The measured rms value of phase current is about 2 A, which is as expected as designed in [7]. Finally, rotor speed is calculated to be 10000 rpm, at all time instances.

6.2.2 Overall Finite Element Analysis Results

In Table 6.5, all the results obtained in MAXWELL are summarized as a table.

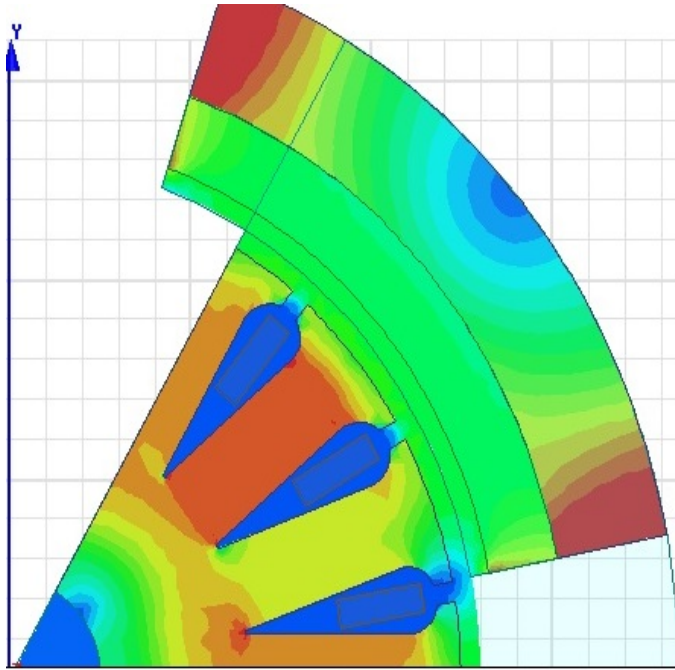


Figure 6.15: Magnetic Fields Obtained in MAXWELL for Squarewave 6-pole Topology

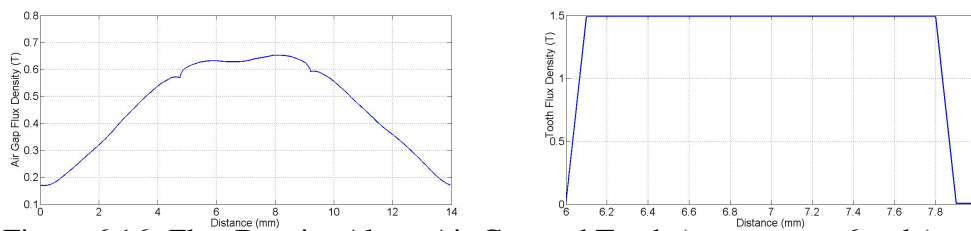


Figure 6.16: Flux Density Along Air Gap and Tooth (squarewave 6-pole)

As shown in Table 6.5, all the performance parameters of the proposed designs are compatible with the ones calculated analytically.

In the next chapter, the overall thesis study is going to be summarized, and overall results such as volume, torque per unit volume, mass, torque per unit mass, inertia, inertia contribution and efficiency results are going to be compared briefly. Finally, a brief future work is going to be stated.

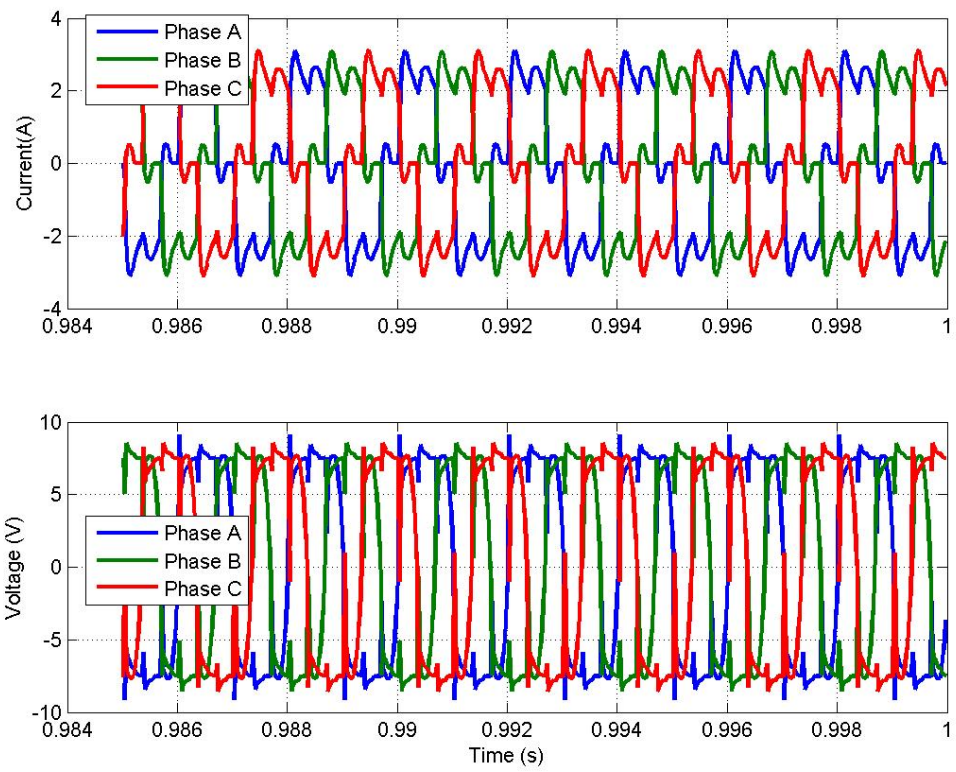


Figure 6.17: Winding Current and Induced Voltage Obtained From MAXWELL for Squarewave 6-pole Topology

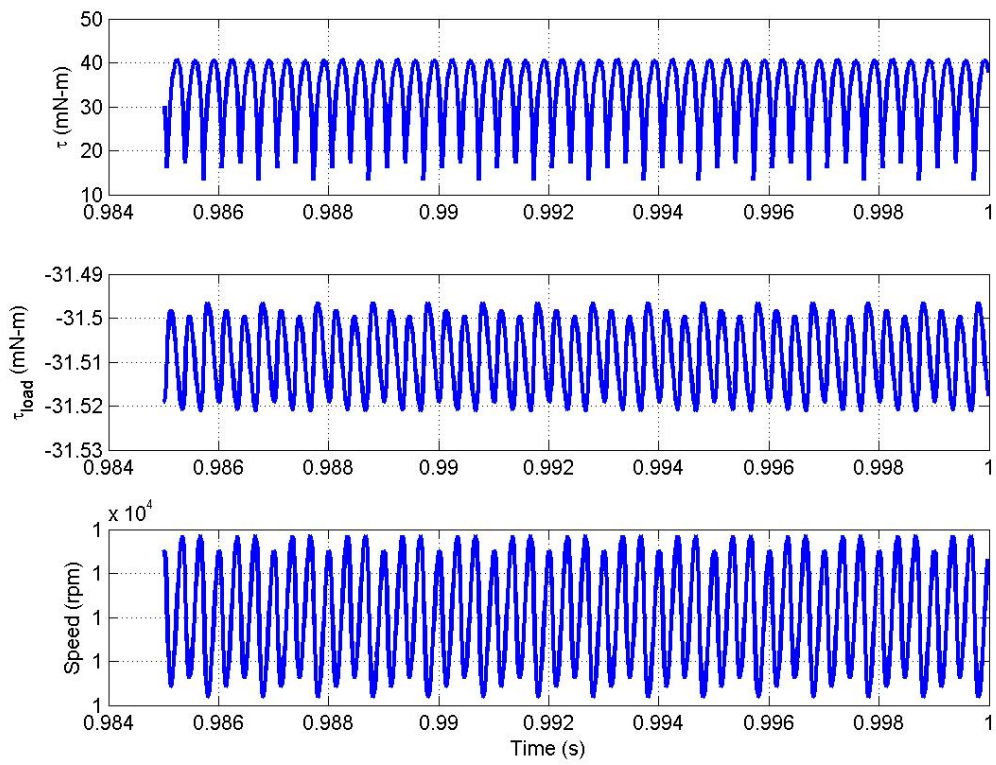


Figure 6.18: Torque and Speed Obtained From MAXWELL for Squarewave 6-pole Topology

Table 6.4: Comparison of Analytical and Simulation Results of Squarewave 6-Pole at Steady-State

	Squarewave 6-pole	
	Analytical	Simulation
I_{rms} (A)	1,68	2,00
e_{back} (V)	8,00	8,00
R_{ph} (mΩ)	80,30	80,30
L_{leak} (μH)	193,52	193,52
L_{ph} (μH)	386,79	294,50
B_{gav} (T)	0,43	0,46
q (A.t/m)	3847,00	4577,00
$B_{stator-peak}$ (T)	1,44	1,50
$B_{rotor-peak}$ (T)	1,44	1,50
P_{loss} (W)	2,37	2,28
P_{out} (W)	33,00	34,28
τ_{motor} (mN.m)	32,00	32,7
η (%)	93,30	93,76

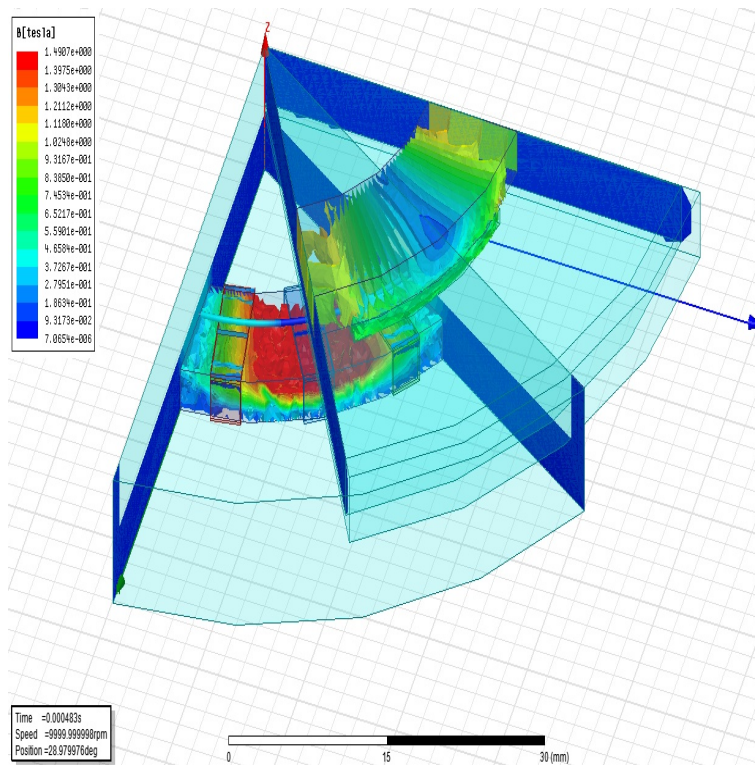


Figure 6.19: Magnetic Fields Obtained in MAXWELL for AF Squarewave 6-pole Topology

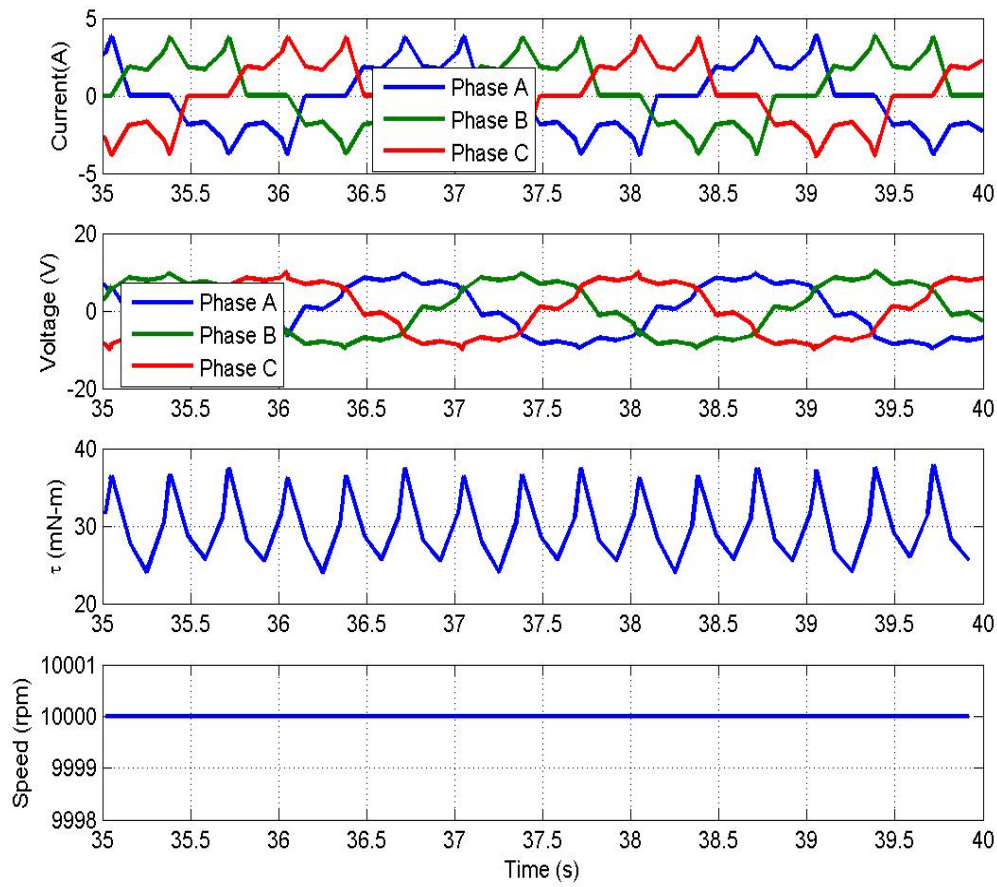


Figure 6.20: Parameters Obtained From MAXWELL for AF Squarewave 6-pole Topology

Table 6.5: Overall MAXWELL Results

	Sine 2-pole	Sine 6-pole	Square 2-pole	Square 6-pole	AF 6-pole
Tooth Flux Density	1.55 T	1.54 T	1.56 T	1.50 T	1.4 T
Torque	32,7 mN-m	32,9 mN-m	32,90 mN-m	32,7 mN-m	32 mN-m
Torque Ripple	20 mN-m	20 mN-m	5 mN-m	25 mN-m	13 mN-m
Winding Current	1.76 A	1.7 A	2.00 A	2.00 A	2.00 A
Back emf	9.2 V	9 V	7 V	8 V	7.5 V

CHAPTER 7

CONCLUSION

This chapter briefly wraps up all the results obtained and stated in Chapter 5 and Chapter 6, and makes deductions about the future work that can be derived afterwards.

7.1 Overall Results

In this thesis study, an alternative motor topology is proposed for Control Moment Gyroscope applications, which is a crucial inertial system in a satellite. For this purpose, first operation principle of CMGs is stated and typical electrical motors used in an aerospace application are defined. Then, brushless DC motors are classified depending on the permanent magnet location, flux direction and excitation. Problems in the current CMG prototypes are defined and motor selection criteria is stated in Chapter 3. In Chapter 4, outer-rotor brushless DC motor design procedure is explained and the first results are illustrated. In Chapter 5, a design is chosen for each topology, namely for excitation and pole number and results obtained analytically are investigated. In Chapter 6, the design set is prepared for validation under Finite-Element Analysis and simulation results are illustrated, as well as the design conducted by [7]. Overall results are summarized below.

Overall volume comparison is shown Figure 7.1.

As shown in Figure 7.1, volume comparison is made both with volume and torque per unit volume. If volume is investigated, it is concluded that 6-pole designs are smaller in volume when compared to the 2-pole designs. This fact leads to the explanation of

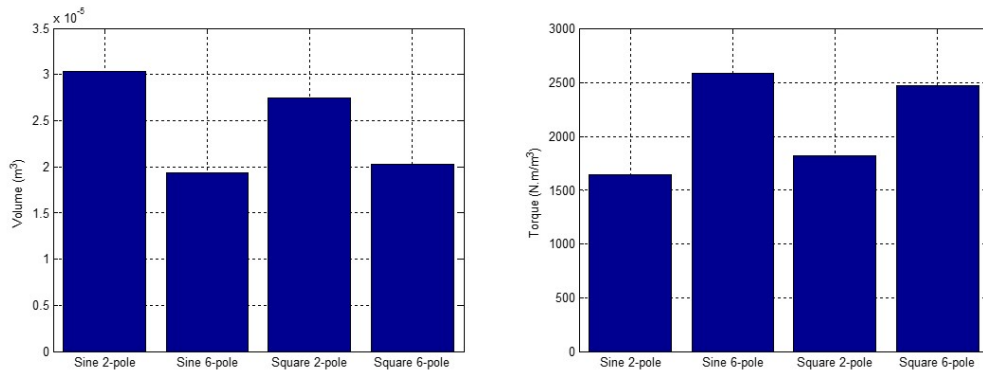


Figure 7.1: Overall Volume Comparison of Chosen Designs

the second volume comparison criteria, which is the torque per unit volume criteria; because torque per unit volume implies the reciprocal of the volume of the design, so if the volume is less, then the torque per unit volume value becomes higher. Therefore, it can be said that the torque production per unit volume is higher in 6-pole designs compared to the 2-pole designs. One point that must be noted is that the axial-flux BLDC motor designed in [7] has a volume of $1.89 \times 10^{-5} m^3$, which is between the two 6-pole designs.

Mass comparison is made in Figure 7.2, again both with mass and torque per unit mass.

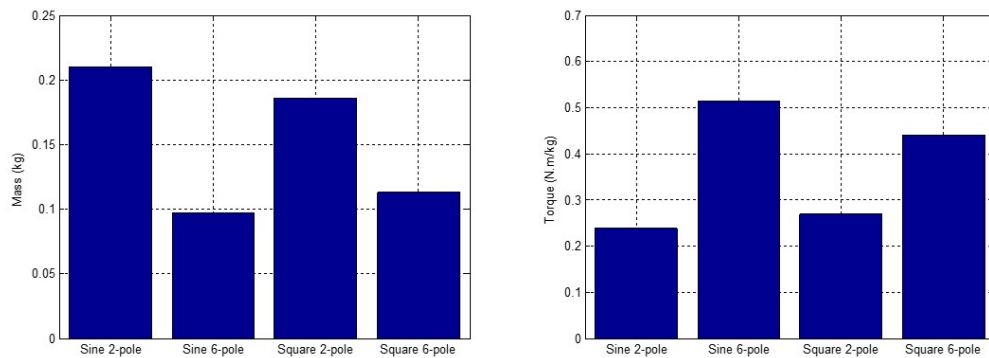


Figure 7.2: Overall Mass Comparison of Chosen Designs

According to Figure 7.2, 6-pole motors are smaller in mass than the 2-pole counterparts. Therefore, torque per unit mass values of these designs are larger than that of 2-pole designs. The axial-flux design is calculated to be about 0.1 kg, which lies, again, between the 6-pole motors.

Inertia and inertia contributions of the proposed motors are compared in Figure 7.3.

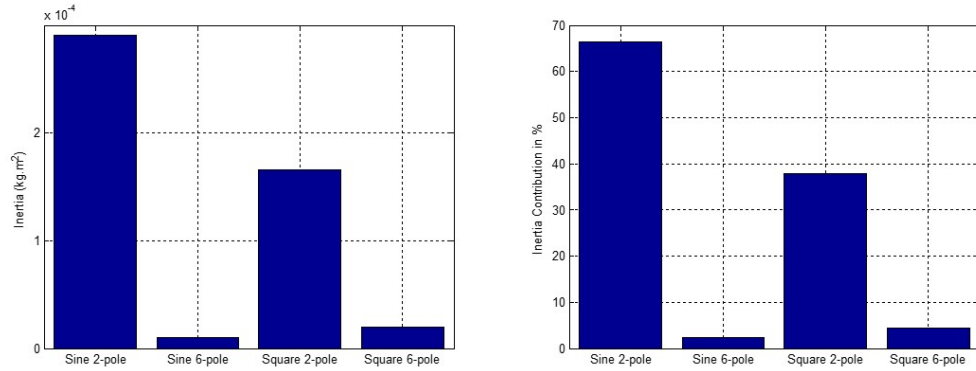


Figure 7.3: Overall Inertia Comparison of Chosen Designs

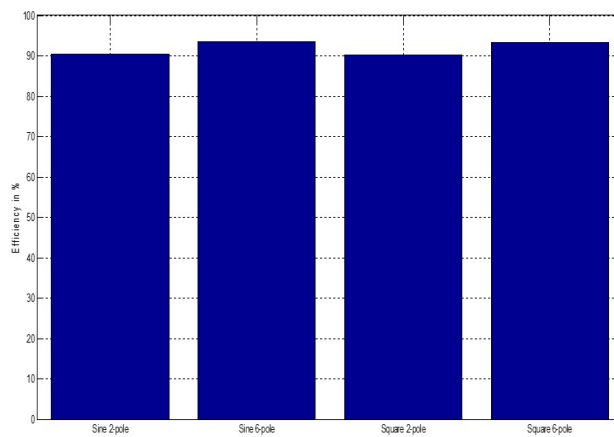


Figure 7.4: Overall Efficiency Comparison of Chosen Design

When inertia values are investigated, it is found that 2-pole designs have larger inertia compared to the 6-pole counterparts. This is an acceptable result due to the fact that the geometry of these designs are more flat and pancake-like, so inertia of the 2-pole designs are concluded to be higher. Additionally, inertia contribution is directly proportional to the inertia of each design. Thus, inertia contributions of these designs are higher than the 6-pole counterparts. Inertia of the axial-flux equivalent is calculated to be $0.3 \times 10^{-4} \text{ kg.m}^2$, which is again between the 6-pole outer-rotor counterparts.

The final comparison is made for efficiency. Efficiency values are shown in Figure 7.4.

Efficiency of the 6-pole designs reach to about 93% while the efficiency value of the 2-pole designs are around 90%. Therefore, 6-pole designs seem to be more efficient than the 2-pole counterparts. The efficiency of the axial-flux design is calculated to be approximately 92%.

As final remarks with the axial-flux design, it can be said that the mass of the 6-pole squarewave RF outer-rotor motor solution is slightly heavier than the AF solution and its volume is less than AF solution. Mass and volume calculation is made, considering only the active material mass and volume of the motors. This however is of secondary importance. What matters is the mass and volume of the system when it is configured to have the required inertia. One must note here that the RF motor solution has a large diameter and is thin. The contribution of the motor inertia to the required inertia is about 2% of the total, while for the AF solution this ratio is 6%.

To conclude the results, 6-pole designs can be preferred if higher torque per unit mass or volume with higher efficiency is desired. On the other hand, if larger inertia contributions are desired in the system design, 2-pole designs can be preferred.

7.2 Future Work

Possible future work areas that can be derived from this work are summarized as follows:

- It must be noted that, although the temperature model is presented in Chapter 3, the temperature characteristics are not deeply studied. The main point of consideration is that since these motors are intended to be used in a satellite application, cooling techniques must be well handled regarding heat transfer by conduction or by radiation. Here, materials are selected depending on the radiation sensitivity. Yet, cooling issue must not be ignored during an integration of such motors to the system.
- Although inertia contributions are mentioned in this study, proper integration of the motors of interest are not included in the thesis. A detailed investigation on this issue must be carried out in order to fully understand the volumetric cost of the electrical motors to the whole CMG system.
- Since the motors are designed in surface-mounted magnet topology, the mechanical considerations can be further investigated. In order to protect magnets from detachment, a non-magnetic ring can be put inside the magnet surface, which

may be counted as a solution for the mentioned issue.

- Further designs can be studied by considering torque minimization techniques such as skewing and pole arcing. Improving the torque ripple ratings of the designs may lead to a better wheel motor design for a typical CMG application.
- The design can be handled using multi-objective optimization techniques in order to further minimize the mass and volume by defining certain constraints such as electrical loading, air gap magnetic flux density and current density.

REFERENCES

- [1] Public lessons learned entry 0893. <http://www.nasa.gov/offices/oce/llis/0893.html>. Accessed: 19/09/2014.
- [2] Vacomax 225 hr properties. http://www.vacuumschmelze.com/en/products/permanent_magnets_assemblies/permanent_magnets/sm_co/vacomax/vacomax_225_hr.html. Accessed: 10/08/2014.
- [3] Douglas D. Havenhill. Direct torque control moment gyroscope, February 1995.
- [4] V.J. Lappas, W.H. Steyn, and C.I. Underwood. Attitude control for small satellites using control moment gyros. *Acta Astronautica*, 51(1-9):101–111, July 2002.
- [5] X Roser and M Sghedoni. Control moment gyroscopes (cmg's) and their application in future scientific missions. In *Spacecraft Guidance, Navigation and Control Systems*, volume 381, page 523, 1997.
- [6] D.C. Hanselman. *Brushless Permanent Magnet Motor Design*. Magna Physics Publishing, 2006.
- [7] Kurtuluş Yılmaz. Comparison of axial flux and radial flux brushless dc motor topologies for control moment gyroscope wheel applications. Master's thesis, Middle East Technical University, April 2009.
- [8] N. Mohan. *Electric Machines and Drives*. CourseSmart Series. Wiley, 2012.
- [9] Vaios J. Lappas. *A Control Moment Gyro (CMG) Based Attitude Control System (ACS) for Agile Small Satellites*. PhD thesis, University of Surrey, October 2002.
- [10] W Jaffe and TJ Sokira. Brushless dc motors: Electronics commutation and control, 1990.
- [11] Padmaraja Yedamale. Brushless dc (bldc) motor fundamentals. *Microchip Technology Inc*, page 20, 2003.
- [12] David G Dorrell, M Hsieh, Mircea Popescu, Lyndon Evans, David A Staton, and Vic Grout. A review of the design issues and techniques for radial-flux brushless surface and internal rare-earth permanent-magnet motors. *Industrial Electronics, IEEE Transactions on*, 58(9):3741–3757, 2011.

- [13] F Sahin, AM Tuckey, and AJA Vandenput. Design, development and testing of a high-speed axial-flux permanent-magnet machine. In *Industry Applications Conference, 2001. Thirty-Sixth IAS Annual Meeting. Conference Record of the 2001 IEEE*, volume 3, pages 1640–1647. IEEE, 2001.
- [14] T.J.E. Miller. *Brushless permanent-magnet and reluctance motor drives*. Monographs in electrical and electronic engineering. Clarendon Press, 1989.
- [15] A. Cavagnino, M. Lazzari, F. Profumo, and A. Tenconi. A comparison between the axial flux and the radial flux structures for pm synchronous motors. In *Industry Applications Conference, 2001. Thirty-Sixth IAS Annual Meeting. Conference Record of the 2001 IEEE*, volume 3, pages 1611–1618 vol.3, Sept 2001.
- [16] H.B. Ertan and K. Yilmaz. Choice of pole number of two-rotor axial-flux pm motor for control moment gyroscope. In *Electrical Machines and Power Electronics and 2011 Electromotion Joint Conference (ACEMP), 2011 International Aegean Conference on*, pages 620–625, Sept 2011.
- [17] Dean J. Patterson, Jessica L. Colton, Brad Mularcik, Byron J. Kennedy, Steven Camilleri, and Rafal Rohoza. A comparison of radial and axial flux structures in electrical machines. *2009 IEEE International Electric Machines and Drives Conference*, pages 1029–1035, May 2009.
- [18] Z Rahman. Evaluating radial, axial and transverse flux topologies for 'in-wheel' motor. In *Power Electronics in Transportation, 2004*, pages 75–81. IEEE, 2004.
- [19] Gordon R Slemon. On the design of high-performance surface-mounted pm motors. *Industry Applications, IEEE Transactions on*, 30(1):134–140, 1994.
- [20] Nicola Bianchi and Silverio Bolognani. Design techniques for reducing the cogging torque in surface-mounted pm motors. *Industry Applications, IEEE Transactions on*, 38(5):1259–1265, 2002.
- [21] Emre Yavuzoğlu. Steering laws for control moment gyroscope systems used in spacecraft attitude control. Master's thesis, Middle East Technical University, November 2003.
- [22] H.B. Ertan and N. Cagan. Comparison of outer rotor radial flux and axial flux pm motors for cmg application. In *Electrical Machines (ICEM), 2014 International Conference on*, pages 1031–1036, Sept 2014.
- [23] C.A. Gross. *Electric Machines*. Electric Power Engineering Series. Taylor & Francis, 2006.

APPENDIX A

PARAMETERS AND DESCRIPTIONS

Table A.1 shows the parameters and descriptions used throughout the thesis study. Other tables regarding the dimensions are prepared by considering this table.

Table A.1: Parameters and Descriptions

R_{DL}	Ratio
D_i (mm)	Inner diameter
L (mm)	Axial length
D_o (mm)	Outer diameter
g (mm)	Air gap
h_s (mm)	Slot depth
l_m (mm)	Magnet thickness
h_1 (mm)	Tooth lip-1
h_2 (mm)	Tooth lip-2
w_1 (mm)	Lip opening
w_2 (mm)	Slot thickness
h_{sbc} (mm)	Stator back core thickness
t_1 (mm)	Tooth width at air gap
t_2 (mm)	Tooth width
J (g.m ²)	Inertia of the motor
V (cm ³)	Volume of the motor
M_{total} (g)	Mass of the motor
R_{ph} (mΩ)	Phase resistance
L_g (μH)	Air gap inductance
L_{end} (μH)	End turn inductance
L_{leak} (μH)	Leakage inductance
L_{ph} (μH)	Phase inductance
I_{rms} (A)	rms Current
q (A.t/m)	Electrical loading

APPENDIX B

DESIGN OUTPUTS WITH VARYING RATIO VALUES

This part shows the tabulated results upon applying the analytical solution with varying ratio, in MATLAB. Sinusoidal 2-pole results are shown in Table B.1.

Sinusoidal 6-pole results are shown in Table B.2.

Squarewave 2-pole results are shown in Table B.3.

Squarewave 6-pole results are shown in Table B.4.

Table B.1: Design Outputs Calculated Analytically for Sinusoidal 2-pole Topology

Parameter	Value					
R_{DL}	0,7	1	1,3	3	10	20
D_i (mm)	30,2	32,1	33,7	39,6	51,1	59,5
L (mm)	43,1	32,1	25,9	13,2	5,1	3,0
D_o (mm)	57,1	60,5	63,3	73,9	94,9	112,1
g (mm)	0,75	0,75	0,75	0,75	0,75	0,75
h_s (mm)	1,27	1,51	1,70	2,44	3,87	4,92
l_m (mm)	1,36	1,38	1,40	1,51	2,01	3,19
h_1 (mm)	1	1	1	1	1	1
h_2 (mm)	1	1	1	1	1	1
w_1 (mm)	0,75	0,75	0,75	0,75	0,75	0,75
w_2 (mm)	2,41	2,54	2,64	3,03	3,78	4,33
h_{sbc} (mm)	11,3	12,1	12,6	14,9	19,2	22,3
t_1 (mm)	4,52	4,86	5,13	6,17	8,16	9,64
t_2 (mm)	2,41	2,54	2,64	3,03	3,78	4,33
J (g.m ²)	0,30	0,28	0,27	0,26	0,27	0,31
V (cm ³)	110,2	92,3	81,5	56,7	36,1	29,3
M_{total} (g)	1291,8	940,5	763,3	441,1	248,5	192,7
R_{ph} (mΩ)	80,4	77,4	80,3	114,3	235,6	361,5
L_g (μH)	31,9	35,0	39,1	62,7	111,2	117,2
L_{end} (μH)	1,17	1,70	2,35	7,44	38,58	93,32
L_{leak} (μH)	37,4	38,9	41,8	59,0	94,2	115,0
L_{ph} (μH)	70,5	75,6	83,2	129,1	244,0	325,4
I_{rms} (A)	2,44	2,60	2,66	2,67	2,62	2,66
q (A.t/m)	1697	2011	2265	3211	5007	6324

Table B.2: Design Outputs Calculated Analytically for Sinusoidal 6-pole Topology

Parameter	Value					
R_{DL}	0,7	1	1,3	3	10	20
D_i (mm)	20,5	22,3	23,7	28,9	38,6	45,7
D_o (mm)	33,1	35,9	38,1	45,4	55,9	62,4
L (mm)	29,3	22,3	18,2	9,6	3,9	2,3
g (mm)	0,75	0,75	0,75	0,75	0,75	0,75
h_s (mm)	5,18	5,85	6,38	8,33	11,98	14,65
l_m (mm)	2,98	3,28	3,49	3,92	3,04	1,87
h_1 (mm)	1	1	1	1	1	1
h_2 (mm)	1	1	1	1	1	1
w_2 (mm)	1,34	1,43	1,51	1,79	2,32	2,71
h_{sbc} (mm)	2,56	2,79	2,96	3,61	4,83	5,72
t_2 (mm)	1,34	1,43	1,51	1,79	2,32	2,71
J (g.m ²)	0,013	0,014	0,014	0,015	0,015	0,014
V (cm ³)	25,2	22,5	20,7	15,6	9,5	7,0
M_{total} (g)	175,6	128,5	104,1	58,9	31,1	23,1
R_{ph} (mΩ)	81,5	84,7	86,2	95,0	145,3	200,9
L_g (μH)	18,4	22,5	25,5	34,3	42,5	181,0
L_{end} (μH)	2,37	3,85	5,38	14,95	69,41	165,18
L_{leak} (μH)	214,3	252,5	277,9	358,9	545,2	676,6
L_{ph} (μH)	235,0	278,9	308,8	408,2	657,1	1022,8
I_{rms} (A)	2,64	2,61	2,61	2,67	2,66	2,67
q (A.t/m)	5421	6037	6524	8298	11569	13937

Table B.3: Design Outputs Calculated Analytically for Squarewave 2-pole Topology

Parameter	Value					
R_{DL}	0,7	1	1,3	3	10	20
D_i (mm)	32,3	34,2	35,7	41,6	53,1	61,6
L (mm)	46,1	34,2	27,5	13,9	5,3	3,1
D_o (mm)	61,8	65,2	68,0	78,8	100,2	117,7
g (mm)	0,75	0,75	0,75	0,75	0,75	0,75
h_s (mm)	0,96	1,17	1,33	1,96	3,20	4,11
l_m (mm)	1,35	1,37	1,39	1,49	1,97	3,06
h_1 (mm)	1,00	1,00	1,00	1,00	1,00	1,00
h_2 (mm)	1,00	1,00	1,00	1,00	1,00	1,00
w_1 (mm)	0,75	0,75	0,75	0,75	0,75	0,75
w_2 (mm)	2,65	2,78	2,88	3,29	4,07	4,66
h_{sbc} (mm)	12,7	13,4	14,0	16,3	20,8	24,2
t_1 (mm)	4,88	5,21	5,48	6,51	8,51	10,01
t_2 (mm)	2,65	2,78	2,88	3,29	4,07	4,66
J (g.m ²)	0,45	0,41	0,39	0,35	0,36	0,39
V (cm ³)	138,5	114,2	99,9	67,6	41,9	33,5
M_{total} (g)	1622,3	1169,1	942,5	534,8	294,8	226,1
R_{ph} (mOhm)	55,0	58,3	64,7	89,8	173,6	272,8
L_g (uH)	19,2	23,3	28,0	44,2	74,5	81,9
L_{end} (uH)	0,70	1,13	1,67	5,22	25,62	63,65
L_{leak} (uH)	20,2	23,4	27,0	37,7	57,2	71,8
L_{ph} (uH)	40,1	47,8	56,7	87,1	157,4	217,3
I_{rms} (A)	2,76	2,82	2,80	2,85	2,92	2,94
q (A.t/m)	1309	1577	1795	2620	4204	5373

Table B.4: Design Outputs Calculated Analytically for Squarewave 6-pole Topology

Parameter	Value					
R_{DL}	0,7	1	1,3	3	10	20
D_i (mm)	21,04	22,81	24,22	29,43	39,19	46,32
L (mm)	30,05	22,81	18,63	9,81	3,92	2,32
D_o (mm)	38,13	40,41	42,30	49,97	69,12	92,11
g (mm)	0,75	0,75	0,75	0,75	0,75	0,75
h_s (mm)	4,22	4,79	5,24	6,91	10,03	12,31
l_m (mm)	4,00	3,94	3,92	4,21	7,15	13,79
h_1 (mm)	1	1	1	1	1	1
h_2 (mm)	1	1	1	1	1	1
w_1 (mm)	0,75	0,75	0,75	0,75	0,75	0,75
w_2 (mm)	1,10	1,15	1,20	1,36	1,67	1,89
h_{sbc} (mm)	3,79	4,11	4,37	5,31	7,07	8,35
t_1 (mm)	2,92	3,23	3,48	4,39	6,09	7,33
t_2 (mm)	1,10	1,15	1,20	1,36	1,67	1,89
J (g.m ²)	0,028	0,027	0,027	0,028	0,040	0,069
V (cm ³)	34,3	29,3	26,2	19,2	14,7	15,4
M_{total} (g)	241,0	177,3	145,0	86,5	53,8	47,6
R_{ph} (mΩ)	62,7	64,3	63,9	74,2	113,4	158,0
L_g (μH)	13,04	15,82	17,47	24,79	30,48	27,11
L_{end} (μH)	1,68	2,71	3,70	10,80	49,74	118,70
L_{leak} (μH)	120,6	139,4	149,0	198,5	291,2	357,2
L_{ph} (μH)	135,4	157,9	170,1	234,1	371,4	503,0
I_{rms} (A)	2,89	2,88	2,92	2,92	2,94	2,95
q (A.t/m)	4727	5299	5751	7401	10446	12652

APPENDIX C

CHOSEN DESIGNS FOR EACH TOPOLOGY

Table C.1 shows the chosen designs after equating the electrical loading value to the design constraint, which is 6000 A-t/m.

Table C.1: Chosen Designs

Parameter	Sinusoidal 2-pole	Sinusoidal 6-pole	Squarewave 2-pole	Squarewave 6-pole
R_{DL}	17	0,95	10	1,5
D_i (mm)	57,39	22	47,33	25,03
L (mm)	3,38	23,16	4,73	16,69
D_o (mm)	107,07	32,62	85,97	39,33
g (mm)	0,75	0,75	0,75	0,75
h_s (mm)	4,66	5,75	4,7	5,5
l_m (mm)	2,55	1,81	2,1	1,88
h_1 (mm)	1	1	1	1
h_2 (mm)	1	1	1	1
w_1 (mm)	0,75	0,75	0,75	0,75
w_2 (mm)	4,2	0,92	3,31	1,22
h_{sbc} (mm)	21,54	2,75	16,46	4,52
t_1 (mm)	9,27	3,09	7,51	3,62
t_2 (mm)	4,19	0,92	3,31	1,22
N_{ph}	68	26	56	30
J (g.m ²)	0,29	0,01	0,17	0,02
V (cm ³)	30,39	19,36	27,47	20,27
M_{total} (g)	210,33	97,11	186,12	113,22

APPENDIX D

6-POLE SQUAREWAVE AXIAL-FLUX DESIGN PARAMETERS

Table D.1 shows the design results of the axial-flux squarewave 6-pole brushless DC motor conducted by [7].

Table D.1: AF 6-pole Design

Parameter	Description	Value
D_i (mm)	Inner Diameter	33,40
L (mm)	Axial Length	15,80
D_o (mm)	Outer Diameter	51,40
g (mm)	Airgap	1,65
l_m (mm)	Magnet Thickness	1,00
l_r (mm)	Rotor Thickness	2,60
l_{cr} (mm)	Stator Thickness	5,20
J ($g.m^2$)	Inertia	0,03
V (cm^3)	Volume	18,90
M_{total} (g)	Mass	109,60
R_{ph} ($m\Omega$)	Phase Resistance	87,00
L_{ph} (μH)	Phase Inductance	14,60
P_{core} (W)	Core Loss	2,00
P_{cu} (W)	Copper Loss	0,76
P_{total} (W)	Total Loss	2,75
η	Efficiency	0,92
I_{rms} (A)	rms Current	2,65
q (A.t/m)	Electrical Loading	5400